Investigation of granular behavior in bedload transport using an Eulerian-Lagrangian model

Raphaël Maurin

UNIVERSITÉ GRENOBLE ALPES

THÈSE

Pour obtenir le grade de

DOCTEUR DE L'UNIVERSITÉ DE GRENOBLE ALPES

Spécialité : **Sciences de la Terre et Univers, Environnement**

Arrêté ministériel : 7 aout 2006

Présentée par

Raphaël MAURIN

Thèse dirigée par **Philippe FREY**
et co-encadrée par **Julien CHAUCHAT et Bruno CHAREYRE**

préparée à **Irstea Grenoble**
dans l'Ecole Doctorale **Terre, Univers, Environnement**

Étude du comportement granulaire en transport par charriage basée sur un modèle Eulérien-Lagrangien

Thèse soutenue publiquement le **11/12/2015**,
devant le jury composé de :

M. Alexandre VALANCE
Directeur de recherche, CNRS, Institut de Physique de Rennes, Président
Mme. Kimberly HILL
Associate Professor, University of Minnesota, Rapporteur
M. Hervé CAPART
Professor, National Taiwan University, Rapporteur
M. Philippe CLAUDIN
Directeur de recherche, CNRS, ESPCI, Examinateur
M. Éric BARTHÉLÉMY
Professeur des Universités, LEGI, Grenoble INP, Examinateur
M. Philippe FREY
Chercheur HDR, IRSTEA Grenoble, Directeur de thèse
M. Julien CHAUCHAT
Maître de Conférence, LEGI, Grenoble INP, Co-encadrant de thèse
M. Bruno CHAREYRE
Maître de Conférence, 3SR, Grenoble INP, Co-encadrant de thèse

UNIVERSITÉ GRENOBLE ALPES

THÈSE

Pour obtenir le grade de

DOCTEUR DE L'UNIVERSITÉ DE GRENOBLE ALPES

Spécialité : **Sciences de la Terre et Univers, Environnement**

Arrêté ministériel : 7 aout 2006

Présentée par

Raphaël MAURIN

Thèse dirigée par **Philippe FREY**
et co-encadrée par **Julien CHAUCHAT et Bruno CHAREYRE**

préparée à **Irstea Grenoble**
dans l'Ecole Doctorale **Terre, Univers, Environnement**

Investigation of granular behavior in bedload transport using an Eulerian-Lagrangian model

Thèse soutenue publiquement le **11/12/2015**,
devant le jury composé de :

M. Alexandre VALANCE
Directeur de recherche, CNRS, Institut de Physique de Rennes, Président
Mme. Kimberly HILL
Associate Professor, University of Minnesota, Rapporteur
M. Hervé CAPART
Professor, National Taiwan University, Rapporteur
M. Philippe CLAUDIN
Directeur de recherche, CNRS, ESPCI, Examinateur
M. Éric BARTHÉLÉMY
Professeur des Universités, LEGI, Grenoble INP, Examinateur
M. Philippe FREY
Chercheur HDR, IRSTEA Grenoble, Directeur de thèse
M. Julien CHAUCHAT
Maître de Conférence, LEGI, Grenoble INP, Co-encadrant de thèse
M. Bruno CHAREYRE
Maître de Conférence, 3SR, Grenoble INP, Co-encadrant de thèse

Résumé : Le transport solide par charriage représente la contribution principale dans l'évolution morphologique du lit des cours d'eau, et se situe donc au coeur d'enjeux majeurs liés aux risques d'inondations. Il est caractérisé par l'interaction entre des comportements collectifs granulaires non-triviaux et un écoulement fluide turbulent. À ce titre, sa compréhension représente à la fois un défi scientifique et une problématique sociétale. L'approche numérique présentée met l'accent sur la description de la phase granulaire et se concentre sur des configurations idéalisées de transport solide par charriage en conditions stationnaires et uniformes, considérant des échantillons de particules sphériques monodisperses dans un écoulement fluide unidirectionnel. Cette configuration simplifiée permet d'étudier en détail les mécanismes granulaires sous-jacents au phénomène. Un modèle numérique couplé minimal pour la description du transport par charriage est présenté, associant une modélisation par éléments discrets tri-dimensionnelle à une résolution fluide unidirectionnelle moyennée en volume. Le modèle est comparé à l'expérience en considérant à la fois la courbe du débit solide adimensionné en fonction du nombre de Shields en trois dimensions, et des profils moyens verticaux de vitesse particulaire, fraction volumique et densité de débit solide dans une configuration quasi-bidimensionnelle. L'étude de la sensibilité aux paramètres a mis en évidence l'importance du couplage entre phases granulaire et fluide, et la robustesse de l'accord entre simulations et expériences. Fort de cette validation expérimentale, le modèle est utilisé pour analyser la structure verticale granulaire en transport par charriage. En étudiant l'effet de la pente et de la densité spécifique, il est montré que les formulations classiques du nombre de Shields et du débit solide adimensionné ne prennent pas en compte de manière appropriée les effets de ces deux paramètres. À partir d'une analyse des équations continues moyennées diphasiques, la contribution manquante est identifiée comme résidant dans l'effet de l'écoulement fluide à l'interieur du lit granulaire. Cette contribution prend une importance fondamentale proche de la transition vers un régime de type lave torrentielle granulaire. Une modification du nombre de Shields est proposée et apparaît réunir les données sur une courbe maîtresse en considérant le débit solide adimensionné en fonction du nombre de Shields modifié. Dans un deuxième temps, la rhéologie de la phase granulaire en transport par charriage est caractérisée en évaluant localement le tenseur des contraintes particulaires en fonction de la profondeur. Ceci est réalisé pour une série de simulations en faisant varier le nombre de Shields, le diamètre des grains et la densité spécifique. Sur l'ensemble des résultats, la partie quasi-statique de l'écoulement met en évidence un régime de creeping avec la présence de signatures caractéristiques d'effets non-locaux. Au-dessus de cette zone, la partie d'écoulement granulaire dense est bien décrite par la rhéologie $\mu(I)$ et persiste jusqu'à des nombres inertiels inhabituellement élevés. Ce régime est caractérisé par la co-existence des contributions collisionelle et frictionelle. La transition entre le régime granulaire dense et gazeux dépend du nombre de Shields, de la pente et de la densité spécifique. La partie granulaire supérieure suit un comportement de type balistique. Ces résultats améliorent la compréhension des mécanismes granulaires en transport solide par charriage et représentent également un défi pour les théories granulaires existantes.

Mots clés : Transport de sédiments, charriage, milieux granulaires, méthode par éléments discrets, écoulement diphasique, couplage fluide-grain, structure granulaire verticale, rhéologie granulaire

Abstract: Turbulent bedload transport represents the main contribution to the riverbed morphological evolution, and associates the non-trivial collective granular behavior with a turbulent fluid flow. Therefore, its description is both a scientific challenge and a societal issue. The present numerical approach focuses on the granular phase characterization, and considers idealized steady uniform bedload transport, with monodisperse spherical beads and a unidirectional fluid flow. This simplified configuration allows to study the underlying physical mechanisms.
A minimal coupled numerical model is proposed, associating a three dimensional discrete element method with a one-dimensional volume-averaged fluid momentum balance. The model is compared with classical experimental results of dimensionless sediment transport rate as a function of the Shields number. The comparison is extended to granular depth profiles of solid volume fraction, solid velocity and sediment transport rate density in quasi-2D bedload transport configurations. Parameter sensitivity analysis evidenced the importance of the fluid-particle phase coupling, and showed a robust agreement of the model with the experiments. The validated model is further used to analyze the granular depth structure in bedload transport. Varying the channel inclination angle and the specific density, it is shown that the classical Shields number and dimensionless sediment transport rate formulations do not take appropriately into account the effects of these two parameters. Analyzing the solid depth profiles and the continuous two-phase flow equations, the neglected fluid flow inside the granular bed is identified as the missing contribution. Its importance is enhanced near the transition to debris flow. A rescaling of the Shields number is proposed and is shown to make all the data collapse onto a master curve when considering the dimensionless sediment transport rate as a function of the modified Shields number. In addition, the bedload transport granular rheology is characterized by computing locally the stress tensor as a function of the depth, for a serie of simulation varying the Shields number, particle diameter and specific density. Overall, the lowermost part is shown to follow a creeping regime and exhibits signature of non-local effects. The dense granular flow on the top of it, is well described by the $\mu(I)$ rheology and is observed to persist up to unexpectedly high inertial numbers. It is characterized by the co-existence of frictional and collisional contributions. The transition from dense to dilute granular flow is controlled by the Shields number, the slope and the specific density. Saltation is observed in the uppermost granular layer. These findings improve the understanding of bedload transport granular mechanisms and challenge the existing granular rheologies.

Keywords: Sediment transport, bedload, granular media, Discrete Element Method, two-phase flow, fluid-grain coupling, granular depth structure, granular rheology

Remerciements

Ces trois années de thèse se terminent et j'aimerais remercier tous ceux qui ont contribué de près ou de loin à rendre cette expérience plaisante et très enrichissante.

Tout d'abord j'aimerais remercier IRSTEA pour le financement de la thèse. J'aimerais également remercier tous les membres du jury d'avoir accepté d'évaluer mon travail de thèse. En particulier merci aux deux rapporteurs Kimberly Hill et Hervé Capart pour leurs lectures attentives du manuscrit et leurs commentaires, à Philippe Claudin et Éric Barthélémy pour leur présence et leurs questions intéressantes lors de la soutenance. Je pense aussi aux membres de mon comité de thèse qui m'ont aidé à avancer tout aux long de la thèse de par leurs regards exterieurs avisés, leurs remarques pertinentes et les discussions qu'on a pues avoir. Notamment, je voudrais remercier Alexandre Valance qui a également accepté de présider mon jury, et Pascale Aussillous que j'ai le plaisir de voir régulièrement depuis mon stage de L3. J'espère qu'on aura l'occasion de continuer à interagir ensemble.

Evidemment, je voudrais remercier mes trois encadrants de thèse qui m'ont été d'une aide précieuse dans cette aventure. Tout d'abord merci à Bruno Chareyre pour le travail effectué en tant que leader du code open-source Yade que j'ai utilisé, mais également merci pour tes remarques toujours à la fois surprenantes et pertinentes, qui m'ont amené à réfléchir sur bien des points que j'aurais pu considérer comme acquis. Un grand merci à Philippe Frey pour avoir initié ce sujet de thèse, pour m'avoir fait confiance, et avoir accepté de me donner de l'autonomie tout en m'accompagnant. Je crois que c'est en grande partie grâce à toi que cette thèse garde en vue l'application tout en étant relativement fondamentale, et c'est quelque chose que j'apprécie particulièrement. Merci également pour ta patience et ta sympathie, j'ai apprécié travailler à tes côtés et j'espère qu'on aura l'occasion de continuer à travailler ensemble dans la suite. Je compte sur toi pour reprendre le flambeau de la simulation numérique ! Enfin, j'aimerais exprimer toute ma gratitude envers Julien Chauchat notamment pour son encadrement exceptionnel, sa gestion parfaite de ma motivation, et la vision à long terme qu'il a eue par rapport à mes projets. C'est toujours un plaisir de discuter avec toi et j'espère qu'on continuera à interagir et à travailler ensemble.

Une thèse se fait également au sein d'un laboratoire et je crois avoir trouvé une perle avec Irstea (Cemagref!) Grenoble. Merci à tous pour l'ambiance exceptionnelle qui règne au quotidien dans ces locaux et qui m'a amené à venir travailler avec plaisir tous les matins ! En particulier, merci à Fred Ousset pour ta bonne humeur, ton sens de l'humour et tes conseils avisés sur l'affutage ou le percage des skis ! Merci à Christian pour l'atelier vélo et pour apporter une touche au labo qui détend toujours l'atmosphère. Merci à Francois pour l'aide sur Yade et les discussions multiples et variées. Merci à Adel et Lingran pour ce bureau multilingue et multiculturel qui a

mis en évidence mes carences en francais, en culture générale et en connaissance de l'administration ! Merci surtout pour votre bonne humeur et les discussions qu'on a pues avoir. Merci aux groupe de "doctorants" du début comme de la fin (entre autre Pascal, Philo, Dom, Gaëtan, Coraline, Guillaume P, Guillaume D, Félix, Perrine, Hugo, Simon, Gilles, Firmin, Antoine, Coralie,...), pour ces repas de midi et ces pauses cafés toujours animées et très agréables. En particulier, merci à Gaëtan pour les discussions, les sorties ski, le derby de la Meije, et les soirées toujours dré dans le pentu ! Je t'attends pour aller skier alors traîne pas trop sur la fin de ta thèse ! Pour finir, j'aimerais remercier mes colocs Mellie, Chloé, Boby et Viviana, Eva évidemment, mes amis et ma famille (en particulier la soeurette, le frérot et les parents !) qui sont toujours là pour me soutenir et pour me rappeler qu'il n'y a pas que la recherche dans la vie !

Contents

List of Symbols

α	Channel inclination angle
α_0	Onset of debris flow channel inclination angle
$\bar{\phi}$	Averaged mobile layer solid volume fraction
δ	Typical bedload transport length scale
δ_s	Granular mobile layer thickness
$\dot{\gamma}$	Particle shear rate
$\dot{n}$	Sediment transport rate in terms of beads per second
ϵ	Fluid volume fraction
η^f	Fluid dynamic viscosity
$\frac{\Delta Q_{rms}{}^i}{\langle Q^{ref} \rangle}$	Normalized transport rate profile root mean square deviation
κ	Von Karman constant
$\langle \rangle^f$	Fluid phase averaging
$\langle \rangle^p$	Particle phase averaging
$\langle \rangle^s$	Solid phase averaging
$\langle u_x \rangle^f$	Average streamwise fluid velocity
$\langle v_x^p \rangle$	Average streamwise particle velocity
$\mathcal{G}$	Averaging weighting function
μ	Shear to normal granular stress ratio, granular effective friction
μ^p	Contact granular friction coefficient
μ_s	Granular material static effective friction coefficient
ν^f	Fluid kinematic viscosity
ν^t	Eddy viscosity
ϕ	Solid volume fraction
ρ^f	Fluid density
ρ^p	Particle density
σ_{ij}^f	Fluid viscous stress tensor

τ^p	Particle shear stress
τ_b	Turbulent fluid bed shear stress
τ_f	Fluid resolution period
τ_t	Turbulent velocity fluctuation model resolution period
τ_{dem}	Discrete Element Method resolution period
τ_{ij}^f	Fluid viscous shear stress tensor
τ_{ij}^p	Particle stress tensor
θ	Macroscopic Shields number
θ^*	Shields number
$\vec{g}$	Acceleration of gravity vector
$\vec{v^p}$	Particle velocity
$\vec{x^p}$	Particle position
ζ	Richardson-Zaki exponent
C_D	Drag coefficient
d	Particle diameter
e_n	Contact granular restitution coefficient
h	Water free-surface elevation
I_c	Critical inertial number at the transition from dense to dilute granular flow
I_{dry}	Dry inertial number
I_{turb}	Turbulent inertial number
I_{visc}	Viscous inertial number
k_n	Contact normal stiffness coefficient
k_t	Contact tangential stiffness coefficient
l_i	ith component of the weighting function length scale
l_m	Turbulent mixing length
N_l	Number of bead layer of the granular bed
P^f	Fluid pressure
P^p	Particulate pressure
Q_s	Sediment transport rate per unit width
q_s	Density of sediment transport rate per unit width
Q_s^*	Dimensionless sediment transport rate, or Einstein's parameters
R_{ij}^f	Fluid Reynolds stress tensor

Re	Reynolds number
Re_p	Particle reynolds number
S^*	Suspension number
S_0	Channel slope
S_{ij}^f	Fluid effective viscous stress tensor
T	Granular temperature
U^f	Average fluid velocity in the water depth
u_*	Turbulent friction velocity
V^p	Particle volume
w_d	Water depth
w_s	Particle settling velocity

List of Figures

List of Tables

Chapter 1

Introduction

Enumerating the complex mechanisms observed in turbulent bedload transport, *Gilbert* (1914) concluded in his time that «it is necessary to supplement [the] observations by experiments in which the conditions are definitely controlled». More than a century later, bedload transport measured in the field remains poorly predicted by the formulas established in laboratories (*Bathurst*, 2007). Considering a fluid flow over a granular bed, the bedload transport is characterized by the part of the load rolling, sliding, or saltating near the bed. It is the typical displacement mode of particles with diameters of the order of centimeters (see figure 1.1) in rivers and mountain streams. Contrary to suspension, the relative importance of the grain inertia with respect to the turbulence intensity, leads to a downward buoyant weight on average larger than the upward fluid force originating from turbulent velocity fluctuations.
Bedload represents the main contribution of sediment transport to the morphological evolution of riverbeds. As such, it has major implications for environmental flows, from both ecological and anthropological point of view. The riverbed represents a fragile source of development for fish and plants. For example, the bed grain-size distribution is important for salmonid reproduction and bed incision can affect riverine plant development. Regarding human activities, incision is the cause of bridge or road collaspes (see figure 1.1). In addition, aggradation can worsen flooding during extreme events with possible important material damages (see figure 1.1) and human threats. Therefore, the study of bedload transport is important to predict and prevent such phenomena.

1.1 Context

The bedload transport rate is related to both the strength of the fluid flow, and the resistance to motion of the granular bed. Classically, these dependences are expressed by the Shields number (*Shields*, 1936), defined as the ratio between the

Figure 1.1: Bedload transport: typical streams and related issues. Credits for the pictures: P. Frey, P. Frey, F. Liébault and M. Chiari.

fluid bed shear stress τ_b and the buoyant specific weight:

$$\theta^* = \frac{\tau_b}{(\rho^p - \rho^f)gd}, \tag{1.1}$$

where ρ^p and ρ^f are respectively the particle and fluid densities, g is the acceleration of gravity, and d is the typical particle diameter. The transport rate per unit width Q_s is considered for more generality. It is made dimensionless following the formulation of *Einstein* (1942):

$$Q_s^* = \frac{Q_s}{\sqrt{(\rho^p/\rho^f - 1)gd^3}}. \tag{1.2}$$

The well-known empirical formula of *Meyer-Peter and Müller* (1948), relates the dimensionless sediment transport rate to the Shields number, and takes the simplified form:

$$Q_s^* = 8\left(\theta^* - \theta_c^*\right)^{3/2}, \tag{1.3}$$

where θ_c^* is the critical Shields number, corresponding to the value of the dimensionless bed shear stress at incipient motion. This formula describes well the global trend of the transport rate. Bedload transport formulas are the basis for engineering

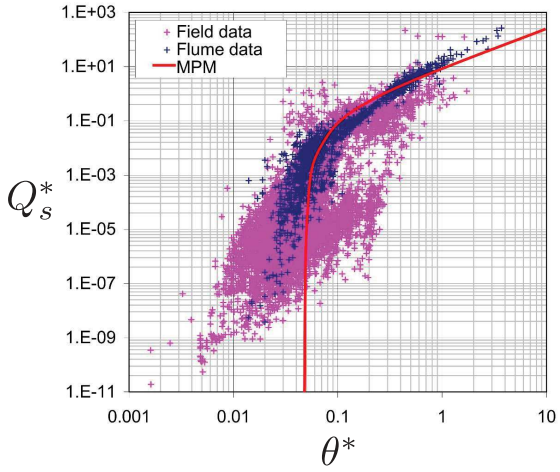

Figure 1.2: Dimensionless sediment transport rate as a function of the Shields number for data from the literature collected by *Recking* (2010). The red line shows the formula of *Meyer-Peter and Müller* (1948) (eq. 1.3). Figure after *Recking et al.* (2013).

applications using 1D or 2D shallow water formalism. It is used as a closure law to link the sediment transport rate and the fluid flow rate. However, the predictions using classical transport formulas can differ from what is observed in the field, by up to two order of magnitudes (*Bathurst*, 2007). In addition, the data from the literature present a very important scatter (*Recking*, 2010) (see figure 1.2). This is reflected by the multitude of existing bedload transport formulas, with variation of prefactors (*Rickenmann*, 1991; *Wong and Parker*, 2006; *Wilson*, 1987) or power-law (*Recking et al.*, 2008; *Recking*, 2010) with respect to the *Meyer-Peter and Müller* (1948) one. The prefactors as well as the critical Shields number, may depend on the slope (*Rickenmann*, 1991; *Lamb et al.*, 2008; *Recking*, 2009; *Rickenmann*, 2012), or the grain-size distribution (*Rickenmann*, 1991; *Recking*, 2010) for example. The origins of the poor predictions and the data dispersion, lie in the complexity of both the configurations encountered in the field and the phenomenon in itself. Therefore, it is worth simplifying the problem and adopting a different perspective to improve our understanding of bedload transport.

Focusing on the riverbed, bedload transport is also a granular phenomenon (*Frey and Church*, 2009, 2011). However, the granular interactions have been fewly studied, yet it could benefit from a wide literature in the physics of granular media (*Andreotti et al.*, 2013). The latter analyzes the behavior of an assembly of grains using the tools of mechanics, statistical physics and disordered media. More than in the tools, the difference stands in the approach adopted, which consists in simplifying the problem and complexifying it gradually in order to understand the underlying physical mechanisms. This is achieved by considering as a basis monodisperse beads sample in the rigid grain limit. As a consequence, the link with the field represents

a long-term view, and the scale of analysis is the one of the laboratory.

The goal of the present PhD is to develop a numerical model and study turbulent bedload transport in the framework of the physics of granular media. Therefore, it focuses on the challenges linked with bedload transport modelling, and analyzes the transport rate from simplified numerical experiments. This is realized in particular through the study of the granular rheology, which is central in the physics of granular media. Accordingly, the following sections present a synthetic literature review on bedload transport modelling, and granular rheology.

1.2 Numerical modelling in bedload transport

Different types of numerical models are used for bedload transport depending on the scale of description, which varies from few grains to the whole river. The differences between the models pertain to the description of the coupling between fluid and granular phases, and to the closures adopted. Indeed, to get rid of smaller scales description and improve the computational cost, it is made use of closures calibrated on semi-empirical or empirical basis. As an example, the shallow water models used for the description of large scale problems ($\sim 10\ km$, e.g. a part of a river) take advantage of the scale difference between the length of the river and the water depth. The simplified equations require modelling of the fluid dissipation at the base, as well as of the fluid effect on the granular phase. The latter is classically modelled with the bedload transport formulas, and might consequently lead to inaccurate descriptions. Therefore, the closures are relevant to model a problem without taking into account smaller scales, but are sources of errors.

Numerical models for bedload transport are mainly based on the description of the problem as a granular and a fluid phases in interaction. Following this two-phase decomposition, there are two major possibilities for numerical modelling: a continuous description for the two phases (Euler/Euler, e.g. *Jha and Bombardelli* (2010)) or a continuous description for the fluid phase and a discrete one for the granular phase (Euler/Lagrange, e.g. *Ji et al.* (2013)). Regarding the latter, all particles are described independently using the Discrete Element Method (DEM) (e.g. *Cundall and Strack* (1979)), solving explicitely the equation of motion for each individual particle. The effect of the fluid is taken into account through the hydrodynamic forces applied to each particle. The different scales of fluid description range from relatively large scale average description (e.g. *Revil-Baudard and Chauchat* (2013)), to Direct Numerical Simulation (DNS, e.g. *Wachs* (2011)) resolving the fluid locally around the particles down to the smallest turbulence length scale.

DNS or equivalently Fully Resolved Simulation (FRS), solve the Navier-Stokes equation with a very fine grid, considering the particles as moving boundaries. Con-

tact singularities due to lubrication are handled with a closure law, applied when the gap between two particles is lower than the fluid mesh. The particle hydrodynamic forces are evaluated from the integral of the fluid stress tensor on the particle surface. Accordingly, the fluid-particle coupling is directly related to the local scale, and the interactions between the turbulence and the particles are explicitely accounted for. While being today computationally very demanding, DNS-DEM couplings have already been applied to sediment transport (*Wachs*, 2011; *Simeonov and Calantoni*, 2012; *Ji et al.*, 2013; *Kidanemariam et al.*, 2013; *Kidanemariam and Uhlmann*, 2014; *Vowinckel et al.*, 2014; *Ji et al.*, 2014).

To gain computational time, Large Eddy Simulations (LES) consider filtered Navier-Stokes equations, resolving the largest turbulent structures and modelling the smallest turbulent length scales. In this method, the filtered and non-filtered turbulence scales interact with each other. In turbulent bedload transport, it has been mostly employed to analyze the interaction between suspended sediment transport and turbulent structures (*Schmeeckle*, 2014; *Finn et al.*, 2014b,a).

Alternative approaches of the fluid resolution are based on the averaged two-phase momentum balance equations (*Jackson*, 2000; *Drew and Passman*, 1999) or Reynolds-Averaged Navier-Stokes equations. In both cases, the average fluid phase is resolved, while the average effect of fluctuations on the mean flow is modelled. Contrary to LES, the turbulence model does not depend on the grid size, and as such does not model the interaction between grid-resolved fluid motion and sub-grid modelled turbulence. The closure complexity associated with the turbulent eddy viscosity concept ranks decreasingly from two equations model (e.g. $k-\epsilon$ (*Hsu et al.*, 2004), $k-\omega$ (*Amoudry*, 2014)) where transport equations for the turbulent kinetic energy and dissipation are solved, to mixing length formulations (e.g. *Revil-Baudard and Chauchat* (2013)) for which the eddy viscosity depends only on the distance to the boundary. Couplings with DEM are very common in the fluidized bed community (*Zhu et al.*, 2007, 2008), and started to emerge in sediment transport (*Calantoni and Thaxton*, 2008; *Duran et al.*, 2012). In both LES and averaged approaches, the coupling with the particles is handled on average through the empirical hydrodynamic forces expressions and the solid volume fraction. The former are derived from semi-empirical considerations. For example, the drag force formulation is classically determined from the asymptotic limits of laminar fluid flow (*Anderson and Jackson*, 1967; *Maxey and Riley*, 1983), completed with experimental measurements (e.g. *Schiller and Naumann* (1933); *DallaValle* (1948); *Ergun* (1952)).

Euler/Euler descriptions consider the momentum conservation of the two phases viewed as two continua in interaction, and are based on the two-phase averaged equations. The closure laws employed for the fluid phase are similar to the one adopted in Euler/Lagrange average models. The difference lies in the continuous description of the solid phase which requires modelling of the intergranular stress through the expression of the granular rheology. It is appropriate when an equivalent continuous medium can be defined for the solid phase. In the case of intense bedload, also termed sheet flow, a substantial number of particle layers are in motion.

Therefore, Euler/Euler descriptions have been mainly used for this regime, with closures for the granular stress tensor according to the main rheologies for granular media, i.e. Bagnold formulation (*Hanes and Bowen*, 1985), the $\mu(I)$ rheology (*Revil-Baudard and Chauchat*, 2013; *Aussillous et al.*, 2013), or the kinetic theory (*Jenkins and Hanes*, 1998; *Hsu et al.*, 2004).

The aim of this PhD is to propose a minimal model with reasonable computational time, to systematically analyze the granular media behavior in bedload transport. Therefore, it is necessary to model the particles with a lagrangian approach, and the fluid phase cannot be fully resolved. To obtain a global description of the fluid phase with a coupling between the two phases, the averaged approach is well suited. Such models have already been developed in the framework of intense turbulent bedload transport. The pionnering work of *Jiang and Haff* (1993) studied sheet flows, modelling the fluid as a unique slab on the top of the granular sample. The averaged streamwise fluid momentum balance was solved and the drag force applied to particles from the fluid velocity in the slab. Following the work of *Jiang and Haff* (1993), *Drake and Calantoni* (2001) divided the vertical scale in a given number of slabs. With this method, the fluid resolution is kept one dimensional (1D) along the streamwise direction, but the fluid flow is estimated all along the depth. *Drake and Calantoni* (2001) analyzed oscillatory sheet flow and evidenced the low impact of the granular contact parameters on the description. Meanwhile, *Yeganeh et al.* (2000) studied sheet flow with a coupled model, where the particles are described independently but do not interact by contact with each other. The comparison with experimental data showed the importance of the contact resolution. More recently, *Duran et al.* (2012) developed a model using DEM coupled with a unidirectional steady averaged fluid resolution. It was used to numerically study the transition from aeolian saltation to bedload transport. Bedload was considered in this paper as an extreme case of low density ratio, the fluid closures of the model being more adapted to aeolian transport.

In bedload transport, when considering few granular layers in motion, the assumption of scale separation and the definition of an equivalent continuous medium is questionable. In volume-averaged models the fluid resolution is based on the two-phase continuous equations, and assumes a well-defined solid phase continuous medium. In particular, it is important for the results to be independent from the size of the fluid mesh. These questions have not been adressed clearly in the literature, and become important when dealing with bedload transport. To overcome these limitations, a numerical model coupling DEM with a 1D fluid momentum balance has been developed, and compared with experiments. A particular care has been taken to consider both rigourously and pragmatically the averaging process and the question of scale separation.

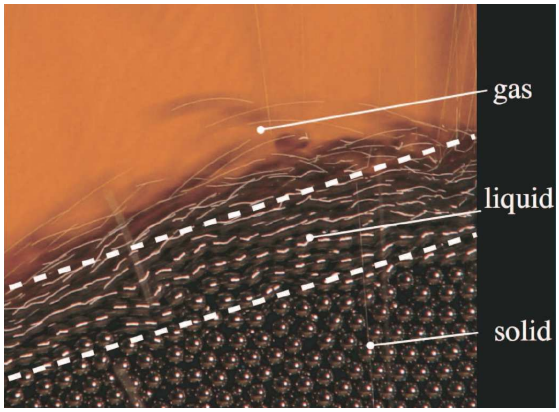

Figure 1.3: The different states of granular media coexisting in a granular flow. After *Forterre and Pouliquen* (2008).

1.3 Granular rheology

1.3.1 Dry granular media

Granular media are defined as collections of macroscopic particles interacting by contact with negligible effect of the brownian motion. They are ubiquitous in our everyday life: soil, sand, cereals (e.g. rice, pasta), sugar,... Granular media present a large variety of behaviors associated with solid, liquid, and gaseous regimes. It is possible to walk on the beach (solid), while the sand flows on an inclined plane (liquid). Shaking a few sand grains in a box creates a granular gas, where the particles interact through binary collisions. The different states can co-exist in a sample as shown in figure 1.3. In analogy with this picture of granular flow down inclines, the expressions dense and rapid granular flows are classically used to denote respectively liquid and gas granular behavior.

Regarding the huge number of particles in a granular medium[1], it is useful to adopt a hydrodynamic continuum description of the problem. The rheology of the granular material is therefore a key issue. It consists in describing the relationship between stresses and deformations. In other words, it represents how the material responses in term of stress to a given deformation, or equivalently how it deforms when submitted to a particular stress state. It is an important characteristic of the material which defines its behavior independently from the nature of the external forcing. The three different regimes of granular flows are described independently within the continuous framework. Efforts are made to unify the different views, but nothing definitive has been proposed so far. The kinetic theory, built in analogy with gaseous behavior, has proven to describe well rapid granular flows in which particles

[1]Considering a volume $V = 0.1 \times 0.1 \times 0.1m^3$ of gravel of diameter $d \sim 1mm$, the number of particles N can be approximated as: $N \sim \phi^{max} V/(\pi d^3/6) \sim 10^6$ (!), with ϕ^{max} the packing solid volume fraction

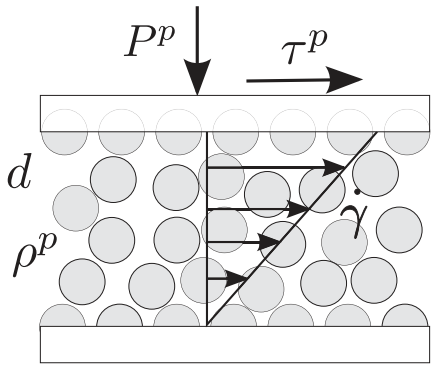

Figure 1.4: Sketch of simple shear configuration (adapted from *Andreotti et al.* (2013)). From dimensional analysis, a unique characteristic dimensionless number can be formed: $I = \dot{\gamma} d / \sqrt{P^p / \rho^p}$ called the inertial number (*Da Cruz et al.*, 2005). The granular shear stress and the particulate pressure are respectively represented by τ^p and P^p, and the shear rate is denoted $\dot{\gamma}$.

interact through binary collisions (*Campbell*, 1990; *Goldhirsch*, 2003). While similar to molecular gases, the so-called granular gases present fundamental differences due to dissipation at contact. The theory is based on the Boltzmann equation and has been generalized to inelastic frictional dilute granular media (e.g. *Garzó and Dufty* (1999)). All the kinetic theories for granular gases are based on a rigourous statistical formalism which enables to derive the hydrodynamic equations from first principles using known assumptions. While representing a considerable advantage, this formalism suffers from the constraints associated with the difficulty to solve the Boltzmann equation. In particular, it requires the hypothesis of binary collisions, and consequently excludes the description of dense granular flows. Despite this basic assumption, attempts have been made to extend the formalism to dense particulate flows (*Jenkins*, 2006, 2007; *Jenkins and Berzi*, 2010), introducing empirical correlation length in the equations. Most of the advantages of a rigourous formalism are however lost when introducing empirical equations in a context where the formalism hypotheses are not verified.

Dense granular flows are well described by the phenomenological $\mu(I)$ rheology (*Midi*, 2004; *Forterre and Pouliquen*, 2008; *Andreotti et al.*, 2013; *Jop*, 2015). The approach is different from the kinetic theory, and consists in trying to explain and understand the nature of the global trends from simple dimensional analysis combined with experiments and numerical simulations. The formalism is based on the local rheology assumption, which allows to reduce every configurations to simple shear locally. From a dimensional analysis of the simple shear configuration (see figure 1.4), a unique dimensionless number can be expressed, the so-called inertial

number (*Da Cruz et al.*, 2005):

$$I_{dry} = \frac{\dot{\gamma} d}{\sqrt{P^p/\rho^p}}, \tag{1.4}$$

where $\dot{\gamma}$ is the shear rate, and P^p is the particulate pressure. It is equivalent to the square root of the Savage number (*Savage and Sayed*, 1984), or Coulomb number (*Ancey et al.*, 1999). The inertial number can be interpreted as the ratio between a macroscopic time scale of deformation ($t_{macro} = 1/\dot{\gamma}$) and a microscopic time scale of re-arrangement under a given particulate pressure P^p ($t_{micro} = d/\sqrt{P^p/\rho^p}$). In simple shear configuration, the particle shear (τ^p) and normal (P^p) stress components are functions of the unique dimensionless number I, and scale with $\rho^p d^2 \dot{\gamma}^2$:

$$\tau^p = f_1(I)\rho^p d^2 \dot{\gamma}^2, \tag{1.5}$$

$$P^p = f_2(I)\rho^p d^2 \dot{\gamma}^2, \tag{1.6}$$

so that the stress ratio μ should depend only on I:

$$\mu(I) = \frac{\tau^p}{P^p} = \frac{f_1(I)}{f_2(I)}. \tag{1.7}$$

Inverting the expression of I (eq. 1.4) to express the particulate pressure, it follows that $f_2(I) = 1/I^2$ from equation (1.6). Consequently (from eq. 1.7): $f_1(I) = \mu(I)/I^2$. To obtain the granular rheology, in addition to the closure required for $\mu(I)$, another equation is required to determine I or P^p as a function of the hydrodynamic parameters (e.g. ϕ, $\langle v_p \rangle^s$,$\dot{\gamma}$). Indeed, the two are directly linked through the expression of the inertial number (eq. 1.4). This is handled by considering either incompressible granular flows assumption, or expressing the solid volume fraction as a function of I. Classically, the expression of the stress ratio $\tau^p/P^p = \mu(I)$ and the solid volume fraction $\phi = \phi(I)$ as a function of I are determined from experiments and numerical simulations (see *Forterre and Pouliquen* (2008) and *Jop* (2015) and references therein). They follow the typical relationships (*Jop et al.*, 2005; *Da Cruz et al.*, 2005):

$$\mu(I) = \mu_1 + \frac{\mu_2 - \mu_1}{I_0/I + 1} \tag{1.8}$$

$$\phi(I) = \phi^{max} - bI \tag{1.9}$$

where μ_1, μ_2, I_0 and b are phenomenological constants. Equation 1.9 can be inverted and gives the inertial number as a function of the solid volume fraction ϕ. Extrapolating to 3D (*Jop et al.*, 2006), the constitutive equation reads:

$$\sigma_{ij} = -P^p \delta_{ij} + \eta^p \dot{\gamma}_{ij}, \tag{1.10}$$

where $\dot{\gamma}_{ij} = \partial_i \left\langle v_j^p \right\rangle^s + \partial_j \left\langle v_i^p \right\rangle^s$, and $\eta^p = \mu(I)P^p/\sqrt{\dot{\gamma}_{ij}\dot{\gamma}_{ij}}$. In this formulation, the granular media can be seen as a complex visco-plastic fluid with a viscosity depending on the inertial number and the particulate pressure. The 1D formulation based on simple shear configuration has been shown to describe well granular problems in various configurations (see references in *Forterre and Pouliquen* (2008) and *Jop* (2015)), supporting the idea that the granular rheology is local. While the 3D tensorial generalization has been sucessfully applied to heap flow (*Jop et al.*, 2006) and laminar bedload transport (*Aussillous et al.*, 2013), some observations suggest that the stress and strain rate tensors orientation are not always aligned (*Lacaze and Kerswell*, 2009; *Cortet et al.*, 2009).

In most of the configurations encountered in realistic phenomenon, the $\mu(I)$ rheology is not describing accurately the quasi-static regime. The latter, historically studied by geomechanicians, shows rate-independent stress-strain relationship (*Muir Wood*, 1990), not compatible with the $\mu(I)$ formulation based on the shear rate. Recent developments (e.g. *Kamrin and Koval* (2012); *Bouzid et al.* (2013)) attempted to adapt the $\mu(I)$ rheology to the quasi-static regime, through the modelling of non-local effects. Those theories try to make the link between the solid and liquid behavior of granular media.

1.3.2 Immersed granular media

Based on the simple shear configuration, the $\mu(I)$ rheology has been applied and extended to account for the influence of an interstistial fluid (*Courrech du Pont et al.*, 2003; *Cassar et al.*, 2005). The dry inertial number is the ratio between a macroscopic time scale of deformation and a microscopic time scale of granular rearrangement. Therefore, the main influence of the fluid on the inertial number stands in the microscopic re-arrangement time, which is affected by the hydrodynamic forces. The macroscopic deformation time is driven by the fluid, but its effect is embedded in the shear rate so that the formulation of the macroscopic time scale is not modified. Considering the re-arrangement process, the time scale is determined by the time for a particle to fall over a diameter, under a given particulate pressure. Only the drag fluid force is considered in the analysis as the buoyancy is already taken into account through the particulate pressure. Two regimes can therefore be defined: a regime with re-arrangement time dominated by the viscous drag force, and another dominated by the inertial drag force. To avoid confusion, the latter is called turbulent regime in the present manuscript. Defining three characteristic times corresponding to the travel time over one diameter under a given particulate pressure P^p, at free-fall velocity ($t_{ff} \sim d/\sqrt{P^p/\rho^p}$), at the viscous settling velocity ($t_{visc} \sim \eta^f/P^p$), and at the turbulent settling velocity ($t_{turb} \sim d\sqrt{C_D\rho^f/P^p}$), three regimes (free-fall, viscous, turbulent) can be distinguished by two dimensionless

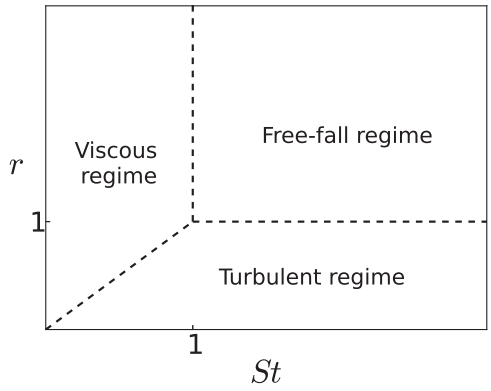

Figure 1.5: Schematic picture of the different regimes defined from the interstitial fluid influence on the granular rheology. Free-fall regime corresponds to negligible influence of the interstitial fluid, while viscous and inertial regimes correspond to local re-arrangement time respectively dominated by viscous and turbulent drag force.

numbers (see figure 1.5):

$$St = \frac{t_{ff}}{t_{visc}} = \frac{d\sqrt{\rho^p P^p}}{\eta^f}, \tag{1.11}$$

$$r = \frac{t_{ff}}{t_{turb}} = \sqrt{\frac{\rho^p}{\rho^f C_D}}. \tag{1.12}$$

The free-fall regime ($St >> 1$, $r >> 1$) corresponds to neglible influence of the interstitial fluid (i.e. dry granular media), the viscous regime ($St << 1$, $r << 1$) corresponds to a rearrangement process dominated by the viscous drag, and the turbulent regime ($St >> 1$, $r << 1$) corresponds to a rearrangement process dominated by the turbulent drag. In each regime, the results should scale with the viscous (I_{visc}), turbulent (I_{turb}), and dry (I_{dry}) inertial number respectively:

$$I_{dry} = \frac{\dot{\gamma} d}{\sqrt{P^p/\rho^p}}, \tag{1.13}$$

$$I_{turb} = \frac{\dot{\gamma} d}{\sqrt{P^p/(\rho^f C_D)}}, \tag{1.14}$$

$$I_{visc} = \frac{\eta^f \dot{\gamma}}{P^p}. \tag{1.15}$$

Using the inertial number associated with the regime considered, the classical expression of $\mu(I)$ and $\phi(I)$ can be *in principle* kept (eq. 1.8 and 1.9).
This approach has been applied with some success to various complex configurations from immersed rotating drum (*Courrech du Pont et al.*, 2003), avalanches (*Cassar et al.*, 2005; *Doppler et al.*, 2007) or granular collapse (*Izard et al.*, 2014), to annular

shear cell (*Boyer et al.*, 2011; *Trulsson et al.*, 2012) and sediment transport (*Ouriemi et al.*, 2009; *Revil-Baudard and Chauchat*, 2013; *Aussillous et al.*, 2013; *Chiodi et al.*, 2014). While the scalings are recovered, the value of the phenomenological constants in the formulations of $\phi(I)$ and $\mu(I)$ vary from one case to the other. Yet, the $\mu(I)$ approach allows to identify the key parameters from simple dimensional analysis, and applies to a wide variety of configurations.

1.3.3 Application to sediment transport

In sediment transport, the fluid flow is the main driving force of the granular medium. It can be for example gravity-driven (e.g. rivers), or due to a fluid pressure gradient (e.g. pipeline). Independently from the origin of the fluid flow, the steady state configuration can be seen as a granular medium under a given sollicitation. Therefore, it is interesting to analyze the granular rheology to characterize the process and the mechanisms at play.

Focusing on sediment transport, there exists only few contributions studying the granular rheology. *Ouriemi et al.* (2009) and *Aussillous et al.* (2013) have studied laminar bedload in closed conducts in both experiments and theoretical two-phase continuous framework. By assuming constant solid volume fraction and a limited transitional layer from dense to dilute granular flow, they showed that a simple Coulombian rheology with a constant friction coefficient gives good estimation of the solid velocity profile, while the $\mu(I)$ rheology gives excellent agreement. It is worth noting that in the laminar case, the lag between fluid and solid velocity profile is negligible (*Mouilleron et al.*, 2009; *Aussillous et al.*, 2013), the two phases being tightly coupled. In intense turbulent bedload transport, the transitional layer from dense to dilute granular flows as well as the fluid-particle velocity lag, are more important (*Sumer et al.*, 1996; *Cowen et al.*, 2010; *Revil-Baudard et al.*, 2015). Therefore, a simple Coulomb rheology is not expected to give accurate results. Focusing on turbulent bedload transport, contributions only exist on sheet flows (*Jenkins and Hanes*, 1998; *Hsu et al.*, 2004; *Capart and Fraccarollo*, 2011; *Revil-Baudard and Chauchat*, 2013; *Revil-Baudard et al.*, 2015), where the suspended load can have an important effect. Two-phase continuous simulations were performed using closures based on the kinetic theory (*Jenkins and Hanes*, 1998; *Hsu et al.*, 2004) and the immersed $\mu(I)$ rheology (*Revil-Baudard and Chauchat*, 2013). In both cases, the results were compared with experimental measurements of solid velocity profile by *Sumer et al.* (1996), and reasonable agreement were found. Further experimental investigations by *Revil-Baudard et al.* (2015) showed that the solid volume fraction profile observed experimentally was substantially different than the simulated one, and that the effective friction coefficient differs from the $\mu(I)$ rheology. While the problem is still open, this was mainly attributed to the intermittency induced by the interaction between the bed and turbulent coherent structures, which breaks down the steady state assumption of the granular rheology.

Considering steep slopes, the granular rheology has been studied at the transition from sheet flow to debris flow (*Armanini et al.*, 2005; *Larcher et al.*, 2007; *Berzi and Jenkins*, 2008; *Armanini et al.*, 2014). As the steep slopes induce wide collisional layers with relatively low particle concentration, it has mainly been analyzed in the framework of the kinetic theory. Experimental measurements at the side-wall enabled *Armanini et al.* (2005) to measure solid velocity, concentration and granular temperature depth profiles. Estimating stress profiles from the data combined with a force balance and a Coulomb criterion, they suggested the presence of a transition between a frictional and a collisional layer in the sample. Following this decomposition, a model has been proposed (*Armanini et al.*, 2014), combining the kinetic theory for elastic spheres of *Lun et al.* (1984) with a rheology of type $\mu(I)$ in the dense limit. They obtained a relatively good agreement with experimental measurements of solid volume fraction, velocity, granular temperature, and extrapolated stress tensor. Using numerical models and analytical developments associating $\mu(I)$ rheology with a simple mixing length approach in two-phase continuous framework, *Berzi and Jenkins* (2008) obtained a relatively good agreement with the experiment of *Larcher et al.* (2007) for the solid velocity, normal and shear stress profiles.
While these configurations have common points with turbulent bedload transport, no contribution has focused on the study of the granular rheology in this particular configuration.

1.4 Objective and scope

Following the work conducted at Irstea by *Bigillon* (2001); *Böhm* (2005); *Hergault* (2011) and *Frey* (2014), the goal of the present PhD is to improve the understanding of bedload transport through a granular media approach. Focusing on the granular behavior in idealized configurations allows to change the perspective from the classical bedload transport analysis and improve the understanding of the phenomenon. In this framework, a numerical model focusing on the granular phase description has been developed and used to characterize the granular phase in bedload transport.

The manuscript is structured in four chapters. First, the numerical model is presented with particular emphasis on the discrete/continuous coupling and the averaging process in the framework of bedload transport (chapter 2). In chapter 3, the proposed model is compared with both the classical transport formulas, and particle-scale depth profiles from the experiments of *Frey* (2014). A condensed version of these two first chapters is under consideration for publication in Physics of Fluids (*Maurin et al.*, 2015). The model is further employed to analyze the effect of the slope and the specific density on the sediment transport rate in chapter 4. Combined with an analytical description in the framework of continuous two-phase equations, it allows to characterize these effects in terms of sediment rate and granular flow depth structure. Lastly, the granular rheology in bedload transport is investigated from numerical simulations in chapter 5.

Chapter 2

Numerical model

To analyze the granular behavior in bedload transport, a minimal model has been developed using a DEM Lagrangian description of the granular phase, coupled with a one dimensional volume-averaged two-phase momentum equation for the fluid phase. The latter is not solved at the particle scale, and the momentum coupling is ensured in an averaged sense via semi-empirical correlations. The aim of the present chapter is to present the principles of the numerical model, and to discuss the coupling between a discrete granular phase and a continuous fluid phase within the framework of turbulent bedload transport. After briefly presenting the Discrete Element method (section 2.1) and the fluid phase description (section 2.2), the coupling between the two phases is discussed (section 2.3).

2.1 Solid phase description: Discrete Element Method

2.1.1 Principles

Discrete Element methods can be divided into two different approaches which have in common the independent description of each particle (*Radjai and Dubois*, 2011). The so-called Contact Dynamics method is based on the powerfull mathematical framework of non-smooth mechanics, neglecting the time-scale associated to elastic contact processes (*Moreau*, 1983; *Jean and Moreau*, 1992; *Brogliato*, 1999; *Radjai and Dubois*, 2011; *Maurin*, 2012). While proved to be effective (*Radjai and Dubois*, 2011), this method suffers from a complex framework which limits its use among a broader group of scientist. On the other hand, the molecular dynamics method, first introduced for the description of granular media by *Cundall and Strack* (1979), is associated with a simple explicit theoretical picture. It has historically been adapted from molecular system description, for which the interactions between the molecules are modelled using empirical molecular potential such as Lennard-Jones one (*Jones*, 1924). Similarly for an assembly of particles, the contact forces are derived from a defined contact law, function of material's parameters, particles interpenetrations and relative velocities. Limiting the effect of the interactions to neighboring par-

ticles only, Newton's equation of motion can be solved explicitely for each particle at each time step. As a direct consequence of the explicit temporal resolution of the contact process, the numerical time step is limited to very low values. The interpenetration can be viewed as the local particles deformation at contact, but is mainly an artefact to explicit and simplify the numerical resolution. In this work, the molecular dynamics approach is used, and the word DEM will be used to denote this particular approach.

The advantages of molecular dynamics lie mainly in the description of each particle's motion, and in the simplicity of the formulation. In addition, the numerous study made with DEM show that most of the time, simple contact models are sufficient to describe well the granular media behavior. This affirmation should however be taken with care, as it is not true for some particular cases (e.g. *Brodu et al.* (2015)). On the other hand, the description of all particles and the limited time step make the simulation computationally expensive. In particular, the contact detection is difficult to parallelize. Up to now, the use of DEM has been restricted to granular scale analysis, the maximum number of particles simulated being small ($\sim 10^7$) with respect to large scale problems. As a matter of comparison, $1m^3$ of coarse sand of diameter $1mm$ contains approximately 10^9 particles. It should be added that molecular dynamics has been developed for spheres, for which there are no ambiguities in the contact description. For original shapes, the geometrical definition of the contact and of the interpenetration are less obvious and requires more attention (see e.g. *Wachs* (2011); *Richefeu et al.* (2012)). An alternative approach is to consider clumps of particles (e.g. *Fukuoka et al.* (2014)), yet it is obviously computationally more demanding.

Overall, the method is particularly well suited to study the average particle-scale granular phase behavior in bedload transport. Indeed, it is able to describe accurately both isolated particles and dense granular flows. In addition, it has been shown to reproduce qualitatively size-segregation processes (*Rognon et al.*, 2007; *Calantoni and Thaxton*, 2008; *Tripathi and Khakhar*, 2011; *Hill and Tan*, 2014), that is crucial in bedload transport.

DEM is today a common tool in the granular media community. Therefore, the reader is sent back to *Šmilauer and Chareyre* (2010) for full details on the numerical implementation in the open-source code YADE[1], and to the literature for a more detailed and exhaustive description (e.g. the book of *Radjai and Dubois* (2011)). In the following, the most important components of the DEM resolution will be detailed, i.e. the resolution principles, the contact law, and the time-step determination.

[1] https://www.yade-dem.org/

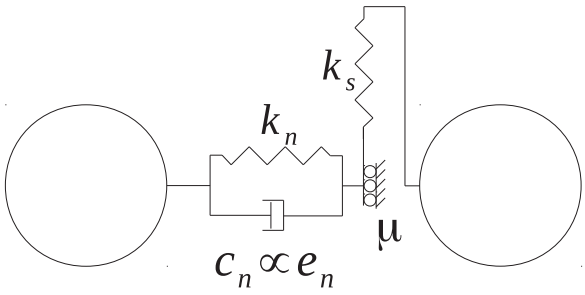

Figure 2.1: Scheme of the contact law detailing the normal and tangential model used.

2.1.2 General formulation and contact law description

For each spherical particle p at position $\vec{x}^p$ and angular velocity $\vec{\omega}^p$, Newton's second law gives the following equation of motion:

$$m\frac{d^2\vec{x}^p}{dt^2} = \vec{f}_c^p + \vec{f}_{ext} = \vec{f}_c^p + \vec{f}_g^p + \vec{f}_f^p \tag{2.1a}$$

$$\mathcal{I}\frac{d\vec{\omega}^p}{dt} = \vec{T} \tag{2.1b}$$

where $\mathcal{I}$ is the moment of inertia, $\vec{T}$ is the torque applied on the particle, $\vec{f}_c^p$ is the nearest neighbor contact forces, $\vec{f}_{ext}$ are the external body forces, i.e. in bedload: the gravity force $\vec{f}_g^p$ and the force applied by the fluid on the particle p, $\vec{f}_f^p$. The latter arises from the DEM-fluid coupling and will be detailed in subsection 2.3. As spherical particles with fluid force applied to the particle center are considered, the torque reduces to the contribution of the contact forces: $\vec{T} = \vec{x_c} \times \vec{f}_c^p$, where $\vec{x^c}$ is the vector linking particle center to the contact point. In this case, for a spherical particle, $\mathcal{I} = 2m|\vec{x_c}|^2/5$. The application of the gravity force is straightforward. The contact forces are determined from the relative displacement of the neighboring particles using a defined contact law. In bedload, there is a sharp transition between rapidly sheared particles at the interface with the fluid, and quasi-static motion inside the bed. The so-called spring-dashpot contact law used in this paper and depicted in figure 2.1, allows the description of these two types of behavior and is widely used in modelling of granular flows (e.g. *Da Cruz et al.* (2005); *Rognon et al.* (2007); *Thornton et al.* (2012)) and sediment transport (e.g. *Drake and Calantoni* (2001); *Yeganeh-Bakhtiary et al.* (2009); *Wachs* (2011); *Duran et al.* (2012); *Izard et al.* (2014)). The contact law is based on a spring of stiffness k_n in parallel with a viscous damper of coefficient c_n for the normal contact, coupled with a spring of stiffness k_s associated with a slider of friction coefficient μ^p for the tangential

contact. Therefore, the contact force depends directly on the normal and tangential interpenetration δ_n and δ_t, and on the normal relative velocity $\dot{\delta_n}$:

$$F_n = -k_n\delta_n - c_n\dot{\delta_n} \tag{2.2a}$$

$$F_t = -min(k_s\delta_t, \mu^p F_n) \tag{2.2b}$$

Where δ_t is initialized to zero when the two particles enter into contact. The constant normal restitution coefficient defined by the linear elastic spring and viscous damping (*Schwager and Pöschel*, 2007), together with the friction coefficient, can be evaluated experimentally (e.g. for subaqueous contact (*Gondret et al.*, 2002)). The spring normal and tangential stiffnesses can be considered as numerical parameters in the rigid grain limit, i.e. when the stiffnesses are much greater than the maximum pressure undergone by the particles (*Roux and Combe*, 2002; *Da Cruz et al.*, 2005): $k_n/(P^p d) > 10^4$. This is equivalent to require the particles interpenetration to be small with respect to their diameters.

2.1.3 Numerical resolution

The DEM open-source code YADE (*Šmilauer et al.*, 2010) has been used to simulate the granular phase. The code is in C++ with a python interface, and includes a number of useful predefined contact laws and functions in addition to the DEM solver. The project YADE was originally developed in the framework of geomechanics, and has been partly adapted to dynamical situations during this PhD. The numerical resolution being the same, the adaptations realized in the framework of this PhD, pertained mainly to the contact law[2] formulation, and the time step evaluation.

The time integration is explicit with a second order centered scheme (*Bathe and Wilson*, 1976) to ensure energy conservation. Resolution time steps for explicit integration schemes are bounded in order to have stable integrations. As the present model accounts only for nearest neighbor interactions, the time step should be lower than the propagation time of the fastest wave over a particle diameter. The latter is determined by the system of particles linked through springs and dampers. A simplified approach has been adopted, considering the networks of springs and dampers as decoupled. Similarly to *Catalano* (2012) (pp. 84, see also *Catalano et al.* (2014)), the time step is given by the minimum between the one associated with the system of springs only $t_{springs}$ (*Chareyre and Villard*, 2005) and the one with the system of dampers only $t_{dampers}$. The evaluation of the time step has been implemented in YADE, generalizing an existing function[3]. It determines the time step $t_{springs}$ from the eigenvalues of the stiffness matrix for the springs network. The same approach

[2]named $Law2\_ScGeom\_ViscElPhys\_ViscEl\_Basic$ in YADE
[3]named GlobalStiffnessTimeStepper

has been applied to the system of dampers. A safety coefficient of 0.7 has been introduced to take into account the possible coupling effects between the springs and dampers systems, leading to: $dt = 0.7\ min(t_{springs}, t_{dampers})$. No numerical stability issue has been faced using this method. For more details on the method and on the determination of the stiffness and damping matrix, see *Catalano* (2012) (pp. 84).

2.2 Fluid phase

In the present work, the goal is to focus on granular processes in the framework of bedload transport. In addition, the model has to be computationally efficient, limiting the simulation time to 24/48h, in order to be able to analyze systematically the influence of the granular parameters. As a consequence, a simple average 1D description with a mixing length turbulence model has been adopted. It allows to fulfill the above criteria, while keeping energy conservation of the system in an average sens. Also, it is appropriate to model boundary layer in unidirectional flows. The exact formulation, and the resolution details are given below.

2.2.1 Fluid phase formulation

The fluid phase model is based on spatially averaged two-phase momentum equations developed in details in the articles of *Anderson and Jackson* (1967) and *Jackson* (1997), and in the book of *Jackson* (2000). It is inspired from the one-dimensional Euler-Euler model proposed by *Revil-Baudard and Chauchat* (2013) to deal with turbulent unidirectional sheet-flows. Recalling the main properties of the weighting function $\mathcal{G}$ and the fluid phase and particle phase average (resp. $\langle\rangle^f$ and $\langle\rangle^p$), the classical volume averaged equations of motion are detailed.
In the framework of the volume average two-phase equations, the arbitrary weighting function $\mathcal{G}$ should be positive, indefinitly derivable and normalized over the whole space V, so that:

$$\int_V \mathcal{G}(\vec{y})dV_y = 1. \tag{2.3}$$

It defines the fluid $\langle\gamma\rangle^f$ and particle phase $\langle\chi\rangle^p$ averaging of respectively a fluid and particle point properties γ and χ:

$$\epsilon(\vec{x},t)\,\langle\gamma\rangle^f(\vec{x},t) = \int_{V_f(t)} \gamma(\vec{y},t)\mathcal{G}(\vec{x}-\vec{y})dV_y, \tag{2.4}$$

$$n(\vec{x},t)\,\langle\chi\rangle^p(\vec{x},t) = \sum_{p\infty} \chi^p \mathcal{G}(\vec{x}-\vec{x^p}), \tag{2.5}$$

where the integral is made on the volume occupied by the fluid $V_f(t)$, and the sum over all the particles. The fluid volume fraction ϵ and number of particle per unit

volume n are defined as:

$$\epsilon(\vec{x},t) = \int_{V_f(t)} \mathcal{G}(\vec{x}-\vec{y})dV_y, \tag{2.6}$$

$$n(\vec{x},t) = \sum_{p\infty} \mathcal{G}(\vec{x}-\vec{x^p}). \tag{2.7}$$

Providing that there exists a separation of scales between the macroscopic length scale of the problem L, the length scale associated with the weighting function l and the particle diameter d, *i.e.* $L >> l >> d$, it is possible to derive the following fluid equation for a general incompressible fluid flow (*Jackson*, 2000):

$$\rho^f \epsilon \left[\frac{\partial \langle u_i \rangle^f}{\partial t} + \langle u_j \rangle^f \frac{\partial \langle u_i \rangle^f}{\partial x_j} \right] = \frac{\partial S_{ij}^f}{\partial x_j} - \frac{\partial R_{ij}^f}{\partial x_j} + \rho^f \epsilon g_i - n \left\langle f_{f\,i}^p \right\rangle^p, \tag{2.8}$$

where ρ^f is the fluid density, S_{ij}^f and R_{ij}^f denote the ij components of respectively the effective fluid stress tensor and the Reynolds stress tensor, $\langle u_i \rangle^f$, $n \left\langle f_{f\,i}^p \right\rangle^p$, and g_i are the i-th component of respectively the average fluid velocity, the average fluid-particle interaction force, and the gravity vector. For equilibrium bedload transport, using the symmetries of the problem, the system can be considered as unidirectional. The equation therefore reduces to its streamwise component x, and depends only on the vertical position z:

$$\rho^f \epsilon \frac{\partial \langle u_x \rangle^f}{\partial t} = \frac{\partial S_{xz}^f}{\partial z} - \frac{\partial R_{xz}^f}{\partial z} + \rho^f \epsilon g_x - n \left\langle f_{f\,x}^p \right\rangle^p, \tag{2.9}$$

The major difference with the continuous two-phase model proposed by *Revil-Baudard and Chauchat* (2013) and with Euler/Euler models in general, is that in the present model the average fluid-particle interaction $n \langle f_x \rangle^p$ and solid volume fraction $\phi = 1 - \epsilon$ are obtained from a spatial averaging of the DEM solution, whereas they are otherwise obtained by solving continuous momentum balance and mass conservation equations. Equation (2.9) requires closures for the effective fluid stress tensor, the Reynolds stress tensor and the average fluid-particle interaction forces. Before detailing these closures in the next subsections, the validity of the presented equations in the framework of bedload transport is discussed.

2.2.2 Scale separation in bedload transport

The fluid equation is valid only providing that there is separation of scales between the macroscopic length scale associated to the problem L, the weighting function length scale l and the particle diameter d, i.e. $L >> l >> d$. Under bedload conditions, due to the sharp transition occurring at the sediment bed interface in the wall-normal direction, the associated macroscopic length scale of the phenomenon L

is lower than the particle diameter d. Therefore, it is possible to define the weighting function such that $L >> l$, but not to have separation of scale with respect to the particle diameter because $L < d$. This is a common problem in free-surface granular flows, as the flow depth considered are usually of the order of few grain sizes, whereas the flow characteristics (e.g. velocity, solid volume fraction) exhibits strong vertical gradients between the bottom boundary and the free-surface. Therefore, the vertical length scale of the weighting function l_z should be lower than the particle diameter in order to accurately resolve the vertical gradients of the averaged solid phase variables. This is necessary in order to define a mesh-independent averaging. Indeed, increasing the wall-normal weighting function length scale l_z in such system, smoothes indefinitely the averaged profiles evaluated, which therefore depends on l_z.

Although this problem is a key issue for Eulerian/Lagrangian modelling, it has not been clearly adressed in the literature, to the best of our knowledge. To overcome this lack of description, the equation derivation is undertaken here from the local expression of Navier-Stokes equation using only the assumption of scale separation between the phenomenon and the weighting function length scale $L >> l$. For conciseness, the full derivation of the equation is detailed in appendix A, and only the results are discussed in the present section. From appendix A, the volume-averaged momentum balance fluid equation reads in this framework:

$$\rho^f \epsilon \left[\frac{\partial \langle u_i \rangle^f}{\partial t} + \langle u_j \rangle^f \frac{\partial \langle u_i \rangle^f}{\partial x_j} \right] = \frac{\partial (\epsilon \langle \sigma_{ij} \rangle^f)}{\partial x_j} - \frac{\partial R_{ij}^f}{\partial x_j} + \rho^f \epsilon g_i - \sum_{p\infty} \int_{s_p(t)} \mathcal{G}(\vec{x} - \vec{y}) \sigma_{ij}(\vec{y}, t) n_j dS_y, \quad (2.10)$$

where $\langle \sigma_{ij} \rangle^f$ is the average fluid stress tensor, σ_{ij} is the local fluid stress tensor, $\sum_{p\infty}$ represents a sum on all the particles, and n_j is the normal to the surface of particle p. This equation has to be compared with the classical equation (2.8). The differences stands in the average fluid stress tensor and the fluid-particle interaction term. As expressed in *Jackson* (1997), the general fluid-particle interaction term of equation (2.10) represents the integral of the traction force mutiplied by the weighting function taken at the particle surface element. On the other hand, the fluid-particle interaction term of equation (2.8) is defined by:

$$n \left\langle f_{f\,i}^p \right\rangle^p (\vec{x}, t) = \sum_{p\infty} \mathcal{G}(\vec{x} - \vec{x_p}) \int_{s_p(t)} \sigma_{ij}(\vec{y}, t) n_j(\vec{y}, t) dS_y, \quad (2.11)$$

which represents the average taken at the particle center, of the traction force integral over the particle surface. The latter is what is usually thought as the average fluid-particle interaction force. Providing separation of scales between the weighting function characteristic scale and the particle diameter ($l >> d$), it is possible to show

that the general fluid-particle interaction term reduces to the average fluid-particle interaction force, plus two second-order terms (see appendix A). The latter two have been showed analytically to lead to Einstein's effective viscosity in the fluid stress tensor for the case of dilute Stokesian particles (*Jackson*, 1997). They can therefore be included in the effective viscous fluid stress tensor.

The lack of scale separation introduces uncertainties on the formulation of the effective fluid stress tensor and on the average fluid-particle interaction term. These two terms can be considered as empirical closure laws as they are derived based on experimental data. Furthermore, the viscous stress tensor contribution plays a weak role in the present turbulent bedload configuration, so that the associated closure is not of primary importance for the problem. In order to model the present complex configuration with simplified tools, it is necessary to make approximation, and the separation of scales between the weighting function $\mathcal{G}$ and the particle diameter d will be supposed. For the fluid resolution, the classical equation (2.9) will be used in the following. While it is clear from the above analysis that it influences the fluid-particle interaction term, it is difficult to determine *a priori* the impact of this assumption. Consequently, it is fundamental to perform experimental comparisons in order to ensure that the results obtained are consistent, and describe accurately the main bedload transport mechanisms.

2.2.3 Closures

In the fluid equation (2.9), omitting the fluid-particle interaction term, closure laws for the effective viscous shear stress S^f_{xz} and the Reynolds shear stress R^f_{xz} need to be prescribed. In the present model, the fluid is considered as Newtonian, so that:

$$S^f_{xz} = \rho^f \epsilon \nu^e \frac{d\left\langle u_x \right\rangle^f}{dz}, \tag{2.12}$$

where ν^e is the Einstein's effective fluid kinematic viscosity (*Einstein*, 1906) defined by:

$$\nu^e = \nu^f \left(1 + \frac{5}{2}\phi\right). \tag{2.13}$$

The Reynolds shear stress, representing the vertical turbulent mixing of horizontal momentum, is modeled based on the eddy viscosity concept (ν^t) with a mixing length formulation:

$$R^f_{xz} = \rho^f \ \nu^t \frac{d\left\langle u_x \right\rangle^f}{dz} \quad \text{with} \quad \nu^t = \epsilon \ l_m^2 \left| \frac{d\left\langle u_x \right\rangle^f}{dz} \right|, \tag{2.14}$$

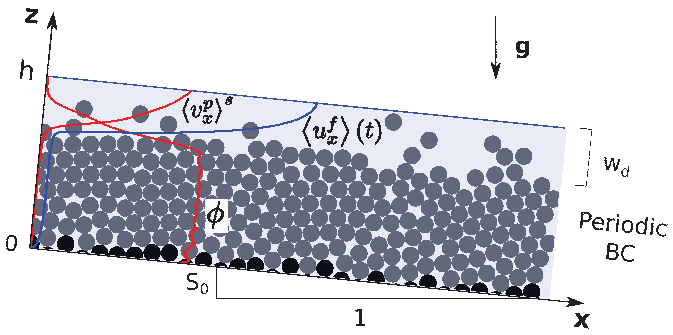

Figure 2.2: Sketch of the problem representing the axes and the variables used in the model: the water surface position h, the water depth w_d, the slope $S_0 = \tan\alpha$, the gravity vector $\vec{g}$, as well as the profiles of average streamwise fluid and solid velocities (resp. $\langle u_x \rangle^f$ and $\langle v_x^p \rangle^s$), and solid volume fraction ϕ. Streamwise periodic boundary conditions (BC) are used for the solid phase DEM description as indicated on the scheme.

in which the mixing length (l_m) formulation proposed by *Li and Sawamoto* (1995) is used:

$$l_m(z) = \kappa \int_0^z \frac{\phi^{max} - \phi(\zeta)}{\phi^{max}} \, d\zeta, \tag{2.15}$$

where $\kappa = 0.41$ represents the von Karman constant. This simple formulation allows recovery of the two expected asymptotic behaviors: the mixing length is linear with z when the solid phase volume fraction vanishes (*i.e.* clear fluid), as in the law of the wall (*Prandtl*, 1926), and the mixing length is zero when the solid phase is at its maximum packing fraction, *i.e.* the turbulence is fully damped inside the dense sediment bed. As explained in *Revil-Baudard and Chauchat* (2013), this formulation is well adapted for boundary layer flows above mobile rough beds. Indeed, the integral of the solid volume fraction predicts a non zero mixing length at the transition between the granular dominated and turbulent dominated layers. Also, with this formulation no virtual origin for the mixing length has to be prescribed.

2.3 DEM-fluid coupling

To solve the fluid equation and the DEM, the fluid-particle interaction force and the exact formulation of the averaging need to be prescribed. After detailing these two points (section 2.3.1 and 2.3.2), a simple model is introduced to simulate fluid velocity fluctuations (section 2.3.3). Details about the numerical resolution are given in the last subsection (section 2.3.4).

2.3.1 Averaging procedure

When separation of scales between the weighting function $\mathcal{G}$ and the particle diameter d exists, the particle phase averaging (eq. 2.5) is equivalent to the solid phase averaging. As explained previously (section 2.2.2), there is no such separation of scales under bedload conditions. Accordingly, the solid phase averaging is used in this model instead. Following *Jackson* (1997), the local solid phase average $\langle\chi\rangle^s(\vec{x},t)$ of a solid phase point property $\chi(\vec{x},t)$ reads:

$$\langle\chi\rangle^s = \frac{1}{\phi(\vec{x},t)}\sum_p \int_{V_p} \chi(\vec{y})\mathcal{G}(\vec{x}-\vec{y})dV_y, \tag{2.16}$$

where the local solid volume fraction $\phi(\vec{x},t)$ is given by:

$$\phi(\vec{x},t) = \sum_p \int_{V_p} \mathcal{G}(\vec{x}-\vec{y})dV_y. \tag{2.17}$$

To be consistent with the discretization of the fluid problem, it is convenient to define a cuboid weighting function. In order to fulfill the normalization property, a three-dimensional step function is chosen for the weighting function:

$$\mathcal{G}(\vec{x}) = \begin{cases} \dfrac{1}{l_x\ l_y\ l_z} & \text{for } |x| \le l_x/2,\ |y| \le l_y/2,\ |z| \le l_z/2 \\ 0 & \text{otherwise} \end{cases} \tag{2.18}$$

In the present model, the average fluid description is 1D so that it depends only on the wall-normal component, z. The solid averaging can therefore be performed on the full width L_y and length L_x of the configuration: $l_x = L_x$ and $l_y = L_y$. With this specification and the formulation of the weighting function, the solid phase averaging of a solid phase property χ^p constant within each particle, reduces to:

$$\langle\chi\rangle^s(z) = \frac{1}{\phi(z)} \sum_{\{p|z^p\in[z-l_z/2;z+l_z/2]\}} \tilde{V}^p\chi^p, \tag{2.19}$$

where z is the wall-normal position of the averaging, $\tilde{V}^p$ is the fraction of the particle volume contained in the slice of height l_z centered around z, and the solid volume fraction $\phi(z)$ reads:

$$\phi(z) = \frac{1}{l_x l_y l_z} \sum_{\{p|z^p\in[z-l_z/2;z+l_z/2]\}} \tilde{V}^p. \tag{2.20}$$

We recover here the averaging formulation of *Hill et al.* (2003) that is convenient to compute since the volume of a slice of spheres can be evaluated analytically in cylindrical coordinate. The averaging box height l_z is imposed by the vertical grid size of the fluid problem and no overlapping between the different slices is allowed.

To be consistent with the derivation of the two-phase equation, the averaging formulation should be independent of the choice of the weigthing function and the results should converge with decreasing wall-normal length scale. It is equivalent to having a statistical representativity inside each discretized cell. This can be checked with spatial convergence analysis. The latter should be performed in each different situation considered and it will be detailed in the next chapter for application to bedload transport (Chapter 3, section 3.1.2 and 3.2.1).

2.3.2 Fluid forces

In bedload, particles are surrounded by a fluid flow, and thus undergo various hydrodynamic forces. The force applied by the fluid on a single particle $\vec{f}_f^p$ introduced in equation (2.1) is defined as the integral over the particle surface S_p of the total fluid stress σ_{ij}, pressure and shear stress, acting on the particle surface (*Jackson*, 1997):

$$f_{f\,i}^p = \int_{S_p} \sigma_{ij} n_j dS_p \tag{2.21}$$

In the present model, the fluid flow is not solved at the particle scale, therefore the hydrodynamic forces cannot be computed explicitly, and need to be prescribed through semi-empirical formulas based on averaged fluid variables. The expression of the fluid force on a particle in an averaged flow is not trivial. The form and origin of the forces are usually determined from the asymptotic limit of laminar (*Anderson and Jackson*, 1967; *Maxey and Riley*, 1983) or inviscid flow (*Schmeeckle et al.*, 2007). The link between the two regimes is made using empirical correlations, e.g. the drag force can be derived exactly in the case of laminar fluid, and is obtained from experimental measurement at higher Reynolds number and in different geometries or confinement (*Ergun*, 1952; *DallaValle*, 1948; *Schiller and Naumann*, 1933; *Richardson and Zaki*, 1954). The formulations of the fluid force applied on each particle can therefore be assimilated as closure laws of the model. Recalling the main contributions, the fluid-particle force reads (*Schmeeckle et al.*, 2007):

$$\vec{f}_f^p = \vec{f}_b^p + \vec{f}_D^p + \vec{f}_m^p + \vec{f}_l^p + \vec{f}_{am}^p + \vec{f}_{Ba}^p, \tag{2.22}$$

where $\vec{f}_b^p$ is the generalized buoyancy force, $\vec{f}_D^p$ is the drag force, $\vec{f}_m^p$ is the Magnus lift force, $\vec{f}_l^p$ is the shear-induced lift force, $\vec{f}_{am}^p$ is the added mass force, $\vec{f}_{B,}^p$ is the Basset history force.

In this PhD, the goal is to establish a minimal model to describe bedload transport, consequently only the main hydrodynamic forces have been considered. The added mass force has not been included as it depends on the local fluid acceleration, that is not solved in the present fluid model. In bedload transport, the dense particle flow induces a very perturbed fluid flow that should erase history effects, so that

Basset force are neglected. The Magnus lift has also been neglected on the basis of former results (*Niño and García*, 1998). Lastly, *Ji et al.* (2013) numerical results exhibit a non-negligible importance of the shear-induced lift force with respect to drag and buoyancy. However, *Schmeeckle et al.* (2007) showed experimentally that the usual formulation of the lift (*Wiberg and Smith*, 1985), derived using the inviscid flow assumption, is not valid close to the threshold of motion. Based on these observations and the absence of alternative formulation, it has been decided not to include the lift force at this stage.

Therefore, the force $\vec{f}_f^p$ induced by the fluid on a particle p appearing in the DEM model (eq. 2.1), reduces to buoyancy $\vec{f}_b^p$ and drag $\vec{f}_D^p$:

$$\vec{f}_f^p = \vec{f}_b^p + \vec{f}_D^p. \tag{2.23}$$

According to *Jackson* (2000) the generalized buoyancy force is defined as:

$$\vec{f}_b^p = V^p \left(-\vec{\nabla} \langle P \rangle^f + \vec{\nabla}. \left\langle \overline{\overline{\tau^f}} \right\rangle \right), \tag{2.24}$$

where $\langle P \rangle^f$ is the averaged fluid pressure and $\left\langle \overline{\overline{\tau}} \right\rangle^f$ is the averaged viscous shear stress tensor taken at a larger scale than the particle scale. This definition generalizes the so-called Archimedes buoyancy force for hydrostatic problems to cases where the fluid volume is submitted to a macroscopic deformation at a scale much larger than the particle scale *i.e.* the fluid deformation viewed by the particles can be considered as constant. Similarly to *Revil-Baudard and Chauchat* (2013), it has been found that the viscous stress tensor contribution is negligible with respect to the pressure contribution in bedload transport. The force applied on each particle can then be approximated by the usual buoyancy expression, which is equivalent to consider a buoyant weight in the vertical direction.
The drag force exerted by the fluid flow on a single particle is classically expressed as:

$$\vec{f}_D^p = \frac{1}{2} \rho^f \frac{\pi d^2}{4} C_D \left|\left| \langle \vec{u} \rangle^f_{\vec{x^p}} - \vec{v^p} \right|\right| \left(\langle \vec{u} \rangle^f_{\vec{x^p}} - \vec{v^p} \right), \tag{2.25}$$

where C_D is the drag coefficient, and $\langle \vec{u} \rangle^f_{\vec{x^p}} - \vec{v^p}$ is the relative velocity between the particle and the average fluid velocity taken at the position of the particle center. The *DallaValle* (1948) formulation together with a *Richardson and Zaki* (1954) correction is used in the present model for the drag coefficient:

$$C_D = \left(0.4 + \frac{24.4}{Re_p} \right) (1 - \phi)^{-\zeta}, \tag{2.26}$$

where $Re_p = || \langle \vec{u} \rangle^f_{\vec{x^p}} - \vec{v^p} || d / \nu^f$ is the particulate Reynolds number for particle p. This simple formulation has been used in different two-phase flow models for sediment transport applications (*Revil-Baudard and Chauchat*, 2013; *Jenkins and*

Hanes, 1998; *Hsu et al.*, 2004). The Richardson-Zaki correction $(1-\phi)^{-\zeta}$ accounts for the hindrance effect induced by the local particle concentration, and allows to recover realistic fluid velocity in the particle bed. The exponent has been set to $\zeta = 3.1$ in reference to *Jenkins and Hanes* (1998).
Equations (2.25) and (2.26) are used to compute the drag force on each individual particles in the DEM model (equation (2.1)), while the effect of buoyancy is taken into account through the vertical buoyant weight.

The phase interaction term in the fluid momentum balance (eq. 2.9) then reduces to the momentum transfer associated with the hydrodynamic forces. In the present 1D fluid resolution, it is expressed as the average number of particles $n = \phi/V_p = 6\phi/\pi d^3$ multiplied by the streamwise solid-phase averaged associated force. For the drag force, it reads:

$$n \left\langle f_{D_x}^p \right\rangle^s = \frac{3}{4} \frac{\phi\, \rho^f}{d} \left\langle C_D \left|\left| \langle \vec{u} \rangle_{x\vec{p}}^f - \vec{v^p} \right|\right| \left(\langle u_x \rangle^f - v_x^p \right) \right\rangle^s . \tag{2.27}$$

The drag coefficient C_D depends on the relative velocity through the particle Reynolds number, so that it should be included in the spatial averaging. Indeed, for a non-uniform spatial distribution of relative velocity, $\left\langle (\langle u_x \rangle^f - v_x^p)^a \right\rangle \neq \left\langle \langle u_x \rangle^f - v_x^p \right\rangle^a$, if $a \neq 1$.

2.3.3 Velocity fluctuation model

The proposed average model for the fluid phase does not account for the fluid turbulent velocity fluctuations. These fluctuations are known in particular to influence the particle threshold of motion. In order to account for these turbulent processes in the average fluid model, it is possible to use a random walk model. The level of description ranges from simple Discrete Random Walk (DRW) without space-time correlations, to more complex continuous random walk model including space-time correlation and derived from Langevin equation (*Dehbi*, 2008). In order to simply account for the fluctuations, a DRW inspired from *Zannetti* (1986) has been introduced. It consists in associating a random velocity fluctuation with each particle for a given duration, as a function of the local turbulent intensity and turbulent time scale. The fluctuations are not correlated in space, nor in time, and the model is built so that the Reynolds shear stress definition is consistent between the average fluid model and the DRW model:

$$\overline{u_x^{f\prime} u_z^{f\prime}} = -\frac{R_{xz}^f}{\rho^f \epsilon}, \tag{2.28}$$

where the $\bar{\bullet}$ represents an averaging operator in time (Reynolds averaging).

From experimental measurements in open-channel flows (*Nezu*, 1977; *Nezu and*

Nakagawa, 1993), it has been observed that the magnitude of fluctuations in the streamwise direction is roughly two times larger than in the vertical direction. With this constraint the following DRW model for the streamwise component $(u_x^{f'})^p$ and the normal component $(u_z^{f'})^p$ of the fluid velocity fluctuation associated with each particle p is proposed:

$$(u_z^{f'})^p = \lambda_1 \tag{2.29a}$$

$$(u_x^{f'})^p = -(u_z^{f'})^p + \lambda_2, \tag{2.29b}$$

where λ_1 and λ_2 are two Gaussian random numbers of zero mean and of standard deviation σ. This standard deviation is obtained from the local value of the Reynolds shear stress at the position of the particle center $\sigma = \sqrt{\frac{R_{xz}^f}{\rho^f \epsilon}(\vec{x^p})}$. The velocity fluctuations are updated every τ_t, defined as the turbulent eddy turn over time, which can be estimated as $\tau_t = w_d/U^f$ where w_d is the water depth, and U^f is the average fluid velocity. These velocity fluctuations are added to the average fluid velocity in the drag force expression (eq. 2.25), both in the DEM simulation, and for the evaluation of the average drag term in the fluid resolution.

2.3.4 Numerical resolution strategy

In this subsection the resolution of the fluid equation is detailed. As expressed in equation (2.9), the fluid resolution reduces to:

$$\rho^f \epsilon \frac{\partial \langle u_x \rangle^f}{\partial t} = \frac{\partial S_{xz}^f}{\partial z} - \frac{\partial R_{xz}^f}{\partial z} + \rho^f \epsilon g_x - n \left\langle f_{f\,x}^p \right\rangle^p .$$

The equation can be expressed as a function of the average fluid velocity, by developing the closure for the viscous stress tensor (eq. 2.12), the Reynolds stress tensor (eq. 2.14), and the fluid-particle interaction force (eq. 2.27). It reads:

$$\epsilon \rho^f \frac{\partial \langle u_x \rangle^f}{\partial t} = \rho^f \frac{\partial}{\partial z} \left[\left(\epsilon\, \nu^e + \nu^t \right) \frac{\partial \langle u_x \rangle^f}{\partial z} \right] + \epsilon \rho^f g\, \sin\alpha - \beta^s \left(\langle u_x \rangle^f - \langle v_x^p \rangle^s \right), \tag{2.30}$$

where β^s is given by:

$$\beta^s = \frac{3}{4} \frac{\phi\, \rho^f}{d} \frac{\left\langle C_D \left|\left| \langle \vec{u} \rangle_{\vec{x^p}}^f + (\vec{u}^{f'})^p - \vec{v^p} \right|\right| \left(\langle u_x \rangle_{\vec{x^p}}^f + (u_x^{f'})^p - v_x^p \right) \right\rangle^s}{\langle u_x \rangle^f{}_{\vec{x^p}} - \langle v_x^p \rangle^s}. \tag{2.31}$$

The expressions of the fluid-particle interaction force and of the eddy viscosity ν^t (eq. 2.14), lead to non-linearities in terms of the average fluid velocity. In order to simplify the numerical resolution, the equation is linearized by considering β^s and ν^t as explicit. At each resolution step, these two terms are evaluated from the previous time step.

The formulation of the average fluid-particle interaction term ensures strictly the same average momentum transfer in the discrete solid phase problem and in the continuous fluid phase one. In the resolution, the volume fraction and the fluid-solid interaction terms are computed from spatial averaging of the DEM simulation. The fluid velocity fluctuations are taken into account in the average drag term. For the fluid resolution, equation (2.30) is discretized using implicit finite differences for the diffusion and the drag terms. The resulting tridiagonal system is solved using a double-sweep algorithm (*Chauchat et al.*, 2013, 2015). The fluid phase resolution period τ_f should be small enough compared with the particle relaxation time $\tau_D = (\beta^s)^{-1}$. This characteristic time corresponds to the time needed by a particle initially at rest to reach its steady state velocity in a constant fluid flow. In general, the fluid resolution period is much bigger than the DEM time-step. In the open-source code YADE, a set of functions[4] have been implemented during the PhD, in order to apply efficiently the fluid forces to each particle and evaluate the average contributions necessary for the fluid resolution.

The simulation loop is described in figure 2.3. It is schematically composed of three interdependent parts with different resolution time steps: DEM with the lowest time step Δt_s, the fluid solver with a fixed resolution period of τ_f, and the fluid velocity fluctuation model with a changing period τ_t. At each time step n, for each particle p, drag and buoyancy forces are computed from the position $\mathbf{x}^p \mid^n$ and velocity of the particle $\mathbf{v}^p \mid^n$, the associated average fluid velocity $\left\langle u_x^f \right\rangle \mid^n (z^p)$ and fluid velocity fluctuation $(\mathbf{u}^{f'})^p \mid^n$. Then, a classical DEM step is performed taking into account the hydrodynamic forces on each particle, from which we obtain the new positions $\mathbf{x}^p \mid^{n+1}$ and velocities $\mathbf{v}^p \mid^{n+1}$ of the particles. If the period for fluid resolution τ_f is surpassed, a spatial averaging is carried out to determine the solid volume fraction $\phi \mid^{n+1}$ and average drag force $\langle f_{D,x} \rangle^s \mid^{n+1}$ at each grid point of the fluid phase model (wall-normal direction only). Then, the fluid equation is solved and determines the new average fluid velocity field $\left\langle u_x^f \right\rangle \mid^{n+1}$. The same is done for the model of fluid velocity fluctuations which is ran if its resolution period τ_t is surpassed. Lastly, the quantities are actualized and the process returns to the beginning of the time loop for a new time step up to the end of the simulation.

2.4 Conclusion

A numerical model to study bedload transport focusing on the granular phase has been presented. Adapted closures have been adopted and the coupling between the discrete granular phase and the continuous fluid phase has been detailed. In particular, the lack of scale separation has been discussed, and it has been shown to

[4] named HydroForceEngine in YADE

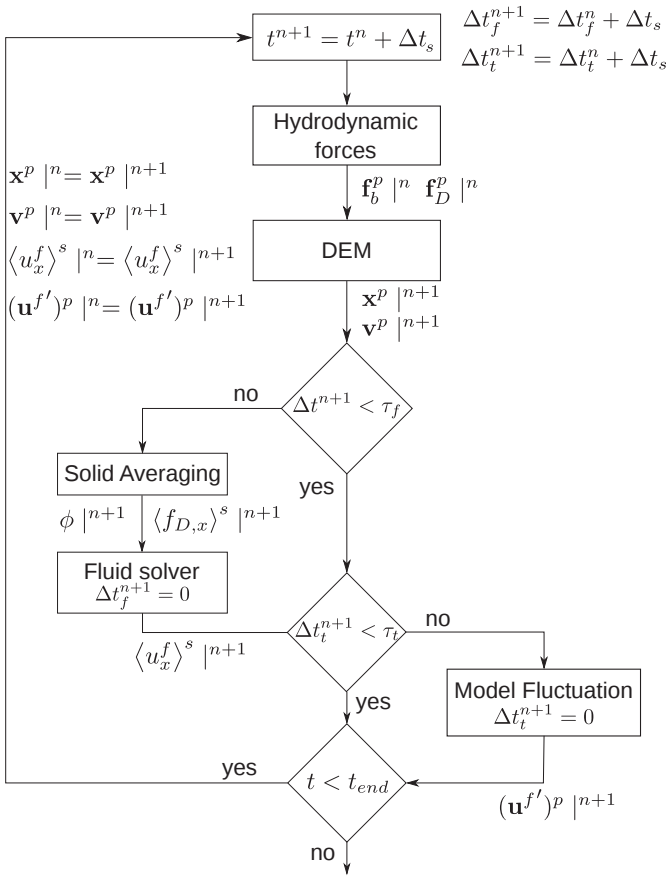

Figure 2.3: Simulation loop of the model. The quantities with superscript p are evaluated for each particle, while $|^n$ express the time step n at which the quantities are defined.

influence mainly the fluid-particle interaction force. Also, an averaging formulation as well as a model to describe the fluid velocity fluctuations have been proposed. In order to validate the assumptions and the modelling choices made, the model will be compared with experiments in the following chapter.

Chapter 3

Experimental comparison and sensitivity analysis

Turbulent bedload transport associates collective granular behaviors with turbulent fluid flows, two phenomena of which the description remains a scientific challenge. In order to simplify the analysis, the present work focuses on the granular phase behavior and describes the fluid flow based on an averaged description. Experimental comparisons are required to validate the modelling assumptions and evaluate the accuracy of the current numerical description of the problem. Therefore, this chapter is dedicated to experimental comparisons and sensitivity analysis. It is divided into two parts corresponding to different situations and levels of description. First, particle-scale comparisons of solid depth profiles in a quasi-2D framework are considered (section 3.1). The original experiment of *Frey* (2014) allows to measure average solid velocity, volume fraction and transport rate density profiles from particle tracking. To complement this refined comparison in a particular configuration, 3D bi-periodic simulations are considered and compared with the classical sediment transport rate curve as a function of the Shields number (section 3.2). In addition, the range of studied Shields number is extended from near incipient motion to intense bedload transport, to give a global picture of the applicability of the model and compare the results with the literature. The 3D results are finally analyzed in term of solid depth profiles to give more insights into the results.

3.1 Experimental comparison with quasi-2D depth profiles

The goal of the model is to describe the granular phase behavior in bedload transport. It is thus important to consider comparisons with particle-scale experimental data. Combined Particle Image Velocimetry (PIV)/Particle Tracking Velocimetry(PTV) measurements have been performed in 3D laminar bedload experiments (*Mouilleron et al.*, 2009; *Aussillous et al.*, 2013). Up to now however, no such 3D

measurement exists for turbulent bedload transport, even if a recent publication (*Ni and Capart*, 2015) suggests it will be the case in the near future. Similarly, while it is technically possible to obtain 3D bedload experimental data from Magnetic Resonance Imaging (*Penn*, 2014), it has not been performed yet. In this PhD, it has been decided to compare the model with the quasi-2D experiment of *Frey* (2014), which permitted tracking of all particles by considering a channel of one diameter width. The presence of the author of the experimental data in the supervision of the PhD, has simplified importantly the data obtention and the harmonization of the post-processing.

3.1.1 Experimental configuration

The experiment of *Frey* (2014) consisted in a quasi-2D ideal case of mountain stream bedload transport on a steep slope. The setup, depicted in figure 3.1, has been the basis of numerous contributions in the past ten years at Irstea Grenoble, with in particular the PhD work of *Bigillon* (2001), *Böhm* (2005) and *Hergault* (2011). It is composed of a 2 m long inclined channel of slope $S_0 = 0.1$, and width $6.5mm$. Water ($\rho^f = 1000\ kg/m^3$) flows in the open-channel and entrains the spherical glass particles ($\rho^p = 2500\ kg/m^3$) of diameter $d = 6\ mm$. Particles are introduced at the inlet and create an erodible bed thanks to the obstacle placed at the outlet. The number of particle layers is controlled by the height of this obstacle. The channel bottom is made of metal half-cylinders of diameter d, fixed at a random elevation between $-2.75\ mm$ and $2.75\ mm$ with steps of $0.5\ mm$ to break clusterization. The particle feeding rate is controlled with a special bead distributor, and the flow rate is adjusted in order to reach transport equilibrium, i.e. feeding rate equal to the sediment transport rate at the outlet without having aggradation and degradation of the bed. The free-surface fluid flow is turbulent ($Re = U^f w_d/\nu^f \sim 10^4$), hydraulically rough ($Re_p \sim 10^3$), and supercritical ($Fr = U^f/\sqrt{g w_d} \gtrsim 1$). The particle settling velocity ($w_s = 0.54\ m/s$) and the suspension number $S^* = w_s/u_*$[1] are high. Therefore, the particles are weakly influenced by the turbulent structures and there is no suspended load. A camera is placed perpendicular to the sidewall, filming a window of 25x8 cm^2 at 131.2 frames per second (see an example of camera acquisition in figure 3.2). Due to the one particle diameter width of the channel, image processing (*Böhm et al.*, 2006) enables particle trajectories to be followed inside the measurement window, and the average free-surface elevation to be evaluated. In each experiment, once bedload is at equilibrium, data acquisition time lasted 60 s. Experimental data are averaged in the same way as in the model using the definition of section 2.3. The order of magnitude of the main dimensionless numbers associated with the experiment are shown in table 3.1. The Stokes number, comparing the inertia of the particle with the fluid viscosity, is given by $St = \rho^p v^p d/(9\eta^f)$.
The experimental comparison focuses on three runs with different Shields number ranging from 0.076 to 0.106 (see table 3.2). They differ in terms of particle feed-

[1] Equivalent to the Rouse number

Table 3.1: Characteristic values of the main dimensionless numbers.

θ	Re	Re_p	Fr	ρ^p/ρ^f	St	S^*
0.05-0.1	10^4	10^3	$\gtrsim 1$	2.5	$10^2 - 10^3$	$2 - 10$

Table 3.2: Experimental run characteristics, with h the water free surface position, N_l the number of bead layers, $\dot{n}$ is the sediment transport rate, and θ the Shields number.

Run	h (cm)	N_l	$\dot{n}$ (b/s)	θ
Exp6	5.3	7.08	6.67	0.076
Exp14	5.7	7.37	13.68	0.100
Exp20	5.9	7.30	19.74	0.106

ing rate, water supply, number of bead layers, and give equilibrium transport rates of about 7, 14 and 20 beads per second. The number of bead layers N_l, is expressed from the the volume occupied by the particles at rest V_{tot}^{part}, which reads $V_{tot}^{part} = \phi^{max} N_l d l_x l_y$, where l_x and l_y are the system length and width. It represents the height of the particle bed at rest, in terms of diameter. While the three cases are close one from the other regarding the Shields number, the differences between the runs represent a good test to quantify the accuracy of the numerical model. For more details on the experiments, the reader is refered to the original experimental article of *Frey* (2014).

3.1.2 Numerical adaptation

General parameters

To compare the model with the experiments, the simulation needs to match the experimental set-up. The analysis focuses on the bulk equilibrium properties of bedload transport. Therefore, periodic boundary conditions are considered in the streamwise direction for the present quasi-2D case. The periodic characteristic of the granular phase, does not enable us to impose a feeding rate. Instead, the density of beads per unit length (equivalent to N_l) and the free-surface position h are imposed. Indeed, there is a unique couple, slope-water depth, corresponding to the transport equilibrium. It can be reproduced by fixing h, N_l and the slope S_0 for a periodic sample. The bottom is made of fixed particles, randomly generated with the experimental characteristics described in the previous subsection. For the fluid resolution, a no-slip boundary condition is imposed at the channel bottom, and the free-surface elevation measured in the experiment is prescribed. The latter is done by forcing the shear stress (i.e. the fluid velocity derivative) to zero. The rest of

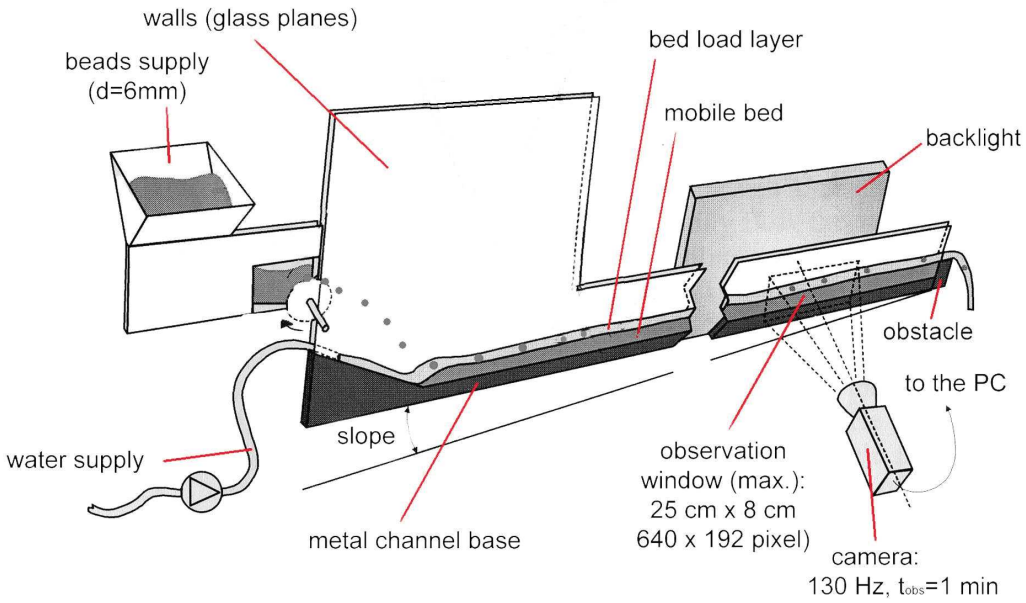

Figure 3.1: Experimental setup scheme, modified from *Böhm et al.* (2006) and *Hergault et al.* (2010). The limited channel width implies a quasi-2D granular flow, permitting particle tracking in the observation window filmed by the camera.

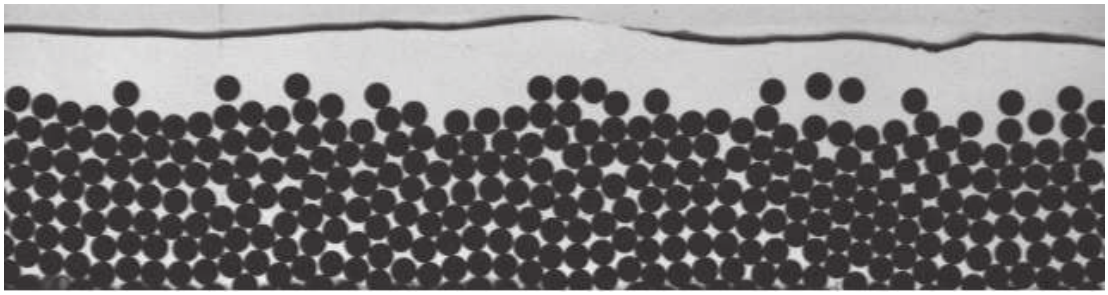

Figure 3.2: Example of camera acquisition from the experimental setup of *Frey* (2014) depicted in figure 3.1.

Table 3.3: Model input parameters for the contact law and the fluid resolution. k_n and k_s are respectively the normal and tangential contact stiffnesses, e_n and μ^p denote the restitution and friction coefficients, κ is the Von Karman constant, ζ the Richardson-Zaki exponent, ϕ^{max} the bed maximum solid volume fraction, τ_f the fluid resolution period and τ_{dem} an order of magnitude of the DEM time step.

k_n	k_t (N/m)	e_n	μ^p	κ	ζ	$\phi^{max}(2D/3D)$	$\tau_f(s)$	$\tau_{dem}(s)$
$10^4 P^p\|^{max} d$	$k_n/2$	0.5	0.4	0.41	3.1	0.51/0.61	10^{-2}	$\sim 10^{-4}$

the experimental parameters, such as the particle diameter, density and material, or the width of the channel, are set in the simulation at their known experimental values, in order to keep the same dimensionless numbers values.

For each run the channel bottom is newly generated randomly, and particles are deposited under gravity. Once the system with fluid resolution is at equilibrium, the simulations last 100 seconds and measurements are made every 0.1 second. This corresponds to the particle relaxation time to the fluid velocity $\tau_D = \beta^{-1}$ (eq. 2.31), and is characteristic from the evolution of the system. For the post-processing of both experimental and numerical results, the averaging definition is taken consistently with the numerical resolution from equation (2.19).

In agreement with *Revil-Baudard and Chauchat* (2013), it has been observed that the fluid effective rheology does not influence the fluid behavior, which is dominated by the turbulent shear stress. Therefore, a clear fluid viscosity is used. The restitution coefficient was set to $e_n = 0.5$ based on measurements made in the experimental channel considered (*Bigillon*, 2001). The simulation are performed in the rigid grain limit, i.e. in the range where the contact stiffness is high enough in order for the deformation/interpenetration of the particles to be low and the results to be insensitive to this parameter. As formalized by *Roux and Combe* (2002), this is ensured by requiring that the ratio between the normal contact stiffness k_n and the maximum particle pressure $max(P^p)$ times the particle diameter, is greater than 10^4:

$$\frac{k_n}{max(P^p)\ d} > 10^4. \tag{3.1}$$

The relatively low maximum particle pressure in our problem scale with the gravity, and can be estimated from a vertical hydrostatic assumption as:

$$max(P^p) = (\rho^p - \rho^f)\phi^{max} N_l\ g \cos\alpha\ d. \tag{3.2}$$

The contact stiffness can then be artificially reduced to gain computational time. It has been checked that a stiffness of:

$$k_n = 10^4\ (\rho^p - \rho^f)\phi^{max} N_l\ g \cos\alpha\ d^2, \tag{3.3}$$

was sufficient for the results to be insensitive to this parameter. The tangential stiffness k_t should be taken of the same order of magnitude than the normal one, and has been shown to have no influence on the results in this range (*Campbell*, 2002; *Silbert et al.*, 2001). The friction coefficient is taken as $\mu^p = 0.4$, of the order of magnitude of the value for dry glass beads. The main parameter values of the simulations are summarized in table 3.3. The simulation results correspond to the application of the experimental conditions, and are not fitted with any parameter afterwards.

Wall friction correction

In the experiment the width to depth ratio is low. Consequently, the fluid flow is expected to have a complex 3D structure. However, flow measurements in this channel showed that the fluid velocity has a typical logarithmic profile (*Frey and Reboud*, 2001). In addition, the stated aim of the model is to focus on the granular phase. Therefore, only a correction for the fluid dissipation at the smooth lateral walls is taken into account in the model. The correction was included as a source term in the fluid averaged momentum balance resolution (eq. 2.30), taking the form of a friction term evaluated from the classical Einstein method. The dissipation term can be written at each elevation z as:

$$\tau_z^{ff} = \frac{f_w}{8}\ \rho^f\ (\langle u_x \rangle_z^f)^2\ \frac{2}{W}, \tag{3.4}$$

where f_w is the wall friction factor and W is the channel width. The wall friction factor is evaluated from the formulation of *Graf and Altinakar* (1998), given by solving the following equation:

$$\frac{1}{f_w} = 2\ log_{10}(Re\sqrt{f_w}) + 0.32, \tag{3.5}$$

where $Re = \langle u_x \rangle_z^f\, W/\nu^f$. The simplicity of the wall correction with respect to the complexity of the situation in terms of fluid flow, leads to the necessity to tune its intensity in order to match the experiments. The intensity has been tuned from the mutliplication of the logarithmic term by a factor kept constant along the three experimental comparisons.

Convergence analysis

As stated in the model formulation, the fluid momentum balance equation is valid providing there is separation of scale between the wall-normal length scale of the phenomenon L, and the one associated with the weighting function, l_z (see section 2.2.2). It is the case if the results are independent from l_z. Therefore, the results should be shown to converge with decreasing l_z, and to be statistically representative inside each averaging cell. These two conditions are studied in the present

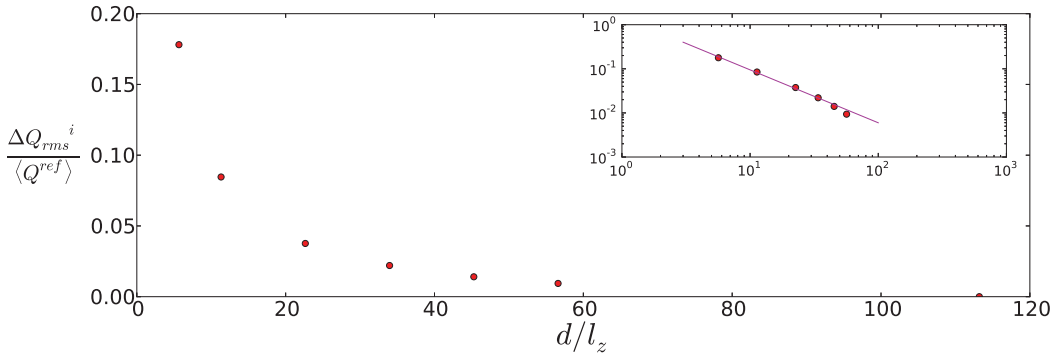

Figure 3.3: Convergence of the sediment transport rate density profile, as a function of the inverse weighting function wall-normal length scale, for the quasi-2D case Sim20. The vertical axis represents the deviation with respect to the reference configuration ($d/l_z = 100$) as defined in equation (3.6). A trend $(d/l_z)^{-1}$ is shown in the logarithmic inset (–).

subsection, through the convergence analysis with variation of the weighting function length scale l_z and the periodic cell length.

The analysis focuses on the sediment transport rate density profile, which is representative of the variable of interests in bedload transport. In order to characterize the convergence, an indicator quantifying the deviation with respect to a reference case is defined. It is given as the root mean square (RMS) of the difference between the considered transport rate density profile and the reference one:

$$\frac{\Delta Q_{rms}{}^{i}}{\langle Q^{ref} \rangle} = \frac{\sqrt{\frac{1}{N}\sum_{z=0}^{N}(\langle Q \rangle_z^i - \langle Q \rangle_z^{ref})^2}}{\frac{1}{N}\sum_{z=0}^{N}\langle Q \rangle_z^{ref}}, \tag{3.6}$$

where the RMS $\Delta Q_{rms}{}^{i}$ is normalized by the averaged transport rate of the reference configuration $\langle Q \rangle^{ref}$, N is the number of averaging cells in the depth, $\langle Q \rangle_z^i$ and $\langle Q \rangle_z^{ref}$ are the values of transport rate in the cell z for respectively the considered case and the reference case. This parameter quantify the gap between the considered transport rate density profile and the reference one. Two similar profiles would lead to a low value, while two different ones would result in a high RMS deviation. The indicator can be seen as a global evaluation of the local deviation from the reference profile.

Wall-normal weighting function The convergence of the transport rate density profile is studied with decreasing wall-normal weighting function length scale. The periodic cell chosen is long enough in order to ensure the statistical representativity in each cell, for each wall-normal length scale. The depth profiles are extracted from

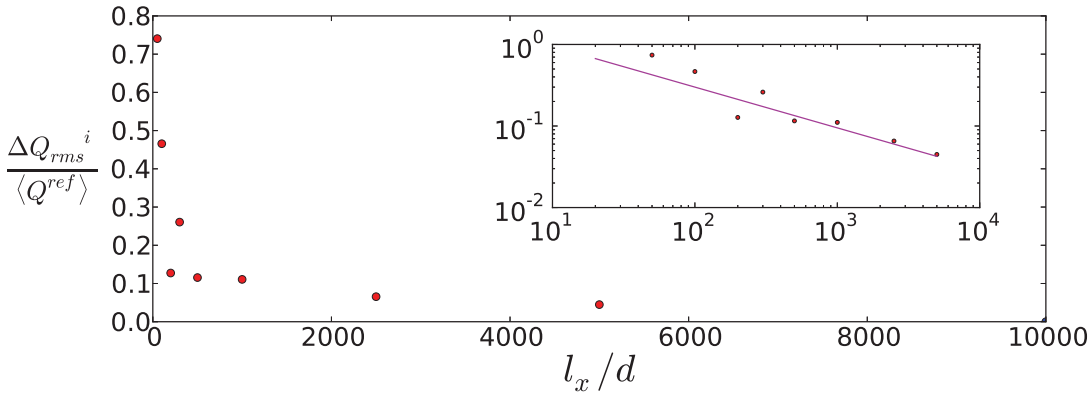

Figure 3.4: Convergence of the sediment transport rate profile as a function of the periodic cell size considered for the quasi-2D case. The vertical axis represents the deviation with respect to the reference configuration ($l_x = 10000d$), as defined in equation (3.6). A trend $l_x^{-0.5}$ is shown in the logarithmic inset (–).

the same simulation, averaging with different wall-normal length scale. The latter varies from d/5 to d/100. Figure 3.3 presents the RMS deviation of the transport rate density profiles for each case. The reference case is taken as the finer mesh profile ($l_z = d/100$). The RMS deviation is plotted as a function of the inverse of the dimensionless wall-normal length scale, i.e., as a function of the number of mesh point contained in a particle diameter, the higher d/l_z, the finer the mesh. A power-law slightly superior than one $(d/l_z)^{-1}$ is observed. For $l_z < d/30$ ($d/l_z > 30$), the results can be considered as converged. This value is similar to the one observed by *Hill et al.* (2003) ($l_z < d/20$) in bedload transport at low Shields number, and $l_z = d/30$ will be adopted for all the simulations.

Streamwise cell length The spatial convergence of the results is analyzed with respect to the streamwise periodic length cell l_x. The convergence analysis is made with respect to the reference state chosen as $l_x/d = 10000$, corresponding to a physical periodic length cell of $60m$ for particles of $6mm$ and about 80000 particles in the simulation. Different simulations have been performed with a periodic streamwise length cell l_x of respectively 50, 100, 200, 300, 500, 1000, 2500 and 5000 d.

Figure 3.4 shows the normalized RMS deviation with respect to the reference configuration as a function of the simulation streamwise periodic length cell. The results show a convergence as a function of cell length l_x of the order of $l_x^{-0.5}$. Considering the best trade off between computational time and deviation observed, a value of $l_x/d = 1000$ has been chosen in the following. The variation from one run to the other due to the generation of the random fixed bottom and the gravity deposition, has been evaluated by simulating ten cases with the exact same parameters. The maximum value of RMS deviation has been found to be 0.10 (not shown). It will be considered in the following as the reproducibility deviation, i.e. under this value

Table 3.4: Results of the sensitivity analysis to the fluid resolution period τ_f, for the case Sim20. The measured Shields number θ^*, transport rate $\dot{n}$, and RMS deviation of the transport rate density profile with respect to the case Ref. $\frac{\Delta Q_{rms}{}^i}{\langle Q^{ref} \rangle}$, are given for each case.

Case	τ_f (s)	θ^*	$\dot{n}$ (b/s)	$\frac{\Delta Q_{rms}{}^i}{\langle Q^{ref} \rangle}$
Sim20	10^{-2}	0.06	26.38	0
$\tau_f = 10^{-3}$	10^{-3}	0.06	24.49	0.10
$\tau_f = 10^{-1}$	10^{-1}	0.06	26.15	0.05
$\tau_f = 1$	1	0.06	25.46	0.08
$\tau_f = 10$	10	0.06	25.98	0.06

no differences between the profiles can be interpreted.

Fluid resolution period

The DEM time step is particularly low (typically $10^{-4}s$) and the evolution of the granular medium over this time is limited. Consequently the fluid resolution period τ_f can be taken bigger than the solid time step. The former should be defined smaller than the characteristic time of evolution of the granular medium. The latter is difficult to evaluate analytically. Therefore, a sensitivity analysis has been performed on the fluid resolution period. The latter has been observed to affect the transient evolution toward equilibrium, leading to numerical instabilities when increased. In order to focus on the effect of steady state average properties, a fluid resolution period of $\tau_f = 10^{-2}s$ is first adopted to reach equilibrium within each sample. Then, the resolution period is switched to the studied value. The results are shown in table 3.4 in terms of RMS deviation of the transport rate density profile with respect to the reference configuration Sim20 for which $\tau_f = 10^{-2}s$. It includes $\tau_f = 10^{-3}s$, $10^{-1}s$, $1s$ and $10s$. The results exhibit no dependence on the fluid period resolution in the range $10^{-3}s$ to $10s$. Indeed, for all cases, the values of the RMS deviations, are below or equal to the reproducibility deviation. Therefore, the fluid resolution period does not have an influence on the averaged equilibrium results, within the considered range. It reflects the low variability of the averaged solid profiles with time, at steady state. A fluid resolution period of $\tau_f = 10^{-2}s$ has been adopted, as it is a good compromise between numerical stability and computational cost.

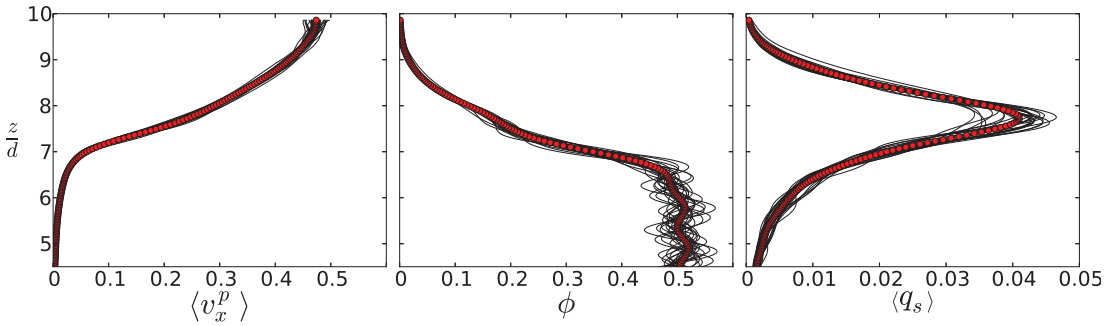

Figure 3.5: Depth profiles of averaged solid velocity (m/s), volume fraction (m^3/m^3) and sediment transport rate density (m/s) for the case Sim20 with a periodic length cell of 1000 d. The different black lines (–) correspond to different post-processing averaging performed in the experimental condition, i.e. over boxes of streamwise length 40 d and time-averaged over 60 s. The full red dots (•) correspond to the averaging as performed for the simulation in general, with a period of averaging of 100 s and a streamwise length of the size of the periodic cell. The figure shows the order of magnitude of the variability of the experimental results due to the limited spatio-temporal window of averaging.

3.1.3 Results

Experimental comparison

In bedload transport, one of the main challenges lies in the prediction of the integrated transport rate as a function of the flow rate. The experiment of *Frey* (2014) was designed to give more insight into the granular behavior, and to focus on the depth profile in bedload transport at the particle scale. The integrated transport rate per unit width Q_s, can be expressed as a function of the average transport rate density $\langle q_s \rangle$, which is the product of the average solid velocity $\langle v_p \rangle$ and solid volume fraction ϕ (*Frey*, 2014; *Lajeunesse et al.*, 2010):

$$Q_s = \int \langle q_s \rangle^s \, dz = \int \langle v^p \rangle^s \, \phi dz. \tag{3.7}$$

Considering steady unidirectional bedload transport, $\langle v^p \rangle^s$, ϕ, and $\langle q_s \rangle^s$ depend only on the depth z. Accordingly, the experimental comparison will focus on the depth profiles of the solid volume fraction, the average solid velocity, and the sediment transport rate density. The latter will be called transport rate profile for simplicity. For each simulation, the Shields number has been evaluated from two different methods. A macroscopic approach, following *Frey* (2014): $\theta = \rho^f R h_b S_0 / [(\rho^p - \rho^f) d]$, with Rh_b the hydraulic radius. And a determination from the fluid bottom shear stress defined by the friction velocity u_*: $\theta^* = \rho^f u_*^2 / [(\rho^p - \rho^f) g d]$, where u_* is given by the maximum turbulent shear stress $u_* = \sqrt{max(R_{xz}^f(z))}$. θ^* was only evaluated in

Table 3.5: Experimental and numerical run characteristics. The free surface position h and the number of bead layers N_l are both measured in the experiment and imposed in the simulation. $\dot{n}$ is the measured transport rate, θ and θ^* the Shields numbers respectively based on macroscopic flow parameters and turbulent shear stress profile. The latter has only been determined in the simulations.

Run	h (cm)	N_l	$\dot{n}$ (b/s)	θ	θ^*
Exp6	5.3	7.08	6.67	0.076	-
Sim6	5.3	7.08	10.15	0.083	0.031
Exp14	5.7	7.37	13.68	0.100	-
Sim14	5.7	7.37	18.13	0.120	0.048
Exp20	5.9	7.30	19.74	0.106	-
Sim20	5.9	7.30	26.38	0.130	0.061

the simulation. This formulation avoids the use of the macroscopic determination of the Shields number, which is sensitive to the water depth evaluation and the type of wall correction considered.

In the previous subsections, no experimental or numerical error has been introduced. The order of magnitude of this dispersion has been evaluated numerically. Figure 3.5 exhibits the depth profiles of the solid volume fraction, the solid streamwise velocity, and the solid transport rate, for the same simulation with different post-processing averaging properties. The fluid mechanics convention is used, where the depth is represented on the y-axis while the quantities of interest are represented on the x-axis. The simulation corresponds to the case Sim20 in table 3.5, considering a periodic length cell of $l_x = 1000\ d$. The figure shows the variability of the results when the averaging cell length is taken equal to the experimental one ($40\ d$) at different position in the channel. This dispersion is greater than the evaluated experimental uncertainty, and than the numerical variability due to the size of the periodic cell. The latter two will be consequently ignored in the comparison, and the variability observed on figure 3.5 will be taken as error bars.

The three different experiments detailed in table 3.5 are considered for experimental comparison. The slope is the same and equilibrium transport rate ranges from 6 to 20 $beads/s$. The differences in the input parameters between the runs lie in the water surface position h and the number of particle layers N_l. The different experimental cases represent a good test to evaluate the sensitivity to the parameters and the ability of the model to reproduce different experimental conditions. The macroscopic results presented in table 3.5 show that the integrated transport rates $\dot{n}$ are in good agreement with the experiment even if slightly overestimated. Considering the Shields number, the two different methods of evaluation lead to an over-estimation using the macroscopic formulation θ, and an under-estimation

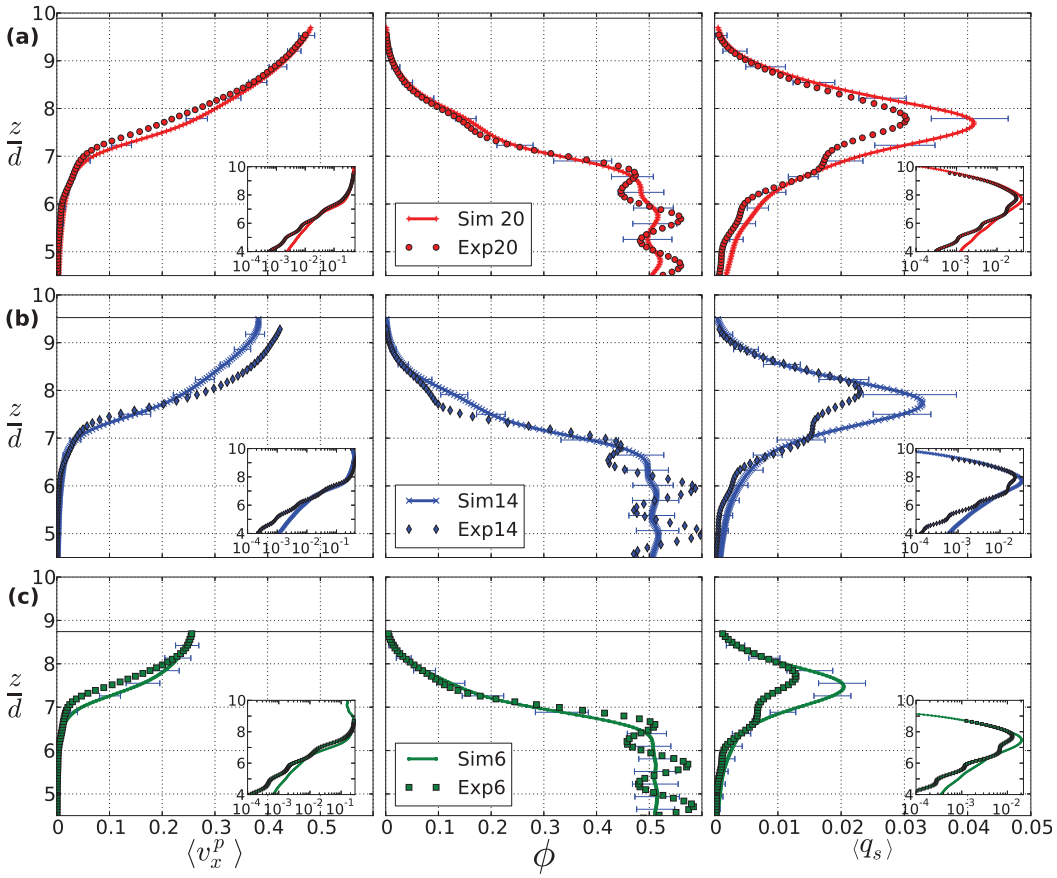

Figure 3.6: Experimental comparison for the different cases presented in table 3.5: (a) Case 20, (b) Case 14, (c) Case 6. The figure shows for each case the depth profiles of the average streamwise solid velocity (m/s), solid volume fraction, and sediment transport rate density (m/s). The full symbol (●, ♦,■) represents the experimental results from *Frey* (2014) while the empty linked one represents the simulation (+, x,·). The black line represents the imposed free surface position. The error bars show the estimated variability of the experimental results due to the limited measurements window length (see figure 3.5).

using the formulation based on the turbulent shear stress θ^*. This underlines the complexity to evaluate the Shields number in the present case, especially considering the macroscopic formulation which is very sensitive when dealing with steep slopes and small water depth. The trends observed with both formulations are good, and the values have the same order of magnitude than the experiment. In the following, we will use θ^* in order to avoid the somehow arbitrary determination of the water depth. Using this definition, the value observed for case 6 is below the classical critical Shields number ($\theta_c^* \sim 0.04$). It should however be kept in mind that the present quasi-2D mono-disperse bed is less resistant, and that the critical Shields number is accordingly lowered. To summarize, the general trends observed for the macroscopic parameters are in good agreement with the experiments. These results

show that the proposed model is able to reproduce the experimental sensitivity to the water free-surface position and to the number of bead layers.

Figure 3.6 shows the solid depth profiles of velocity, volume fraction and transport rate density, for the three experimental comparisons. The global trends from one case to the other are well reproduced by the model, and the shape of the simulated curves are close to the experimental ones. Focusing on the transport rate density profiles, the value of the peak is slightly overestimated in each case, while the rest of the curve is in very good agreement with experiments. We note an overestimation of the exponential decrease in the bed, weakly affecting the total sediment transport rate. The oscillations present in each experimental solid volume fraction profile, are representative of the limited size of the experimental averaging window, and impact the sediment transport rate density profiles. These features are therefore not reproduced in the simulation, and the comparison should be considered with respect to the average trend. For the solid volume fraction profile, the agreement between simulation and experiments is excellent for case 6 and 20, while a discrepancy is observed at the interface in case 14. The solid velocity profiles show a good prediction of the maximal velocity, and of the depth structure. The overestimation of the sediment transport rate peak is shown to correspond to an overestimation of the solid volume fraction in case 14, and of solid velocity in case 6 and 20.

Considering the comparison for the three different cases, with respect to the simplicity of the fluid description and the goal of describing the average solid behavior, the agreement with the experiments is good. The values of the integrated transport rate are close to the experimental ones and the sensitivity to the experimental parameters such as the free-surface position or the number of bead layers has been well reproduced. The comparison of the averaged solid depth profiles of the solid velocity, the solid volume fraction and the transport rate shows that the model is able to reproduce the particle-scale trends observed experimentally, and the variation between the three different runs.

Sensitivity analysis

In order to evaluate the robustness of the experimental comparison, a sensitivity analysis is performed considering the different granular and fluid physical parameters. In the following, the discrete character of the depth profiles will not be shown anymore, and lines will be used for clarity. Meanwhile, it should be kept in mind that the curves are obtained from discrete average profiles.

Importance of the fluid velocity fluctuations The influence of the fluid turbulent velocity fluctuations model is evaluated by comparing the results of simulation Sim20 with a simulation without the Discrete Random Walk (DRW) model (figure 3.7 and respectively cases Ref. and fluct. in table 3.6). The negligible difference observed on the profiles, and the RMS deviation lower than the one associated with

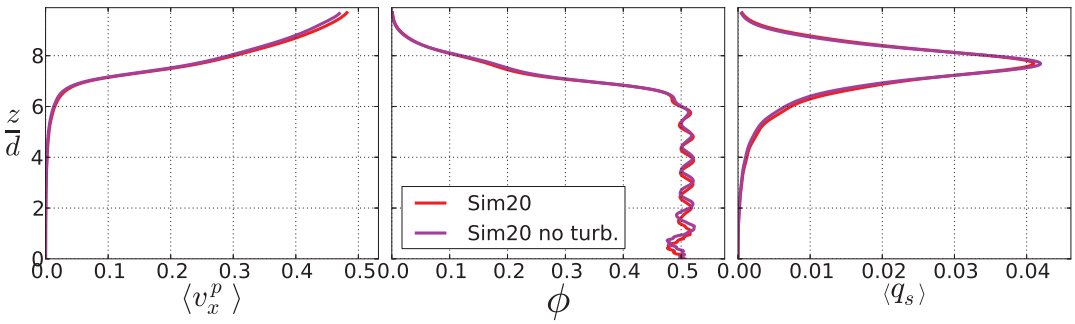

Figure 3.7: Effect of the fluid turbulent fluctuation model on the average solid depth profiles of velocity, volume fraction and transport rate density, for the quasi-2D case Sim20.

the reproducibility (table 3.6), show that the turbulence model has a negligible impact on the average granular phase behavior in this configuration. The same test has been performed for the case Sim6, which corresponds to a Shields number closer to the threshold of motion. The results give a fundamental difference between the two simulations since the case without fluctuations resulted in no transport rate (not shown as not relevant), while the case with fluctuations gives transport rate of 6.83 beads per seconds (Sim6 in table 3.5). The fluctuations model is therefore necessary to reproduce the lowest Shields number experimental case Exp6.

Hindrance correction effect In the formulation of the drag interaction force, a correction to account for hindrance effect has been introduced. It has been decided to use a formulation of Richardson-Zaki because it depends directly on the solid volume fraction and allows to recover the right behavior of both close packed particles and isolated particles in clear fluid. The influence of this parameter has been tested considering the case Sim20 (see table 3.6), in order to understand its role in the model. Figure 3.8 presents the fluid and solid depth profiles for two cases with and without the hindrance correction. The fluid velocity without correction is of the order of 0.17 m/s. With the correction accounting for hindrance effects, the fluid velocity drops down to about 0.04 m/s. The order of magnitude of the drag coefficient predicted using the *Richardson and Zaki* (1954) correction is comparable to the one predicted by *Ergun* (1952)'s drag law, which has been established from experiments of inertial flows in porous media. Figure 3.8 also shows the effect on the solid depth profiles. As it can be seen, the differences are weak and almost only located at the top of the profiles, where the very low solid volume fraction ensures a low impact on the sediment transport rate. The hindrance correction is therefore of secondary importance regarding the solid phase description. It is however important in the description of the fluid velocity profile in the bed, which can have an important impact on cases with low particle density.

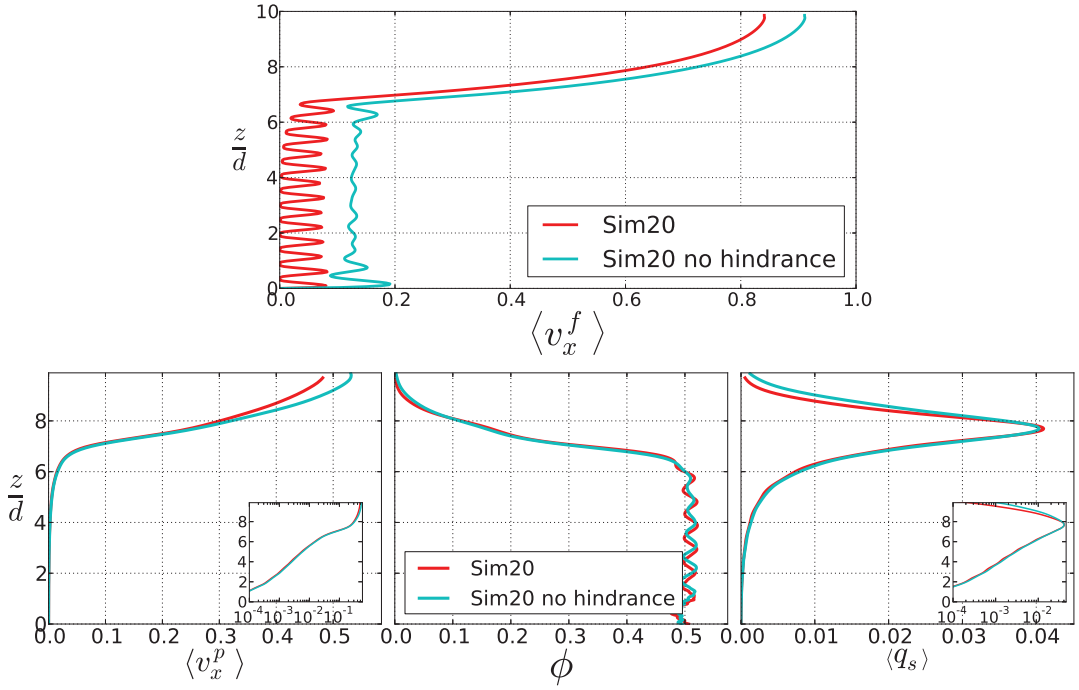

Figure 3.8: Effect of the hindrance correction on the fluid and solid depth profiles for quasi-2D case Sim20.

Granular interactions The effect of the restitution coefficient has been studied for case Sim20. Figure 3.9 shows the solid depth profiles for restitution coefficient $e_n = 0.01$, 0.25, 0.5, 0.75 and 1. The profiles only weakly depend on the restitution coefficient values in the realistic range $e_n \in [0.25, 0.75]$. The two extreme cases 0.01 and 1 show more pronounced differences even if it is not modifying fundamentally the results. The solid velocity profile is weakly impacted and does not show any clear trend as a function of the restitution coefficient. The influence on the solid volume fraction is not very important, a slight increase in concentration in the upper part of the profile is observed when the restitution coefficient increases. The low value of the solid volume fraction at this position (under 0.1), suggests that this increase is linked with an increase in saltation[2]. The transport rate density profile exhibits more differences, with an increase in the bed for both extreme cases. Surprisingly, the transport rate density inside the bed, and consequently the integrated sediment rate (table 3.6) are more important for the case without rebound than for the one with no contact dissipation. We will come back on this surprising result in next section (3.2).

The effect of the friction coefficient is shown in figure 3.10, in which the reference case Sim20 ($\mu^p = 0.4$, Sim20 in table 3.6), is plotted together with the results

[2]Here and in the the rest of the manuscript, the term "saltation" refers to the one employed in the bedload transport community and denotes small particle jumps with rebounds on the granular bed

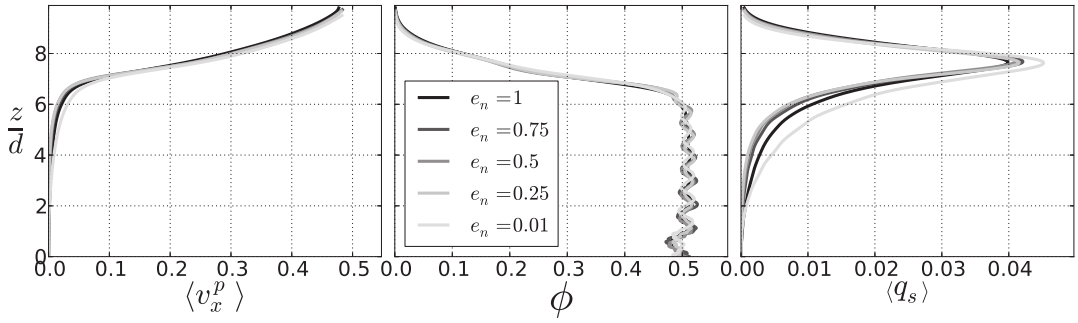

Figure 3.9: For case Sim20, the figure shows the sensitivity of the results to the restitution coefficient, comparing the reference case $e_n = 0.5$ with cases corresponding to restitution coefficient of $e_n = 0.01$, 0.25, 0.75, and 1. The highest the restitution coefficient, the darkest the associated line.

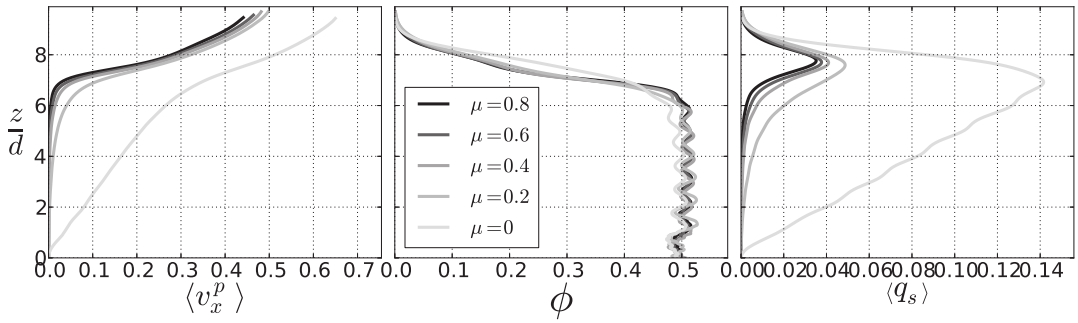

Figure 3.10: For case Sim20, the figure shows the sensitivity of the results to the friction coefficient, comparing the reference case $\mu^p = 0.4$ with cases corresponding to friction coefficient of $\mu^p = 0$, 0.2, 0.6, and 0.8. The highest the friction coefficient, the darkest the associated line.

Table 3.6: Results of the sensitivity analysis over the case Sim20. The reference case corresponds exactly to the case Sim20 described in section 3.1.3, the e_n and μ^p series correspond respectively to the variation of the restitution and friction coefficient, and fluct. to a simulation without fluctuation model (DRW). The measured Shields number θ^*, transport rate $\dot{n}$ (in term of beads per second), and RMS deviation with respect to the case Ref. $\frac{\Delta Q_{rms}{}^i}{\langle Q^{ref} \rangle}$ (cf eq. 3.6), are given for each case.

Run	μ^p	e_n	DRW model	θ^*	$\dot{n}$ (b/s)	$\frac{\Delta Q_{rms}{}^i}{\langle Q^{ref} \rangle}$
Sim 20	0.4	0.5	yes	0.06	26.38	0
fluct.	0.4	0.5	no	0.06	25.38	0.08
$e_n = 1$	0.4	1	yes	0.06	30.65	0.23
$e_n = 0.75$	0.4	0.75	yes	0.06	27.94	0.09
$e_n = 0.25$	0.4	0.25	yes	0.06	25.92	0.08
$e_n = 0.01$	0.4	0.01	yes	0.06	36.20	0.62
$\mu^p = 0.8$	0.8	0.5	yes	0.06	17.49	0.54
$\mu^p = 0.6$	0.6	0.5	yes	0.06	21.29	0.30
$\mu^p = 0.2$	0.2	0.5	yes	0.06	43.44	0.98
$\mu^p = 0$	0	0.5	yes	0.06	226.03	9.84

obtained for the cases $\mu^p = 0$, 0.2,0.6 and 0.8. From these five cases, the frictionless case shows a very important difference while the four others are weakly impacted. The bed flows down to the fixed bottom for the frictionless particle case, as indicated by the solid velocity profile. Considering the other cases, the solid volume fraction profile is weakly affected while the solid velocity and consequently the transport rate density show an increase mainly localized in the lower part with decreasing friction coefficient. Focusing on the variation between the cases $\mu^p = 0.4$ and $\mu^p = 0.8$, weak variations are observed. For quantitative analysis, looking at the RMS deviation with respect to case Sim20 in table 3.6, it appears that the friction coefficient impacts more importantly the transport rate density profile than the restitution coefficient, even if it exhibits no important qualitative change in the solid depth profiles when taken in a realistic range.

3.1.4 Conclusion

The particle-scale experimental comparison performed on three different cases of ideal mountain stream bedload allowed us to show the ability of the model to reproduce the average behavior of the granular phase in bedload transport. The numerical reproduction of the experiment and the choice of the different numerical parameters has been justified through convergence analysis. The accuracy of the model to describe the granular phase has been evaluated, and the sensitivity to different physical parameters has been investigated. The fluid velocity fluctuations model has

been shown to be necessary in order to reproduce the cases closer to the threshold of motion while it does not affect importantly the results for the highest Shields number case. The hindrance correction in the drag force formulation impacts mainly the fluid velocity inside the granular bed, and only represents a secondary effect regarding the solid depth profiles. In addition, the results show that, when taken in realistic ranges, the restitution coefficient has a negligible effect on the results while the friction coefficient has a low impact.
All together these results show the robustness of the experimental comparison with respect to variation of the model parameters. Up to now the results have been interpreted from the numerical robustness point of view. It is however clear that these variations can be interpreted considering the physical meaning of the different parameters. In the next section, a more general three-dimensional framework configuration will be used to further analyze the classical macroscopic sediment transport rate curve as a function of the Shields number and the average depth profiles.

3.2 Three-dimensional analysis

The quasi-2D particle-scale experimental validation presented, creates a solid ground to generalize the model to three dimensions. The latter is the purpose of the present section. In order to define a general framework, the effects of the periodic cell size, the DEM bottom boundary condition, and the polydispersity are studied (section 3.2.1). Extending the analysis to Shields number from 0.02 to 0.7, the results are then compared with the classical sediment transport rate curve as a function of the Shields number, and analyzed in term of depth profiles (section 3.2.2).

3.2.1 Framework adaptations

To extend the generality and focus on bulk equilibrium properties, a 3D bi-periodic (streamwise and spanwise) cell is considered. Consequently, the fluid wall friction term is removed in the fluid resolution. Compared with the quasi-2D case, the fluid resolution period is kept to $\tau_f = 10^{-2}s$ as it is not expected to change from 2D to 3D, and has been shown to have a negligible influence on average equilibrium profiles (section 3.1.2). The solid packing fraction ϕ^{max}, is modified according to the value observed in the 3D case, i.e. $\phi^{max} = 0.61$. The particles normal stiffness is evaluated in the same way as in quasi-2D, using equation (3.1), based on the maximum granular pressure undergone by the particles. For each run, the DEM results are averaged over 100 seconds. A new convergence analysis has been repeated in 3D considering the variation of both streamwise and spanwise periodic cell length. In addition, the influence of the granular bottom boundary condition and of the introduction of a slight polydispersity are evaluated. The analysis are detailed below.

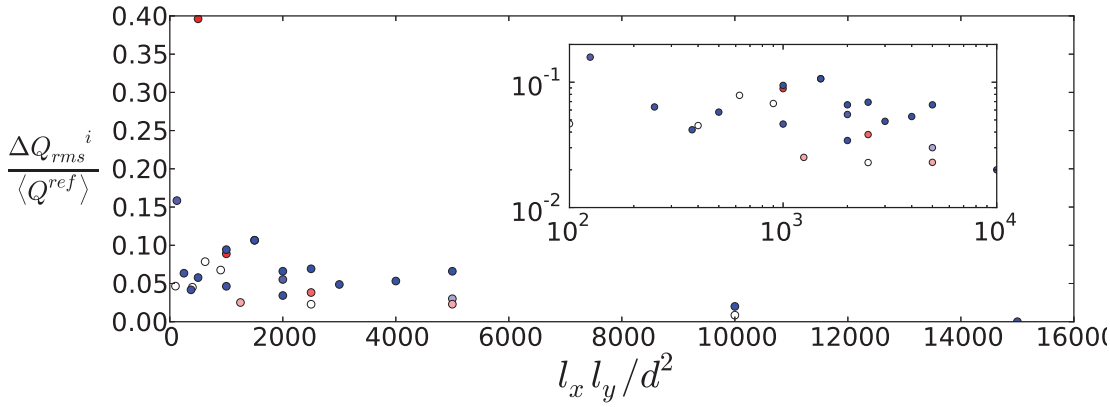

Figure 3.11: Convergence of the sediment transport rate profile as a function of the periodic cell size considered for the 3D case. The vertical axis represents the deviation with respect to the reference configuration $(l_x, l_y) = (50d, 30d)$ as defined in equation (3.6). The points color goes from red corresponding to $l_y >> l_x$ to blue corresponding to $l_x >> l_y$, passing by white for $l_x = l_y$.

Convergence analysis

Similarly to the 2D case, a convergence analysis has been undertaken. With respect to the former, the convergence in term of wall-normal weighting function length scale l_z is not expected to change. At higher Shields number, the convergence with decreasing l_z is even expected be better. Indeed, intense bedload is characterized by a smoother transition between the packed bed and the high velocity saltating particles. For simplicity l_z has been unchanged along the simulation, taken at its lower bound corresponding to the quasi-2D analysis: $l_z = d/30$. For the periodic cell size, a new convergence analysis has been performed considering the variation of both the streamwise and spanwise cell length at a Shields number around 0.1. As for the 2D case (section 3.1.2), the analysis is made on time-averaged sediment transport rate density profiles. The reference case has been chosen as $(l_x, l_y) = (500d, 30d)$, i.e. the relative cell size $V = l_x\, l_y\, l_z$ being bigger than the quasi-2D reference case ($15000d^2$ against $10000d^2$). A large number of simulations have been performed varying both l_x and l_y from $5d$ to $100d$. It has not been possible to consider smaller cell sizes, as the coupled fluid-particle model becomes unstable.

The results are summarized in figure 3.11, expressing the RMS deviation with respect to the reference case as a function of the product $l_x\, l_y/d^2$. The latter reflects the statistical representativity as it directly determines the size of the averaging cell $V = l_x\, l_y\, l_z$ (l_z fixed). Except for the red point corresponding to $(l_x, l_y) = (5d, 100d)$, all the results give a low RMS deviation and show a very slight decreasing trend with increasing cell size. This most probably reflects the fact that the results are already converged, and not anymore influenced by the periodic cell size. For confirmation it would be necessary to study smaller cell sizes, which is not possible

for numerical stability reasons. The unique point out of the cloud corresponds to $l_x = 5d$. The important variation is suspected to be due to a streamwise size lower than the characteristic length scale of the bedload phenomenon. This would prevent the phenomenon to develop regularly, and can be responsible for the fundamental differences observed. Not surprisingly, the spanwise direction takes less importance in the problem, and no difference are observed when reducing l_y down to $5d$. In addition, it appears that the cases with $l_x = l_y$ give better results than the other ones as the white points are all situated in the lower part of the cloud. As a consequence, a square-based cell will be adopted in the following.

The convergence seems to be faster with respect to the 2D case in term of full periodic cell size $V = l_x\ l_y\ l_z$. A cell size of $l_x = l_y = 10d$ is already converged, while the convergence is obtained with $l_x = 1000d$ and $l_y = 1d$ for the 2D case. It can be explained by the better randomness of the 3D packing, and suggests that the statistical representativity was not the limiting parameter in the quasi-2D convergence analysis. Indeed, the ordering of the packing as a function of the random bottom is important in this case and have probably been the limiting parameter. The choice of the 3D periodic cell have been made with respect to the present analysis, and considering the increasing numerical instability of the coupling with increasing Shields number. For the latter reason, a periodic cell of base $l_x = l_y = 30d$ has been adopted for all the simulations, except for the highest Shields number case ($\theta^* = 0.73$) that requires $l_x = l_y = 50d$.

DEM bottom boundary condition

To gain generality in the analysis, it is important for the results to be independent of the DEM bottom boundary condition. Following this idea, the influence of the fixed bottom and the number of granular layers have been tested. Performing trial and error tests, it has been observed that a fixed bottom generated from a gravity deposition is the most efficient. From a random generation of particles in space, a deposition is performed on a bottom flat wall in a bi-periodic cell, creating a particle bed of height $20d$. The particles with the center contained between elevation 9.5d and 10.5d are fixed, while the other ones are deleted. This creates a random bottom boundary condition with the properties of a granular packing. It allows to minimize the influence of the bottom on the granular sample.
To test the efficiency of the generated bottom and determine the required number of layers, further analysis are performed. Simulations are considered using the above described parameters and a bi-periodic cell of $l_x = l_y = 30d$ at a Shields number $\theta^* \sim 0.1$. First, the solid depth profiles are compared with simulations made with a flat wall boundary condition with different friction coefficient ($\mu_w = 0.4$ and $\mu_w = 0.2$). Figure 3.12 presents the averaged solid depth profiles for the three cases with similar Shields number. Above $z > 4.5d$, the shape is exactly the same in the three cases, and the profiles compare quantitatively. However, in the bed the insets show

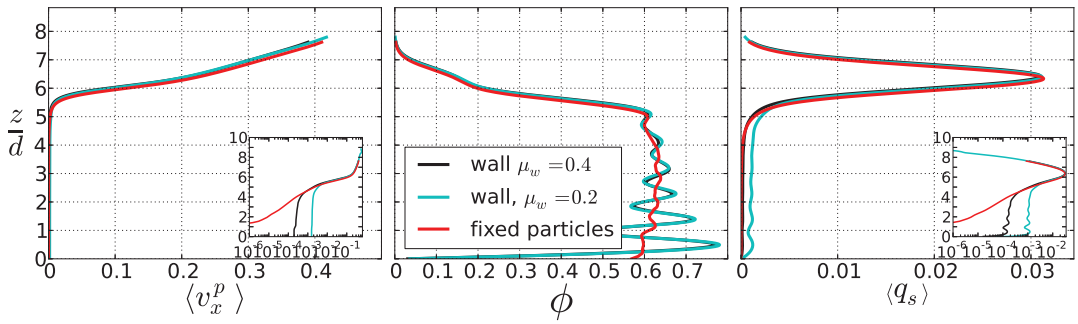

Figure 3.12: Effect of the nature of the DEM bottom boundary condition on the solid depth profiles at Shields number $\theta^* \sim 0.1$. Three types of bottom are considered: flat walls of friction coefficient $\mu_w = 0.2$ and $\mu_w = 0.4$, and random fixed particles obtained from a gravity deposition.

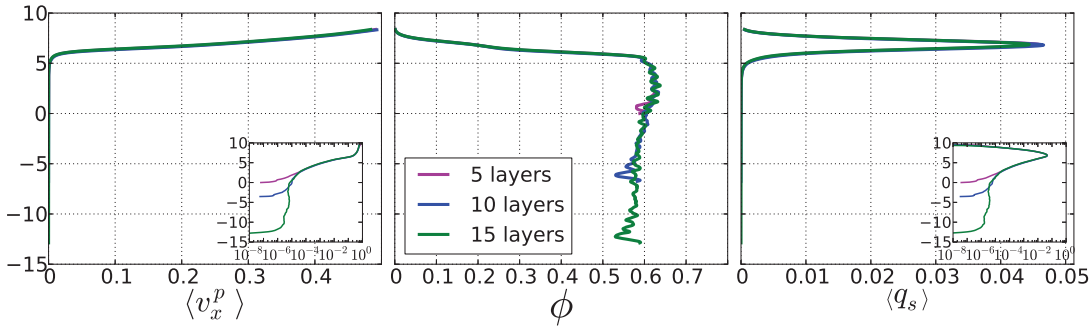

Figure 3.13: Effect of the number of particle layers on the solid depth profiles at Shields number $\theta^* \sim 0.1$.

that there is an important difference in the solid velocity profile, which is reflected in the transport rate density profile. In the case with the bottom made of fixed particles, an exponential decrease is observed, until a plateau when approaching the bottom boundary. For the case with walls, there is a clear difference for $z < 4d$: the exponential decrease changes to an almost constant velocity down to the fixed flat bottom. The velocity in the bed depends on the wall friction coefficient, suggesting a sliding-block behavior at the bottom of the sample. In addition, it is important to note that the nature of the bottom boundary condition is not affecting the profiles in the upper part, providing that the number of layers is sufficiently large.

To evaluate the minimum number of bead layers, three different simulations have been performed at a Shields number around 0.1, with respectively 5, 10, and 15 grain layers. Figure 3.13 shows the depth profiles of the three cases, in which the 0 has been shifted in order to match the fluid free-surface positions of the three different cases. The case with 5 layers of grains has been taken as reference, so that the wall-normal scale can be negative when considering a higher number of particle layers. On the figure, in the region of interest the profiles are superimposed, and do not

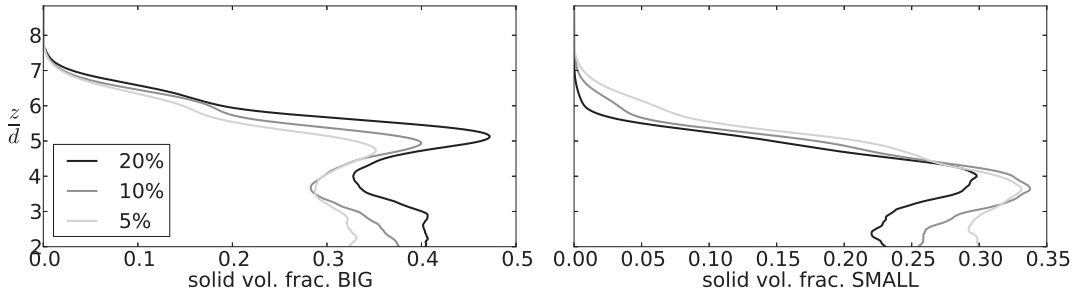

Figure 3.14: Effect of the polydispersity on the solid volume fraction profile of coarse ($d > d_{50}$) and fine ($d < d_{50}$) particles at Shields number $\theta^* \sim 0.1$, after 120s of simulation. The repartition of the profiles show that there is size-segregation for all three cases with increasing polydispersity.

show any influence of the number of layers. The only noticeable change stands in the bed (cf. insets) for the solid velocity and transport rate. The transport rate is the direct consequence of the solid velocity in this region so that only the velocity profile will be analyzed. For cases 5 and 10 layers, the curve goes away from the 15 layers one at about 2-3 diameters above the bottom fixed boundary condition. Above this limit the curves have exactly the same shape which means that there is no influence from the bottom anymore. Focusing on case 15 layers, the trend in the bed is clearly changing around $z = 0$, where the exponent of the decreasing exponential gets more important. The curves is very steep, and it is not clear if it is constant or if it is an exponential decrease. Similarly, above this point, we might wonder if a decreasing exponential is really present or not, as the linear part is limited. It can also be noted that the solid volume fraction is reducing when going down into the dense bed. This is a direct consequence of the very low velocity in this part, that did not allow the granular medium to move and compact itself during the simulated time. It is therefore not very relevant to analyze the behavior of this zone which can be considered as not yet at equilibrium.

The influence of the granular bottom boundary condition is restricted to its vicinity and does not impact the upper part of the flow. As such, bedload can be considered as a surface process, and the number of beads layer can be limited to its minimum in order to gain computational time. The results are independent from the fixed bottom and it will be taken in the following as random fixed particles.

Grain size distribution

In granular media modelling, a slight polydispersity is usually introduced in order to break particle regular arrangement (e.g. *Da Cruz et al.* (2005); *Duran et al.* (2012); *Izard et al.* (2014)). The polydispersity introduced is typically between ±5% and ±20% around the mean diameter. Size-segregation phenomena are usually avoided

by the continuous character of the grain size distribution. It is however important to ensure the absence of segregation, as it leads to out of equilibrium situations. To clarify this point, the influence of the polydispersity is tested considering samples with ±5%, ±10%, and ±20% of grain-size polydispersity around the mean diameter (d_{50}). Figure 3.14 shows the solid volume fraction profiles of the coarser ($d > d_{50}$) and finer ($d < d_{50}$) particles at Shields number $\theta^* \sim 0.1$, after 120s of simulation. It can be seen that the coarse particle volume fraction presents a peak at the top of the granular layer, while the fine one shows a peak at a position slightly below the coarse one. This is the characteristic signature of size-segregation where the fine particles sink into the bed, while the largest one rise to the bed surface. The direct consequence is that the granular flow in the region of interest, at the top of the layer, is only made of coarse particles and the transport rate is lowered. Accordingly, the particle diameter of interest becomes the largest particle diameter and the polydispersity may introduce bias. With a random fixed bottom breaking clusterization, no signature of important regular arrangement has been observed with monodisperse samples of maximum 10 bead layers. In consequence, and to avoid size-segregation, it has been decided to use strict monodisperse samples in the following.

3.2.2 Results

Keeping the parameters used for the quasi-2D analysis (see table 3.3), with a monodisperse bi-periodic configuration, simulations are performed in 3D with 10 granular layers, varying the water free-surface position to sample Shields number from 0.02 to 0.7.

Macroscopic considerations

To analyze macroscopically the problem, let us consider the dimensionless sediment transport rate $Q_s^* = Q_s/(\sqrt{(\rho^p/\rho^f - 1)gd^3})$ as a function of the Shields number θ^* (figure 3.15). The model results are compared with experimental data from *Meyer-Peter and Müller* (1948) (+), and *Wilson* (1966) (x). Simulation parameters for the reference configuration, represented as black squares (■), are the same as the one used for the experimental comparison (see table 3.3). The 3/2 power law is recovered by the numerical simulations and the results show a good agreement with experimental data for Shields number $\theta > 0.1$. Near the threshold of motion, the model results differ from experimental measurements. The linear inset shows that the transition around the critical Shields number, characteristic of the onset of motion, is sharper in the numerical simulation results than in the experimental measurements. Also, the critical Shields number is slightly lower: around 0.04 in the model, against 0.047 for *Meyer-Peter and Müller* (1948) data. This underestimation is consistent with the use of spheres in the numerical simulations, which present less important imbrications, and consequently smaller resistance to entrainment than

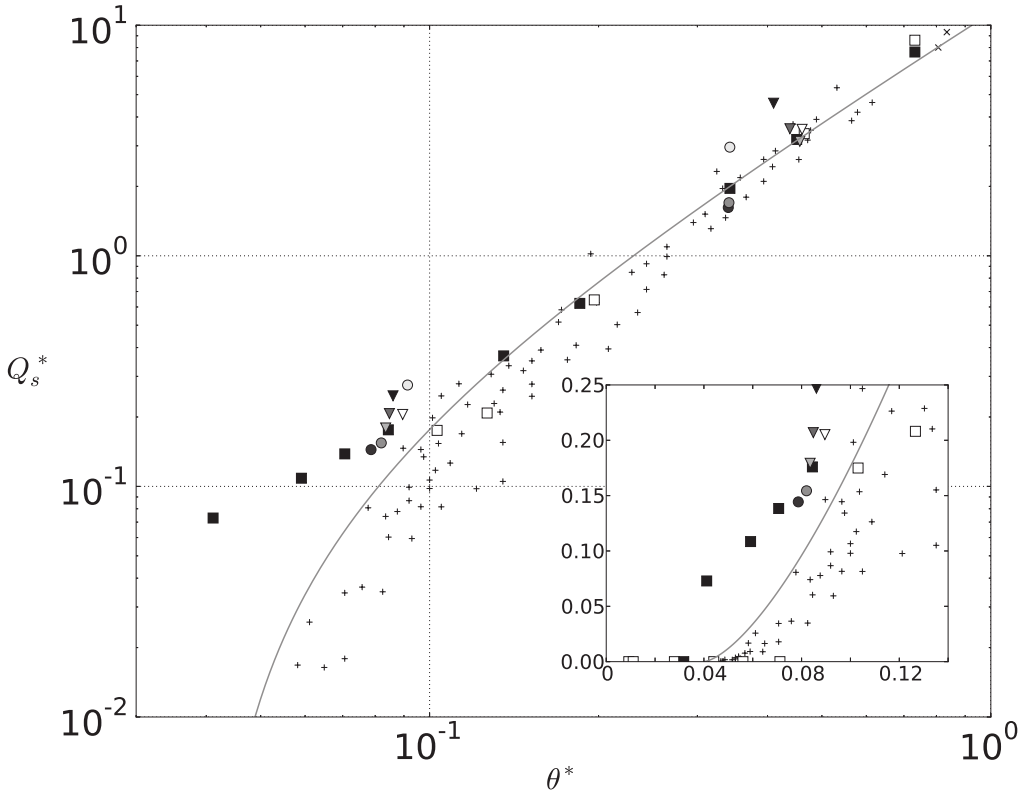

Figure 3.15: Dimensionless sediment transport rate Q_s^* as a function of Shields number θ^* for different configuration. Classical runs (■) with $e_n = 0.5$ and $\mu^p = 0.4$ are shown together with the exact same runs without turbulent fluctuation model (□) for different Shields number. Triangle symbols represent the change in restitution coefficient with $e_n = 0.01$ (▽), $e_n = 0.25$ (▼), $e_n = 0.75$ (▼), $e_n = 1$ (▼). Variations of the particle friction coefficient are represented by bullet points: $\mu^p = 0.2$ (•),$\mu^p = 0.6$ (•),$\mu^p = 0.8$ (•). The experimental data of *Meyer-Peter and Müller* (1948) (+) and *Wilson* (1966) (x) synthesized in *Yalin* (1977), show the experimental trend in power law 3/2, with the dispersion of the data. The gray line corresponds to $Q_s^* = 11.8(\theta^* - \theta_c^*)^{3/2}$ as found asymptotically by *Wilson* (1987). The inset in linear scale shows the behavior near the threshold of motion.

the natural sediment used in the experiments. Note also that the scatter of the experimental data is usually very important close to the threshold of motion due to different definitions of the onset of motion and difficulties in shear stress measurements (*Buffington and Montgomery*, 1997). In particular, the present choice of Shields number based on the maximum turbulent shear stress, is less arbitrary than classical momentum balance estimates based on the water depth measurement, but most probably leads to a slight underestimation. Considering the whole range of

Shields number investigated, the results are in good agreement with literature data, and this shows that the numerical model is able to reproduce quantitatively the sediment transport rate, except near the threshold of motion.

The results of the model without the fluid velocity fluctuations are shown in figure 3.15 as empty squares (□). At high Shields number negligible differences are observed, while the influence is important close to the threshold of motion. It is consistent with the present conditions, where the suspension number is relatively high ($w_s/u_* \in [1.7; 10]$) and the fluid velocity fluctuations are expected to mostly play a role close to the threshold of motion. Focusing on the linear plot, it is observed that the critical Shields number is changed from around 0.04 to around 0.09 in the case without fluid velocity fluctuations. The former is in the range of observed values under turbulent flow conditions (*Buffington and Montgomery*, 1997), while the latter is close to the value observed under laminar flow conditions (*Ouriemi et al.*, 2007). The influence of the fluctuations on the critical Shields number can be associated with turbulent coherent structures (e.g. *Papanicolaou et al.* (2002); *Dwivedi et al.* (2012)). However, the present simple fluid velocity fluctuations model does not account for the space-time correlations induced by turbulent boundary layer coherent structures. This partly explains that the fluctuations model does not allow to describe well the evolution of the sediment transport rate with Shields number close to the threshold of motion (figure 3.15). Nevertheless it permits to successfully reproduce the onset of sediment transport motion in the turbulent regime, resulting in a good comparison with experimental depth profiles (section 3.1.3).

The influence of the restitution coefficient is shown in figure 3.15 for two different Shields numbers, by keeping the free-surface position and number of particle layers constant. The restitution coefficient has been varied in the range $e_n \in [0.01, 1]$. It corresponds to a realistic range $e_n \in [0.25, 0.75]$, complemented by two extreme cases: no rebounds ($e_n = 0.01$) and no dissipation at contact ($e_n = 1$). Focusing on the realistic range at high Shields number ($\theta \sim 0.45$), the effect on the sediment transport rate is negligible. A slight trend is observed, the sediment transport rate and the Shields number being respectively increasing and decreasing function of the restitution coefficient. The extreme case without dissipation at contact ($e_n = 1$) follows the same trend but exhibits a more important transport rate increase. Quite surprisingly, the case $e_n = 0.01$ shows an increase in transport rate with respect to case $e_n = 0.25$. For the lower Shields number value ($\theta \sim 0.1$), while the dependency in restitution coefficient is limited in the realistic range, there is no associated clear trend. The non-monotonous dependencies observed show non-trivial coupling between the granular phase characteristics and the sediment transport rate. The global weak dependency on the restitution coefficient is consistent with results obtained by *Drake and Calantoni* (2001) under oscillatory flow conditions, and show that there is no need to include a lubrication model in the present condition. However, the relatively low importance of the restitution coefficient at such a high Shields

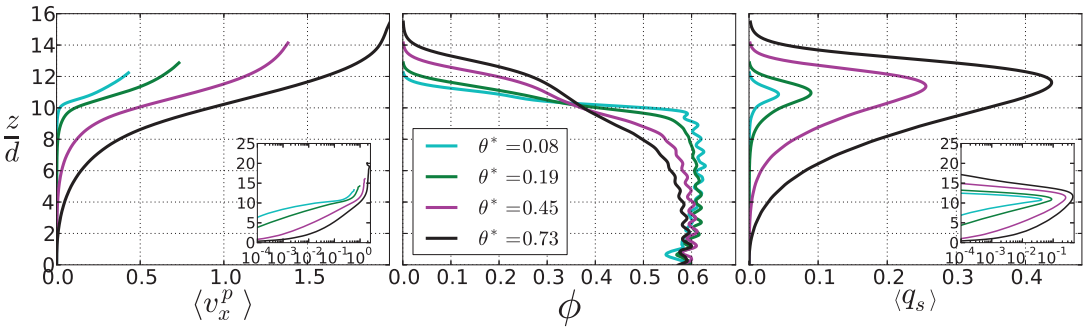

Figure 3.16: Evolution of the solid depth profiles with increasing Shields number. The simulations corresponds to different water free-surface elevation which goes from $13d$ up to $25d$, with a constant number of bead layers ($N_l = 10$).

number value is surprising. It is usually thought that collisional interactions are the dominant mechanism of momentum diffusion for such inertial particles (*Jenkins and Hanes*, 1998; *Armanini et al.*, 2005).

The effect of the particle friction coefficient is also shown in figure 3.15, represented by circles: $\mu^p = 0.2$ (●), $\mu^p = 0.6$ (●), $\mu^p = 0.8$ (●). Unlike the restitution coefficient analysis, the trend observed is monotonous for all values, and similar at low ($\theta \sim 0.09$) and high Shields number ($\theta \sim 0.35$). The sediment transport rate and the Shields number decrease with increasing friction coefficient. The effect appears to be non-linear as the observed influence for a variation from $\mu^p = 0.2$ to 0.4 is much greater than the one observed for a variation from $\mu^p = 0.4$ and 0.8. This type of dependency is characteristic of dry dense granular flows (*Da Cruz et al.*, 2005).

As a partial conclusion, the present analysis shows that (i) the 3/2 power law for the sediment transport versus Shields number relationship is well captured by the proposed model; (ii) the fluid velocity fluctuations model is essential to capture a realistic value for the critical Shields number under turbulent flow conditions (iii) the influence of the granular interaction parameters is low, when taken in a realistic range. These results underline the robustness of the model and strengthen the experimental validation. Extreme values of particle friction and restitution coefficient affect the results, and show complex behaviors. In order to understand better the mechanisms at work, the sensitivity to granular interaction parameters will be further discussed by analyzing the results in terms of depth profiles.

Depth profiles analysis

Figure 3.16 presents three depth profiles corresponding to Shields number from near-threshold to intense bedload transport. The solid transport rate density has

a typical shape with a more and more asymetric peak when the Shields number increases. Above and below the peak, an exponential shape is observed respectively increasing and decreasing. This trends are due to a solid velocity exponential increase in the bed, associated with a constant solid volume fraction. The highest Shields number case seems to be influenced by the bottom, suggesting that there might be an unsufficient number of particle layers for this case. An inflexion point in the solid velocity is observed near the transport rate peak elevation, and corresponds to a modification in the decreasing trend in the solid volume fraction profile, which can be assimilated as a shoulder. In the uppermost part, the concentration shows an important decrease, while the solid velocity is driven by the fluid. As already discussed, no experimental data are available for 3D bedload transport with spherical beads. However, *Revil-Baudard et al.* (2015) performed sheet flows experiments with plastic facets of equivalent diameter $3mm$ at Shields number $\theta^* \sim 0.45$. While the suspension number in their configuration is low and leads to important suspended load, it is interesting to compare the solid profiles. Similarly to what is observed, the velocity profiles show an exponential increase in the bed, followed by an inflexion point assimilated to a linear zone in their analysis. The associated solid volume fraction however does not exhibit the shoulder observed. This feature, observed in Euler-Euler numerical simulations with both granular description from the kinetic theory (*Hsu et al.*, 2004) and the $\mu^p(I)$ rheology (*Revil-Baudard and Chauchat*, 2013), was also present in the experimental results of *Capart and Fraccarollo* (2011) on sheet flows at similar Shields number. Video acquisition at the wall with plastic cylindrical particles of $6mm$ diameter, enabled *Capart and Fraccarollo* (2011) to obtain velocity and solid volume fraction profiles. The latter shows a shoulder for Shields number up to 1, while it seems to disappear at higher transport stage. This suggests that the presence of the concentration shoulder is linked to the suspension number. However, the measurements of *Revil-Baudard et al.* (2015) have been done at suspension numbers of approximately $s^* \sim 1.1$, while the transition in *Capart and Fraccarollo* (2011) is observed at $s^* \sim 0.7$. The question remains open, and could also be linked to the shape of the particles used. In their analysis, *Capart and Fraccarollo* (2011) consider a linear solid volume fraction and velocity profiles in the middle part. Results observed here suggest that this is not the case for spherical glass beads without suspension. In addition, the concentration profile is here observed to present a fixed point located at the base of the shoulder around which the different profiles adapt themselves. The size of the mobile layer is characterized by the extent for which the solid volume fraction is greater than zero and lower than 0.6. It is observed to increase with increasing Shields number, from about 2 to $10d$. Lastly, it is worth noting that the exponential increase of the solid velocity in the bed is characteristic of dry granular flows over an erodible bed (*Midi*, 2004; *Komatsu et al.*, 2001; *Richard et al.*, 2008).

The influence of the granular properties on the solid depth profiles is considered. Figure 3.17a shows the impact of the restitution coefficient for a Shields number

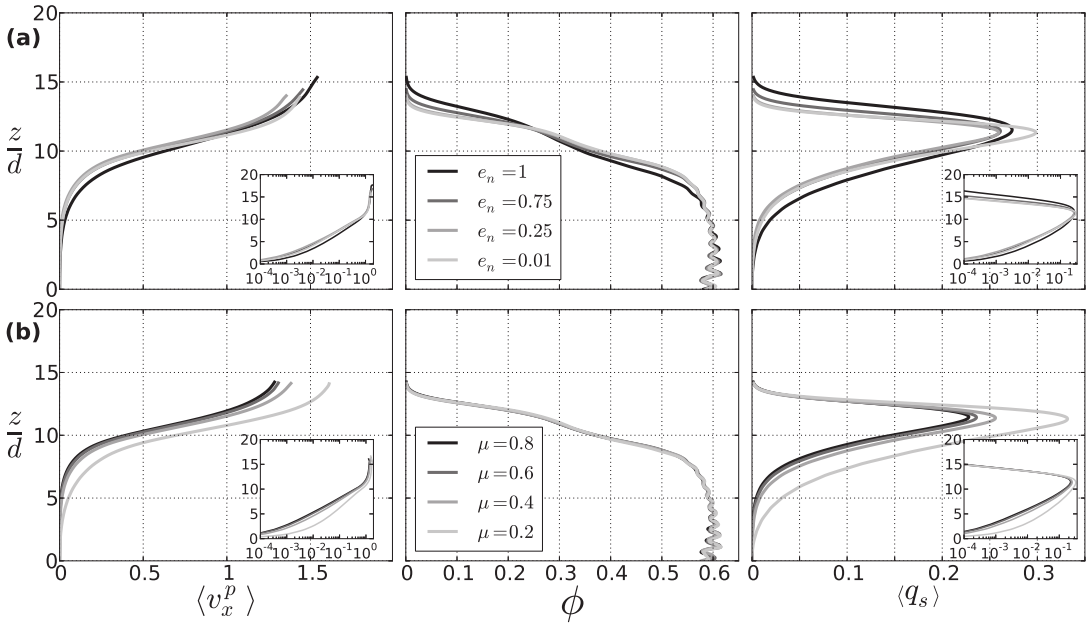

Figure 3.17: Effect of the restitution (a) and friction coefficient (b) on the average solid depth profiles for a Shields number $\theta \sim 0.45$. The solid velocity $\langle v_x^p \rangle$ and sediment transport rate density $\langle q_s \rangle$ are given in m/s, while the solid volume fraction ϕ is dimensionless. To give a global picture of the trend, the color of the lines are representative of the friction and restitution coefficient values. The position of the free surface in both case is situated at $20d$.

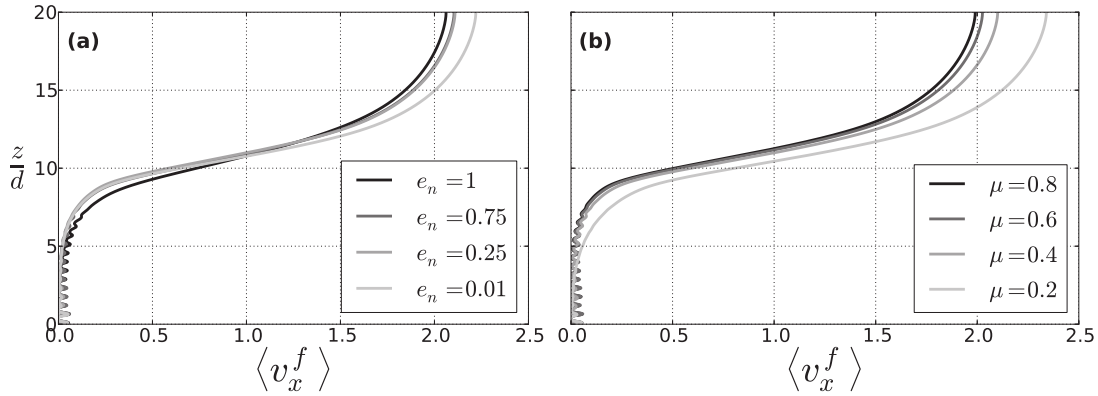

Figure 3.18: Effect of the restitution (a) and friction coefficient (b) on the average fluid velocity depth profiles for a Shields number $\theta \sim 0.45$. The lines get darker with increasing coefficient values.

$\theta \sim 0.45$. Such a high Shields number is expected to enhance the collisional effects. A clear trend appears on the transport rate density and the solid volume fraction. The width of the transport rate peak is increasing with increasing restitution coefficient. It is associated with a smoother transition of the volume fraction at the granular free-surface. Regarding the solid velocity, it is an increasing function of the restitution coefficient inside the bed. In the upper part, while the cases $e_n = 0.25$, $e_n = 0.75$, and $e_n = 1$ follow the same trend than in the bed, the lower restitution coefficient exhibits a higher solid velocity than all the other cases. This is surprising as the velocity is expected to be reduced in the upper part, with increasing dissipation at contact.
To understand this result, it is necessary to consider the coupling between the granular and the fluid phase. Indeed, the trend observed in the solid volume fraction profiles, suggests a reduction of the mobile layer thickness. This influences directly the fluid velocity (see figure 3.18), which is observed to increase in the upper part with decreasing restitution coefficient. In this part of the flow, the solid velocity is driven by both the fluid velocity and the restitution coefficient. The latter influence the saltation height through the importance of the energy loss at collisions, while the former gives the scale of the solid velocity at the different elevation. A competition between these two effects is taking place when reducing the restitution coefficient: the saltation height and the fluid velocity are respectively influenced negatively and positively. For $e_n = 0.25$ and $e_n = 0.75$ runs, the increase in fluid velocity with respect to simulation $e_n = 1$, is not compensating the energy loss due to the reduction of the restitution coefficient. However, it is the case when going to restitution coefficient close to zero ($e_n = 0.01$). These results show the complex coupling mechanisms between the granular and the fluid phase, and the non-trivial impact of the restitution coefficient on the depth structure of the granular flow.

Figure 3.17b shows the influence at high Shields number $\theta \sim 0.45$ of the friction coefficient over the range $\mu^p \in [0.2; 0.8]$ with 0.2 steps. Interestingly, the solid volume fraction profile is not affected by the variation in friction coefficient. On the contrary, the particle velocity and thus the sediment transport rate density profiles are increasing when the friction coefficient is decreased. The increase of the velocity throughout the depth is mainly affecting the lower part of the sediment transport rate density profile, where the solid volume fraction is maximum. It corresponds to the denser part of the granular flow, for which the frictional interactions are dominant. The fluid velocity profile (figure 3.18) follow the trend, and is a decreasing function of the friction coefficient. This is a direct consequence of the reduction of the bed resistance due to the decrease in friction coefficient.

This analysis shows that, while affecting weakly the macroscopical results, the friction and restitution coefficient impact the depth structure of the granular flow differently. In addition, the non-monotonous behaviors observed suggests the presence of non-trivial coupling between the solid and the fluid phases.

3.3 Conclusion

The model has been compared with experiments in two different configurations considering both the classical macroscopic sediment rate as a function of the Shields number, and the granular depth profiles. The ability of the model to reproduce these two important behaviors and the robustness of the comparisons with respect to the parameters, show the relevance of the model which reproduces not only the evolution of the sediment transport rate as a function of the Shields number, but also the depth structure of the granular phase. The rigorous approach developed to tackle granular bulk behavior in bedload transport, gives a solid basis for further use of the model and enhances the generality of the results presented here. The influence of the different model contributions have been studied. In particular, the discrete random walk fluid velocity fluctuations model has been shown to be sufficient to reproduce the reduction of the critical Shields number due to turbulent fluctuations. A weak impact of the restitution and friction coefficients variations has been observed on the macroscopic sediment transport rate versus Shields number. In addition, the study of the granular depth profiles allowed us to make the paralell with dry granular flows, and better understand the mechanisms at work in bedload transport. In particular, it has been shown that the granular parameters influence the depth structure of the granular flow, and induce non-trivial coupling with the fluid phase.

The rigorous development of the model and the experimental validations demonstrate the potential of this approach to deal with granular processes in bedload transport. It will be used in the next chapter to study the effect of the slope and specific density in bedload transport.

Chapter 4

Slope and specific density effects

The present chapter deals with the variation of the sediment transport rate due to change in slope, specific density and particle diameter, which are the main parameters of the problem. The aim is to characterize bedload transport from a dimensionless point of view, and to understand the origin of the different contributions.

Before presenting the results, it is interesting to consider the expected dependency from dimensional analysis. As evidenced in the previous chapter, bedload transport is a complex phenomenon with important coupling between the fluid and the granular phase. Some simple dimensional analysis can still bring ideas about the driving mechanisms. As a matter of fact, the scale of the force in the problem is given by the gravity for both fluid and solid phases. Considering the granular phase, the scale is given by the buoyant weight, so that the gravity appears only mutiplied by the specific density $(\rho^p/\rho^f - 1)g$. As expressed by *Duran et al.* (2012), there exists two typical length scales for the granular medium in the problem: the particle diameter d and the hydrodynamic length scale associated with turbulent drag $\rho^p/\rho^f d$. Yet, in the present problem, the density ratio is not varying importantly, so that the latter might be less relevant. Taking into account the fluid density as a mass scale, it allows to normalize classically the fluid bed shear stress by forming the Shields number:

$$\theta^* = \frac{\tau_b}{(\rho^p - \rho^f)gd}, \tag{4.1}$$

and the dimensionless sediment rate:

$$Q_s^* = \frac{Q_s}{\sqrt{(\rho^p/\rho^f - 1)gd^3}}, \tag{4.2}$$

also called Einstein parameter. In addition to these two dimensionless parameters, the suspension number $S^* = w_s/u_*$ is also usually evaluated to characterize the importance of suspension (*Sumer et al.*, 1996). Considering hydraulic rough flow conditions ($Re_p >> 1$), it can be directly linked to the Shields number. Expressing the shear velocity from equation (4.1) with $\tau_b = \rho^f u_*^2$, the suspension number reads:

$$S^* = \frac{w_s}{u^*} = \frac{\sqrt{\frac{4}{3C_D}(\rho^p/\rho^f - 1)gd}}{\sqrt{\theta^*(\rho^p/\rho^f - 1)gd)}} = \sqrt{\frac{4}{3C_D\theta^*}}. \tag{4.3}$$

Therefore, for spherical beads, it is fully determined by the Shields number. Accordingly, it is not a relevant parameter, and the relatively low Shields number ensures no effect of the suspension. Also, the Stokes number $St = \rho^p v^p d/(9\eta^f)$, comparing the inertia of the particle to the fluid viscosity effect, is not affecting importantly the collisions as it is always greater than 10^3 in the conditions considered (*Gondret et al.*, 2002).

Therefore, in agreement with the literature on the subject, the Einstein parameter and the Shields number seem to be the main dimensionless numbers representative of turbulent bedload transport. These two dimensionless numbers take into account the effect of the slope, mainly through the impact on the fluid bed shear stress. Indeed, the latter is very sensitive to the inclination angle. This is well understood when considering the classical force balance approximation $\tau_b = \rho^f g \sin\alpha \; w_d$, with w_d the water depth. At first order, the sine function is linear, impacting importantly the contribution. The geometrical effect of the slope inclination angle on the granular material can be taken into account through the gravity term by replacing the acceleration of gravity g by its projection along the wall-normal axis $g\cos\alpha$. In addition, it is also classically taken into account by modifying the critical Shields number θ_c (*Fredsøe and Deigaard*, 1992):

$$\theta_c^* = (\theta_c^*)_0 \cos\alpha \left[1 - \frac{\tan\alpha}{\mu_s}\right], \tag{4.4}$$

where $(\theta_c^*)_0$ is the critical Shields number at negligible slope angle, and μ_s is the static effective friction coefficient of the granular material. Therefore, the effect of the slope is restricted to the surface contribution of the fluid, and the geometrical effect on the granular phase.

In this chapter, it is shown that the effect of the slope is much more complex and also dependent on the specific density. It allows to draw a more general picture of bedload transport. The chapter is structured as follows: the effect of the slope and the specific density are quantified in terms of sediment transport rate as a function of Shields number, as well as solid depth profiles (section 4.1). Through analytical development of the average continuous two-phase equation, the problem is exposed in terms of shear to normal granular stress ratio, and the different components are analyzed (section 4.2). It is shown that the granular medium undergoes a transition to what can be assimilated as a debris flow (section 4.3.1). Lastly, a rescaled Shields number taking into account the slope and the specific density effect is proposed, and is shown to make the data collaspe on a single curve (section 4.3.2).

4.1 Results

The slope, the specific density and the Shields number are varied systematically, and average solid depth profiles are measured together with the dimensionless sediment transport rate. The slopes varies between 0.05 (2.9°) and 0.27 (15.1°). The specific density $\rho^p/\rho^f - 1$ takes two extreme values around the realistic 1.5 ($\rho^p = 2500kg/m^3$): 0.75 ($\rho^p = 1750kg/m^3$) and 3 ($\rho^p = 4000kg/m^3$). The Shields number sampled vary in the range $\theta^* \in [0.03 - 0.1]$, from incipient motion to moderate bedload transport. Table 4.1 summarizes all the data.

4.1.1 Sediment transport rate

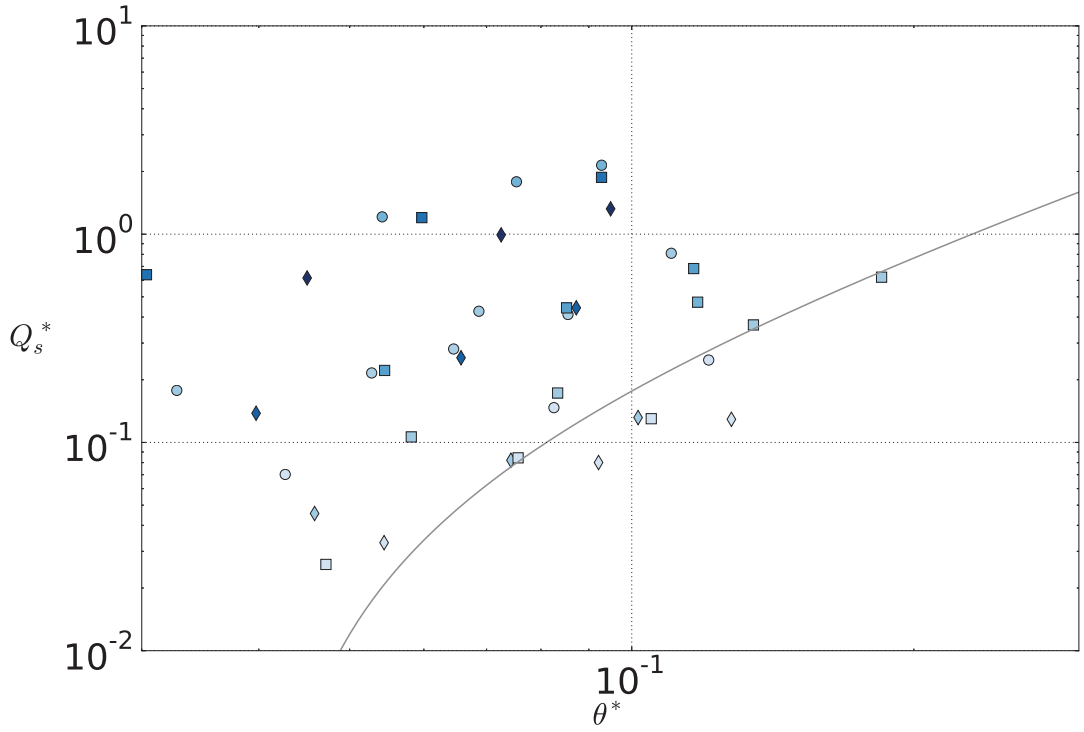

Figure 4.1: Sediment transport rate as a function of the Shields number for variation of specific density and slope. The intensity of the color reflects the value of the slope angle, while the symbol are representative of the specific density (see table 4.1 for exact correspondence of the symbols). The gray line corresponds to the trend observed for the slope 0.1 in the previous chapter: $Q_s^* = 11.8(\theta^* - \theta_c^*)^{3/2}$.

Figure 4.1 shows the sediment transport rate as a function of the Shields number. The intensity of the color reflects the magnitude of the slope, and the symbol are representative of the specific density. First, important variations are observed for given Shields number, in particular with strong deviation from the classical trend represented by the gray line. The increase of sediment transport at a given Shields

Table 4.1: Parameters of the simulations studied and symbol correspondence. The slope inclination angle α, specific density $\rho^p/\rho^f - 1$ and Shields number θ^* have been varied. The color intensity is associated with the value of the slope angle, and each specific density to a symbol.

Run	α	$\rho^p/\rho^f - 1$	θ^*	Q_s^*	symbol
r1sl05s1	0.05	0.75	0.043	0.07	
r1sl05s2	0.05	0.75	0.083	0.147	
r1sl05s3	0.05	0.75	0.121	0.249	
r2sl05s1	0.05	1.5	0.047	0.026	
r2sl05s2	**0.05**	**1.5**	**0.076**	**0.084**	
r2sl05s3	0.05	1.5	0.105	0.13	
r4sl05s1	0.05	3	0.054	0.033	
r4sl05s2	0.05	3	0.092	0.08	
r4sl05s3	0.05	3	0.128	0.129	
r1sl09s1	0.09	0.75	0.053	0.216	
r1sl09s2	0.09	0.75	0.065	0.281	
r1sl09s3	0.09	0.75	0.085	0.411	
r2sl1s1	0.1	1.5	0.032	0.0	
r2sl1s2	**0.1**	**1.5**	**0.058**	**0.106**	
r2sl1s3	**0.1**	**1.5**	**0.083**	**0.173**	
r2sl1s4	0.1	1.5	0.135	0.366	
r2sl1s5	0.1	1.5	0.185	0.622	
r1sl1s1	0.1	0.75	0.033	0.178	
r1sl1s2	0.1	0.75	0.069	0.426	
r1sl1s3	0.1	0.75	0.11	0.81	
r4sl1s1	0.1	3	0.046	0.046	
r4sl1s2	0.1	3	0.074	0.082	
r4sl1s3	0.1	3	0.102	0.132	
r1sl13s1	0.13	0.75	0.054	1.211	
r1sl13s2	0.13	0.75	0.075	1.785	
r1sl13s3	0.13	0.75	0.093	2.143	
r2sl13	0.13	1.5	0.118	0.472	
r2sl15s1	0.15	1.5	0.054	0.222	
r2sl15s2	0.15	1.5	0.085	0.443	
r2sl15s3	0.15	1.5	0.116	0.683	
r2sl2s1	0.2	1.5	0.03	0.639	
r2sl2s2	**0.2**	**1.5**	**0.06**	**1.2**	
r2sl2s3	0.2	1.5	0.093	1.874	
r4sl22s1	0.22	3	0.04	0.138	
r4sl22s2	0.22	3	0.066	0.255	
r4sl22s3	0.22	3	0.087	0.443	
r4sl27s1	0.27	3	0.045	0.616	
r4sl27s2	0.27	3	0.073	0.992	
r4sl27s3	0.27	3	0.095	1.323	

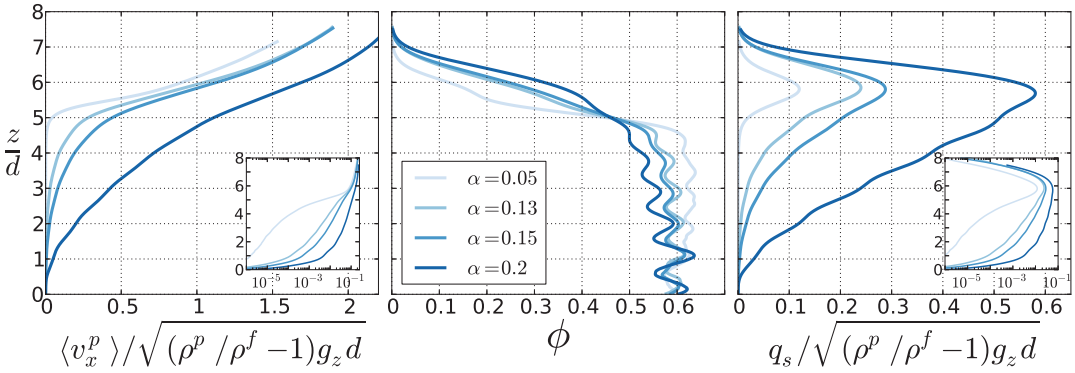

Figure 4.2: Effect of the slope inclination on the normalized solid velocity, volume fraction, and transport rate density profiles, for a given specific density $\rho^p/\rho^f - 1 = 1.5$ and a Shields number $\theta^* \sim 0.11$. The data correspond to cases r2sl05s3, r2sl13, r2sl15s3, and r2sl2s3 in table 4.1.

numbers goes together with colors getting darker, meaning that the slope influences the phenomenon. The highest the slope is, the highest the transport rate. Looking more carefully, this trend holds only for a given specific density. Lower specific density cases lead to a higher sediment rate for a given slope. As can be seen from table 4.1 recalling the data, the increase of sediment rate at given Shields number and specific density is a non-linear function of the slope. Considering for example a specific density of 1.5, doubling the slope from 0.05 (r2sl05s2) to 0.1 (r2sl1s3) leads to an increase of 50% in transport rate, while doubling from 0.1 (r2sl1s2) to 0.2 (r2sl1s2) multiply the transport rate by 10 (+900%) for the same Shields number (cases in bold in table 4.1). Similar behaviors can be observed for the other specific density when varying the slope.

4.1.2 Solid depth profiles

The effect of respectively the slope and the specific density are considered independently, studying the solid depth profiles.

Slope effect

Figure 4.2 shows the effect of the slope on the solid depth profiles for given specific density and Shields number. Following the classical scaling adopted in the introduction, the solid velocity and transport rate density profiles are normalized by $\sqrt{(\rho^p/\rho^f - 1) g_z d}$, with $g_z = g \cos\alpha$. At constant specific density and Shields number, the effect of the slope is supposed to be only contained in g_z. Considering the solid velocity, the uppermost shape of the depth profile is not influenced importantly, except for the highest slope. In the bed, the solid velocity is an increasing function of the slope, smoothing out the transition from the granular bed to the

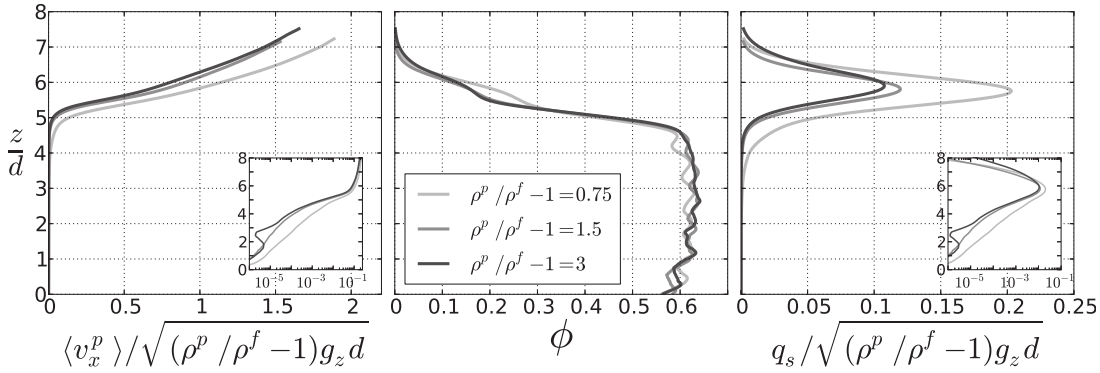

Figure 4.3: Effect of the specific density variation on the normalized solid velocity, volume fraction, and transport rate density profiles, at a given slope angle of $\alpha = 0.05$. Cases r1sl05s3, r2sl05s3, r4sl05s3 in table 4.1.

interface with the fluid. Similarly, the sharpness of the solid volume fraction at the granular free-surface is reduced with increasing slope. The lower granular layers are more and more mobilized, as can be seen from the reduction of the solid volume fraction in the bed . Therefore, the transport rate profile shape evolves, showing a more important asymmetry toward the bed, with increasing slope angle. The profiles show a gradual evolution with the slope for the lowest value ($\alpha = 0.05, 0.13, 0.15$), whereas a sharp transition is observed from $\alpha = 0.15$ to $\alpha = 0.2$. For the latter case, the values of the velocity, solid volume fraction, and transport rate density indicate that it is flowing over the entire granular layer. Altogether, these results show that the slope affects very importantly the structure of the granular flow and the intensity of the transport rate density. The variation of the profiles normalized by the classical scaling, show that the latter is not able to account for the effect of the slope observed.

Specific density effect

Figure 4.3 shows the variation of the solid depth profiles with the specific density, considering fixed slope and Shields number. For the three profiles, the two highest specific density leads to very similar profiles when normalized by the scaling from classical bedload analysis. However, the lowest specific density presents important differences. The normalized solid velocity is higher than the two other cases, over the entire depth. In addition, the concentration shoulder observed at z/d between 5 and 6, is more important, reflecting a change in the structure of the granular flow. The consequence in term of normalized bedload transport is important, as shown by the value at the peak which doubles compared with the two other cases. These features suggest non-trivial mechanisms with variation of the specific density, which are not captured by the classical sediment transport scaling.

4.2 Analytical analysis of the granular depth structure

The effect of both the slope and the specific density are important in terms of sediment transport rate, and are not well described by the classical scaling in terms of Shields number and dimensionless sediment transport rate. To better understand the mechanisms at play, the two-phase continuous equations describing bedload transport are considered. With steady unidirectional assumptions, they read along the streamwise and wall-normal directions (chapter 2, eq. (2.9), and *Revil-Baudard and Chauchat* (2013)):

$$0 = \frac{\partial S_{xz}^f}{\partial z} + \frac{\partial R_{xz}^f}{\partial z} + \rho^f (1-\phi) g \sin\alpha - n \left\langle f_{f\,x}^p \right\rangle^p, \tag{4.5}$$

$$0 = \frac{\partial \tau_{xz}^p}{\partial z} + \rho^p \phi g \sin\alpha + n \left\langle f_{f\,x}^p \right\rangle^p, \tag{4.6}$$

$$0 = \frac{\partial P^f}{\partial z} + \rho^f (1-\phi) g \cos\alpha, \tag{4.7}$$

$$0 = \frac{\partial \tau_{zz}^p}{\partial z} + (\rho^p - \rho^f) \phi g \cos\alpha. \tag{4.8}$$

Focusing on the granular equations (eq. 4.6 and 4.8), both can be integrated between a position $z < h_p$ and h_p the top of the granular layer. At the latter position, the granular stress tensor is zero, and the integrated streamwise component of the momentum balance equation reads:

$$0 = -\tau_{xz}^p(z) + \rho^p g \sin\alpha \int_z^{h_p} \phi(\zeta) d\zeta + \int_z^{h_p} n \left\langle f_{f\,x}^p \right\rangle^p (\zeta) d\zeta, \tag{4.9}$$

so that:

$$\tau_{xz}^p(z) = \rho^p g \sin\alpha \int_z^{h_p} \phi(\zeta) d\zeta + \int_z^{h_p} n \left\langle f_{f\,x}^p \right\rangle^p (\zeta) d\zeta. \tag{4.10}$$

Similarly, the equation along the wall-normal direction can be modified into:

$$\tau_{zz}^p(z) = g \cos\alpha (\rho^p - \rho^f) \int_z^{h_p} \phi(\zeta) d\zeta. \tag{4.11}$$

For the fluid, only the streamwise equation (eq. 4.5) will be considered. Integrating between z and h_p, it reads:

$$0 = S_{xz}^f(h_p) - S_{xz}^f(z) + R_{xz}^f(h_p) - R_{xz}^f(z) + \rho^f g \sin\alpha \int_z^{h_p} [1-\phi(\zeta)] d\zeta - \int_z^{h_p} n \left\langle f_{f\,x}^p \right\rangle^p (\zeta) d\zeta. \tag{4.12}$$

Revil-Baudard and Chauchat (2013) showed that the effective viscous shear stress

tensor is negligible in sheet-flow simulations. It will be shown in chapter 5 section 5.1.2 that it stays negligible in the present case. In addition, the Reynolds stress tensor is fully damped in the quasi-static bed, so that $R^f_{xz}(z) = 0$. Therefore, the equation simplifies into:

$$0 = R^f_{xz}(h_p) + \rho^f g \sin\alpha \int_z^{h_p} [1-\phi(\zeta)]d\zeta - \int_z^{h_p} n \left\langle f^p_{f\,x} \right\rangle^p (\zeta) d\zeta. \tag{4.13}$$

Considering that h_p is close to the position of the maximum of turbulent shear stress, $R^f_{xz}(h_p)$ can be rewritten as the bed shear stress $\tau_b = \rho^f u_*^2$. Expressing the interaction term as a function of the rest, we end-up with:

$$\int_z^{h_p} n \left\langle f^p_{f\,x} \right\rangle^p (\zeta) d\zeta = \tau_b + \rho^f g \sin\alpha \int_z^{h_p} [1-\phi(\zeta)]d\zeta. \tag{4.14}$$

Combining equations (4.10), (4.11) and (4.14), the effects observed in section 4.1 can be understood in simple terms. The shear to normal stress ratio $\tau^p_{xz}(z)/\tau^p_{zz}(z)$ can be expressed from equations (4.10) and (4.11):

$$\begin{aligned}\frac{\tau^p_{xz}(z)}{\tau^p_{zz}(z)} &= \frac{\rho^p g \sin\alpha \int_z^{h_p} \phi(\zeta)d\zeta + \int_z^{h_p} n \left\langle f^p_{f\,x} \right\rangle^p (\zeta) d\zeta}{g\cos\alpha(\rho^p-\rho^f)\int_z^{h_p}\phi(\zeta)d\zeta} \\ &= \frac{\rho^p g \sin\alpha \int_z^{h_p} \phi(\zeta)d\zeta}{g\cos\alpha(\rho^p-\rho^f)\int_z^{h_p}\phi(\zeta)d\zeta} + \frac{\int_z^{h_p} n \left\langle f^p_{f\,x} \right\rangle^p (\zeta) d\zeta}{g\cos\alpha(\rho^p-\rho^f)\int_z^{h_p}\phi(\zeta)d\zeta}.\end{aligned} \tag{4.15}$$

Using equation (4.14), the last term on the right hand side can be rewritten, so that:

$$\frac{\tau^p_{xz}(z)}{\tau^p_{zz}(z)} = \frac{\rho^p g \sin\alpha \int_z^{h_p} \phi(\zeta)d\zeta}{g\cos\alpha(\rho^p-\rho^f)\int_z^{h_p}\phi(\zeta)d\zeta} + \frac{\tau_b + \rho^f g \sin\alpha \int_z^{h_p} [1-\phi(\zeta)]d\zeta}{g\cos\alpha(\rho^p-\rho^f)\int_z^{h_p}\phi(\zeta)d\zeta}. \tag{4.16}$$

which can be simplified into:

$$\frac{\tau^p_{xz}(z)}{\tau^p_{zz}(z)} = \frac{\rho^p}{\rho^p-\rho^f}\tan\alpha + \frac{\tau_b}{g\cos\alpha(\rho^p-\rho^f)\int_z^{h_p}\phi(\zeta)d\zeta} + \frac{\rho^f \tan\alpha \int_z^{h_p}[1-\phi(\zeta)]d\zeta}{(\rho^p-\rho^f)\int_z^{h_p}\phi(\zeta)d\zeta}. \tag{4.17}$$

For clarity, let us consider an average solid volume fraction $\bar{\phi}_z$ between z and h_p, defined as:

$$\bar{\phi}_z(h_p - z) = \int_z^{h_p} \phi(\zeta) d\zeta. \tag{4.18}$$

Equation (4.17) can finally be expressed as:

$$\frac{\tau_{xz}^p(z)}{\tau_{zz}^p(z)} = \frac{\rho^p}{\rho^p - \rho^f} \tan\alpha + \frac{\tau_b}{g\cos\alpha(\rho^p - \rho^f)\bar{\phi}_z(h_p - z)} + \frac{\rho^f}{\rho^p - \rho^f} \frac{1 - \bar{\phi}_z}{\bar{\phi}_z} \tan\alpha. \tag{4.19}$$

This equation shows that the granular phase shear to normal stress ratio is composed of three terms, which can be associated with different contributions. In dry granular flows over inclined planes, the effective friction coefficient is fully determined by the slope and reads $\tau_{xz}^p(z)/\tau_{zz}^p(z) = \tan\alpha$ at any position z (*Andreotti et al.*, 2013). For bedload transport, the equivalent contribution is the first term on the right hand side of equation (4.19). It is modified by the buoyancy, due to the hydrostatic property of the fluid flow. In addition, two other contributions are present. Identifying the Shields number, the second term on the right hand side can be rewritten as:

$$\frac{\tau_b}{g\cos\alpha(\rho^p - \rho^f)\bar{\phi}_z(h_p - z)} = \frac{\theta^*}{\bar{\phi}_z(h_p - z)/d} \tag{4.20}$$

It is a surface term due to the fluid bed shear stress. Therefore, its intensity decays inside the granular bed with decreasing elevation. Lastly, the third term on the right hand side of equation (4.19) compares the indirect slope effect on the granular phase due to the fluid-solid interaction[1] (see eqs. 4.13 and 4.16), to the buoyant weight contribution of the granular phase (see eq. 4.8 and 4.11). It does not depend on the depth as both are linear with wall-normal position z.

Considering the limit case for which the bed is at rest, and the surface contribution is negligible with respect to the other two (low Shields number), equation (4.19) reduces to:

$$\begin{aligned}\frac{\tau_{xz}^p(z)}{\tau_{zz}^p(z)} &= \frac{\rho^p}{\rho^p - \rho^f} \tan\alpha + \frac{\rho^f}{\rho^p - \rho^f} \frac{1 - \phi^{max}}{\phi^{max}} \tan\alpha \\ &= \frac{\tan\alpha}{\rho^p/\rho^f - 1} \left[\frac{\rho^p}{\rho^f} + \frac{1 - \phi^{max}}{\phi^{max}}\right].\end{aligned} \tag{4.21}$$

The configuration can be assimilated as a gravity-driven fluid flow inside a porous medium. Comparing the stress ratio formulation with the constant static effective

[1] The slope affects the fluid contribution, which in turn affects the granular phase through the drag force

friction coefficient of the granular material μ_s, the fluid flow effect can be seen as a reduction of the apparent friction coefficient. Therefore, the granular bed is more easily mobilized with increasing fluid contribution. The latter is an increasing function of the specific density and the slope angle, and might be at the origin of the effect observed on the sediment transport rate.

Manipulating equation (4.19), it is possible to quantify precisely the effects of slope and specific density. Following *Revil-Baudard and Chauchat* (2013), the case $z = h_c$ is considered, where h_c is defined such that: $\tau^p_{xz}(h_c)/\tau^p_{zz}(h_c) = \mu_s$. The thickness of the mobile layer $\delta_s = h_p - h_c$ can be expressed from equation (4.19):

$$\frac{\delta_s}{d} = \frac{\theta^*}{\bar{\phi}\left[\mu_s - \left(1 + [\bar{\phi}(\rho^p/\rho^f - 1)]^{-1}\right)\tan\alpha\right]}. \tag{4.22}$$

Not surprisingly, it depends on the Shields number, the specific density and the slope angle.

4.3 Discussion

4.3.1 Transition from bedload to debris flow

Increasing the slope of the channel, a transition to granular debris flow should be observed. In the present context, the term debris flow is employed to describe configurations for which the full granular layer is mobilized, independently of its size. It corresponds to the limit case for which δ_s/d tends to infinity, and should not depend on the Shields number. It is possible providing the denominator of the right hand side of equation (4.22) tends to zero. Therefore, the critical slope angle (α_0) corresponding to the transition to debris flow can be defined as:

$$\mu_s - \left(1 + [\bar{\phi}(\rho^p/\rho^f - 1)]^{-1}\right)\tan\alpha_0 = 0, \tag{4.23}$$

Considering an infinite layer in motion at the transition to debris flow, the average solid volume fraction $\bar{\phi}$ tends to the packing fraction ϕ^{max}. The critical slope angle can then be expressed as:

$$\tan\alpha_0 = \frac{\mu_s}{1 + [(\rho^p/\rho^f - 1)\phi^{max}]^{-1}}. \tag{4.24}$$

We recover here the critical slope angle for the transition to debris flow, as derived by *Takahashi* (1978) (see *Takahashi* (2007)). In the present case, the static effective friction coefficient and the maximum packing fraction are not varying. As a consequence, it depends only on the specific density and it can be predicted for the considered values: respectively $\alpha_0 = 0.12$, 0.19, and 0.25, for specific density $\rho^p/\rho^f - 1 = 0.75$, 1.5, and 3. As can be seen from table 4.1, these critical inclina-

tion angles have been exceeded in the simulations performed, and correspond to the sharp increase observed in the dimensionless sediment rate.

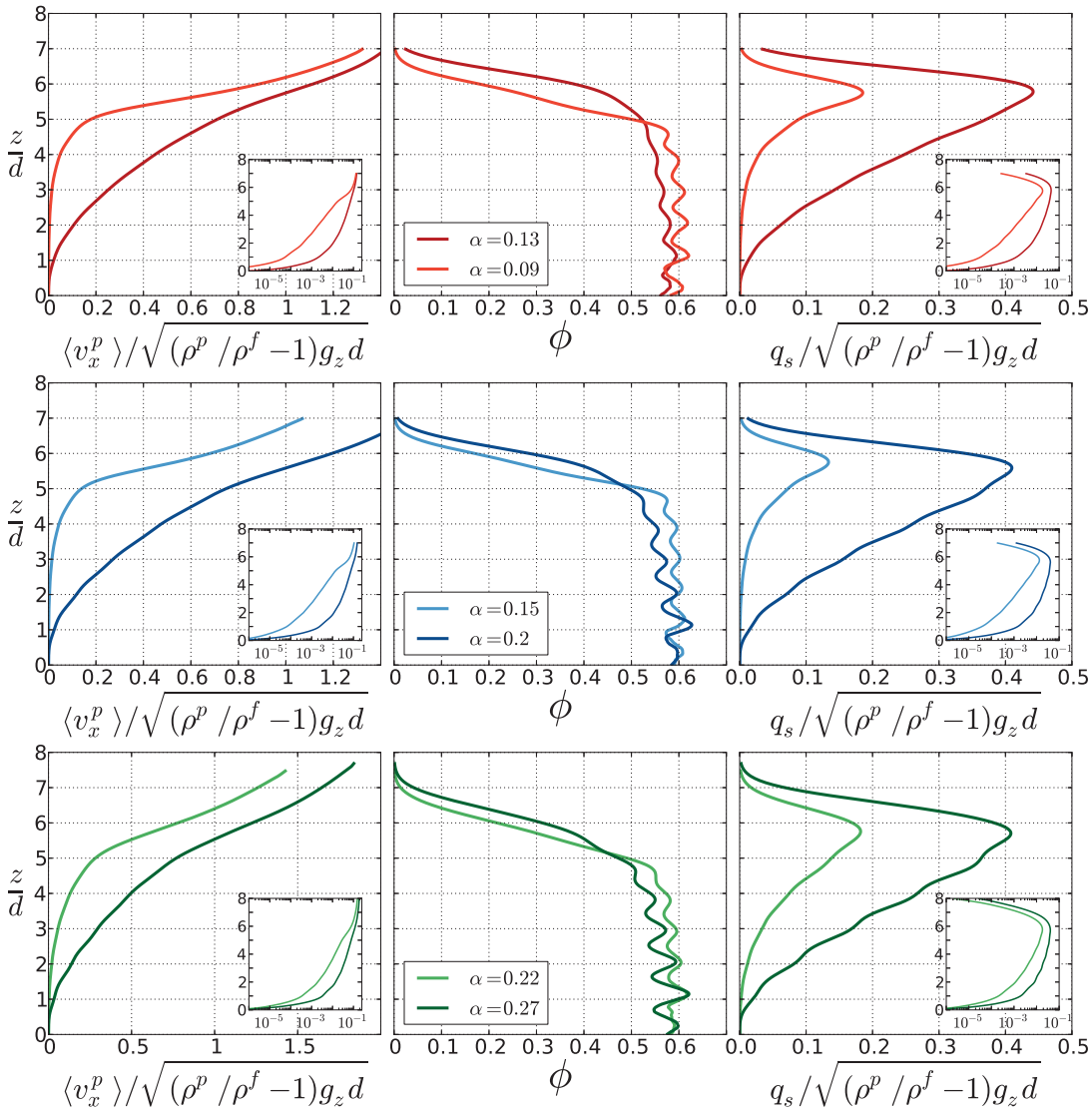

Figure 4.4: Normalized solid depth profiles for simulation at Shields number $\theta^* \sim 0.1$ above and below the critical slope angle, defining the transition to debris flow (equation 4.24). The three figures represents the transition for the three specific density sampled: $\rho^p/\rho^f - 1 = 0.75$ (red), 1.5 (blue) and 3 (green). The profiles above the transition are flowing down to the fixed bottom.

Figure 4.4 shows the solid depth profiles for each specific density, considering simulation with channel inclination above and below the critical slope angle α_0. For all the cases above this angle, the granular media is seen to flow down to the bottom, independently of the number of layers (see figure 4.5). Below the critical slope, the sediment rate is affected, but the granular flow is confined to the surface. Therefore,

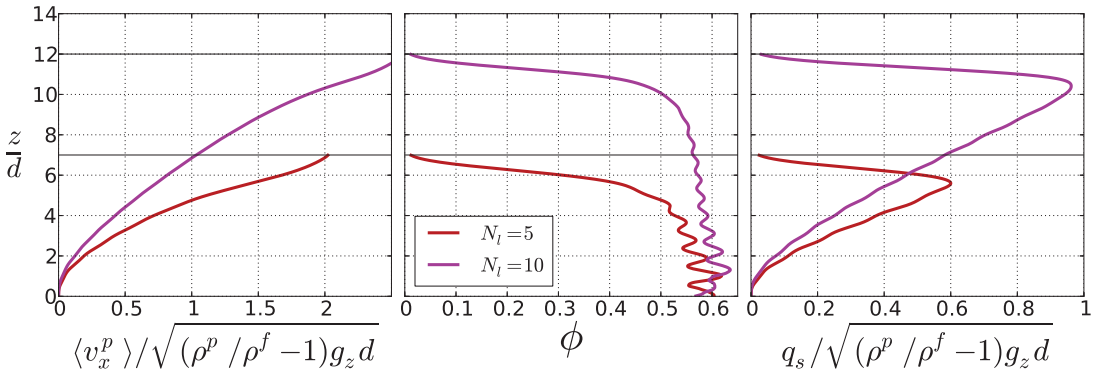

Figure 4.5: Normalized solid depth profiles for channel inclination angle above the critical slope angle defining the transition to debris flow (equation 4.24), for case with specific density $\rho^p/\rho^f - 1 = 0.75$. The black line represents the position of the water free-surface for the two simulations. Independently of the number of granular layer (N_l), the granular medium is observed to flow down to the fixed bottom.

the transition from bedload to debris flow is observed in the present simulations, and is well predicted by equation (4.24). In the following, the cases above the transition will be removed from the analysis, and only bedload transport configurations will be considered.

The variation of the slope and the specific density affects the stability of the granular layer, as it determines the "distance" to the critical slope in the phase space. Alternatively, it can be seen as affecting the effective static friction coefficient of the granular medium. As a consequence, it impacts directly the sediment transport rate. To quantify the latter, it is necessary to determine the scaling of the solid velocity profile with the parameters of the problem. Indeed, the solid volume fraction is dimensionless and does not show very important variations, while the solid velocity is observed to change importantly with the Shields number. Considering the dimensional analysis of the problem, the velocity should scale with the buoyant-free gravity $(\rho^p/\rho^f - 1)g$ and a characteristic length scale of the problem. The thickness of the mobile layer (eq. 4.22) contains all the problem dependencies, and is a good candidate. Considering the relatively low Shields number investigated, the surface contribution is expected to be less important than the two others. As a consequence, it is possible to take $\bar{\phi} \simeq \phi^{max}$, and the characteristic length scale of the problem δ reads:

$$\frac{\delta}{d} = \frac{\theta^*}{\phi^{max}\left[\mu_s - (1 + [\phi^{max}(\rho^p/\rho^f - 1)]^{-1})\tan\alpha\right]}. \tag{4.25}$$

Using equation (4.24), it can be rewritten as:

$$\delta = \frac{\theta^* d}{\phi^{max}\mu_s\left[1 - \tan\alpha/\tan\alpha_0\right]}. \tag{4.26}$$

From this expression, it is clearly related to the proximity with the critical slope $\tan\alpha_0$. The streamwise solid velocity is expected to scale as:

$$\mathcal{V} \sim \sqrt{(\rho^p/\rho^f - 1)g\delta}. \tag{4.27}$$

The dimensionless transport rate is the normalized integrated transport rate density. It reads:

$$Q_s^* \sim \frac{\phi^{max}\mathcal{V}\delta}{\sqrt{(\rho^p/\rho^f - 1)gd^3}} \sim \phi^{max}\left(\frac{\delta}{d}\right)^{3/2} \sim \left(\frac{\theta^*}{\mu_s\left[1 - \tan\alpha/\tan\alpha_0\right]}\right)^{3/2}. \tag{4.28}$$

To test the relevance of the proposed formulation, figure 4.6 shows the sediment transport rate as a function of both the Shields number (a) and the modified Shields number (b), for all the cases presented in table 4.1. The runs above the inclination angle of the transition to debris flow have been removed, and additional runs from the next chapter (see table 5.1) have been added. These additional simulations allows to investigate higher Shields and to observe the dependence on the particle diameter.

When re-scaling the Shields number, all the data collapse on a single master curve. It shows that the combined effect of the slope and the specific density are well captured by the modified Shields number defined by equation (4.26). In addition, the relevant length scale for the problem is not the diameter but δ, defined in equation (4.25). Indeed, the data with varying diameters added in figure 4.6 are all collapsing on the curve. Regarding the logarithmic scale inset of figure 4.6b, it exhibits a dependence to the square of the modified Shields number. Further simulations are needed to confirm the relevance of this exponent for higher values of modified Shields number. At low Shields number, it is difficult to distinguish between a clear exponent and a typical shape $(\theta^* - \theta_c^*)^n$. Considering the collapse, the point corresponding to the highest slope (⧫) is seen to be not well captured by the scaling. This deserves further investigation and additional simulations will be performed at higher slopes.

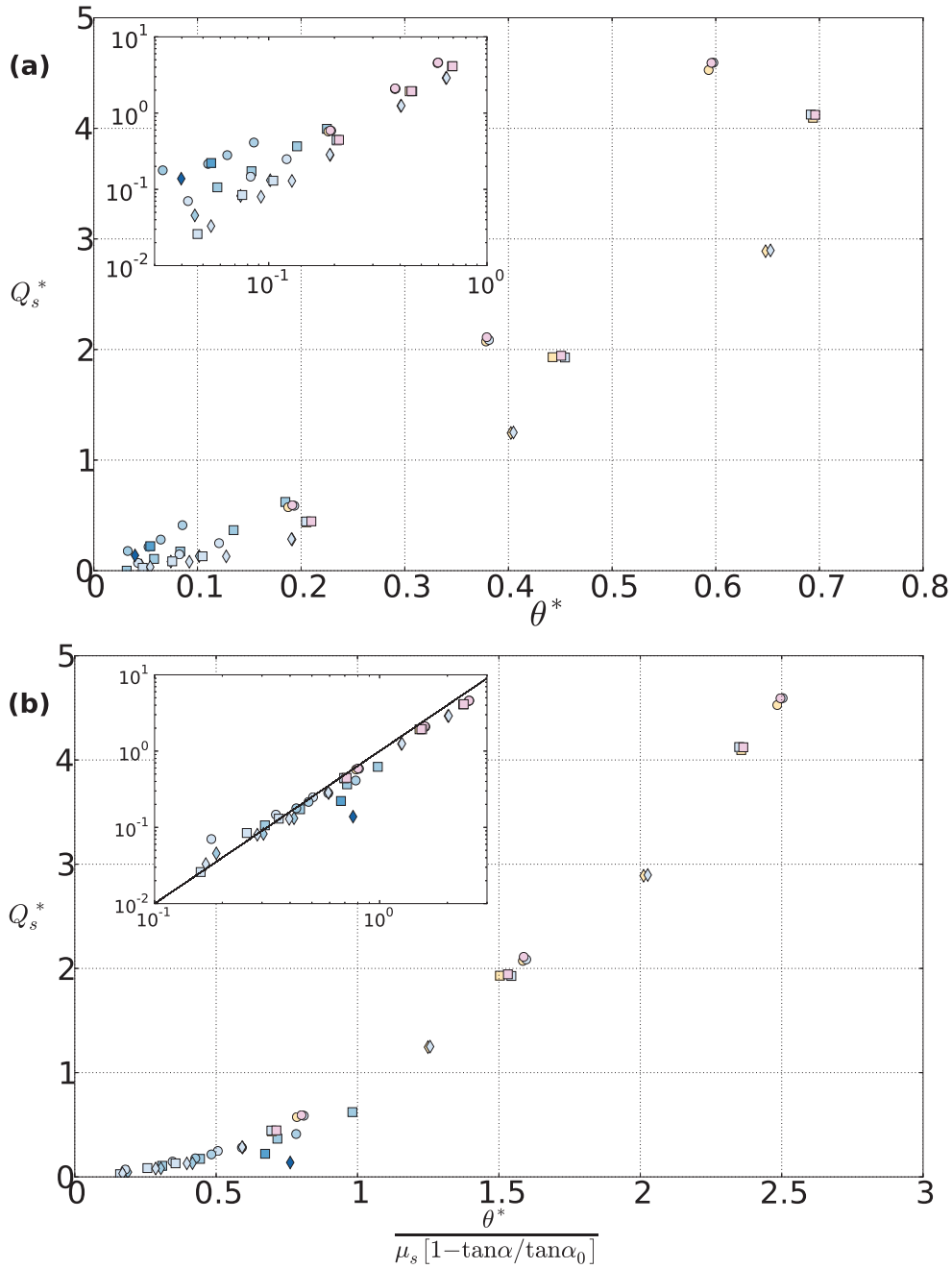

Figure 4.6: Sediment transport rate as a function of the Shields number (a) and the modified Shields number (b) defined by equation (4.26), for all the simulations in the bedload regime presented in table 4.1 and 5.1, with variation of slope, specific density, Shields number and particle diameter. The color change denotes the variation of the diameter from 3mm to 12mm, the color intensity reflects the slope, and the symbol is associated with the specific density. The inset shows the data in a logarithmic scale. The black line in the inset of (b) represents a trend of $Q_s^* \sim [\theta^*/\mu_s(1 - \tan\alpha/\tan\alpha_0)]^2$.

4.3.2 Sediment transport rate scaling

Regarding the literature on applied bedload transport, the results presented here are surprising. Indeed, in the field, some observations show an increase of the critical Shields number (*Rickenmann*, 2012; *Lamb et al.*, 2008; *Recking*, 2009) and a reduced sediment transport rate. The opposite effect is observed here. Classically, the increase of the critical Shields number is associated with the presence of emerging boulders in these low-submergence fluid flows, which modify the hydrodynamic conditions (*Lamb et al.*, 2008; *Recking*, 2009). In the present ideal case, the particle sample is monodisperse and the hydrodynamic is prescribed through a mixing length formulation, which reproduces a typical logarithmic fluid profile. While idealized, the configuration is relevant in order to help understand field mechanisms. The present results show the typical expected behavior in a simplified configuration. It confirms the intuitive view of the slope as a destabilizing effect, and therefore supports the idea of a modification of the transport conditions in the field. The latter can be affected by a variety of mechanisms at the grain scale, such as the hydrodynamic modification, or the granular shape and size-distribution effects. Further studies with e.g., a wider grain size distribution, would help to better understand the nature and the origin of this counter-intuitive effect.

4.4 Conclusion

The numerical model developed has been used to study the effect of the slope, specific density and particle diameter on the sediment transport rate. Increasing the inclination of the channel, a transition to debris flow is observed: the granular flows extend down to the fixed bottom independently of the number of particle layers. Interestingly, the angle of the transition depends on the specific density and can be predicted analytically. The dependence of the transition in specific density is explained by the influence of the fluid on the granular bed. Indeed, the effect of the slope in bedload transport, cannot be restricted to the geometrical effect on the grains and to the surface contribution of the fluid bed shear stress as proposed by *Fernandez Luque and Van Beek* (1976) and *Fredsøe and Deigaard* (1992). It has been shown analytically that another contribution comes into play. It represents the effect of the slope on the fluid flow, and is constant throughout the depth. For a static granular bed, it can be seen as the constant fluid flow in the bed, imposed by the inclination of the channel. This contribution reduces the apparent static friction coefficient of the granular material through the fluid-particle interaction, facilitating the entrainment of the particles by the surface fluid bed shear stress. It affects very importantly the granular flow in bedload transport, especially when considering high slopes and low specific densities. Accordingly, a rescaled Shields number has been proposed to account for these effects. The wide range of Shields number, slope, specific density and particle diameter covered in the numerical simulations,

have been shown to collapse along a single master curve, when considering the dimensionless sediment transport rate as a function of the modified Shields number. Therefore, the combined effect of the slope and the density can be seen as reflecting the distance to the transition to debris flow. The slopes close to the transition to debris flow, and the trend at higher modified Shields number remain to be better characterized. Future work will be dedicated to this extension.

In addition to these important findings, the results allow to understand the structure of the granular flow in terms of stress ratio repartition. The picture drawn from the present chapter will be further used to analyze the rheology of the granular phase in bedload transport in the next chapter.

Chapter 5

Granular rheology

For a given material, the rheology describes how a given material respond in terms of stress, to a given deformation rate, or equivalently how it flows when submitted to a given stress state. In bedload transport, the granular rheology governs both the response to, and the interaction with the fluid shear stress, and affects in consequence the transport rate. At steady state, the fluid shear stress can be first assimilated as an external forcing. However, the fluid can *a priori* influence the granular rheology, as it also affects the particles trajectories through drag for example. The characterization of the constitutive law for granular media in bedload transport can therefore help to improve the understanding of the phenomenon. Taking advantage of the coupled model developed, the present chapter analyzes the rheology of the granular phase in bedload transport. The methodology to compute the granular rheology is presented in section 5.1. The results are presented in section 5.2 and discussed in section 5.3.

5.1 Methodology

The numerical model described in chapter 2 is used with bi-periodic boundary conditions to study the bulk behavior of the granular flow at steady state. For simplicity, the turbulent velocity fluctuation model is turned off. In order to define properly an equivalent continuous medium for the granular phase, the analysis is restricted to cases with a non-negligible number of particle layers in motion. The range of Shields number explored has been chosen between $\theta^* \sim 0.2$ and $\theta^* \sim 0.6$ to stay in the bedload regime. It corresponds to high suspension number $S^* = w_s/u_* \in [2\ , 5]$. For mountain stream bedload, this represents intense rare events with high transport capacity. It can also be seen as a limit case of sheet flow, without suspension. The deposited bed at the beginning of the simulation is made of ten layers of grains, which is sufficient to avoid effects from the bottom boundary conditions in the range of parameters investigated.

5.1.1 Granular stress tensor

Formulation

To study granular rheology, it is needed to evaluate the stress tensor. Applying the volume averaging operator to the particle stress tensor, allows to compute from DEM the average particle stress tensor $\langle \sigma_{ij}^p \rangle$, for each slice of volume V (*Andreotti et al.*, 2013; *Goldhirsch*, 2010):

$$\langle \sigma_{ij}^p \rangle = -P^p \delta_{ij} + \tau_{ij}^p = -\frac{1}{V} \sum_{\alpha \in V} m^\alpha v_i'^\alpha v_j'^\alpha - \frac{1}{V} \sum_{c \in V} f_i^c b_j^c, \tag{5.1}$$

where the sum are respectively over the particles and the contacts contained in the volume V, $v_k'^\alpha = v_k^\alpha - \langle v_k \rangle$ is the k component of the spatial velocity fluctuation associated with particle α of mass m^α, $\mathbf{f}^c$ is the contact force applied by particle 1 on particle 2, and $\mathbf{b}^c$ is the branch vector from particle 1 to particle 2. This definition of the stress tensor contains two different terms which correspond respectively to the inertial and contact contributions to the stress tensor. The latter is also known as the Love-Weber stress tensor (*Love*, 1927), widely used in geomechanics. For cuboid weighting functions defined according to a mesh, some contacts stand between two averaging boxes. In this case the convention is to take into account the part of the branch vector contained in the box considered (*Andreotti et al.*, 2013). Physically, this is equivalent as supposing that the stress is evenly distributed along the branch vector for each contact. In reality, the stress is inhomogeneously located near the contact but this method allows to smooth the stress tensor profile, and is reasonable providing that statistical representativity is ensured.

Considering the unidirectional character of the problem, the goal is to obtain a depth profile of stress tensors. From the particle positions and contact forces, the stress tensor can be computed locally for each mesh cell along the wall-normal direction z, using equation (5.1). This evaluation does not influence the model so that the averaging properties can be chosen independently from the simulation ones. Figure 5.1 shows the shear and normal stress profiles with varying averaging wall-normal weighting function length scale. No influence of the averaging mesh size is observed as all the points are superimposed. Accordingly, the mesh could be chosen larger than in the simulation. However, to compute the rheology it is necessary to evaluate the shear rate which is obtained as the derivative of the average solid streamwise velocity in the present case. Consequently, the limiting parameter is not the stress tensor but the shear rate. Indeed, the spatial convergence of the shear rate profile with wall-normal averaging weighting function scale is similar to the one obtained for the solid velocity. Therefore, the same mesh as in the simulation will be adopted.

In the simple shear picture of the $\mu(I)$ rheology, the shear stress and the particulate pressure are given by respectively $\tau_{xz}^p(z)$ and $\tau_{zz}^p(z)$. However, granular media exhibit stress tensor asymmetry and normal sress differences. The former has been

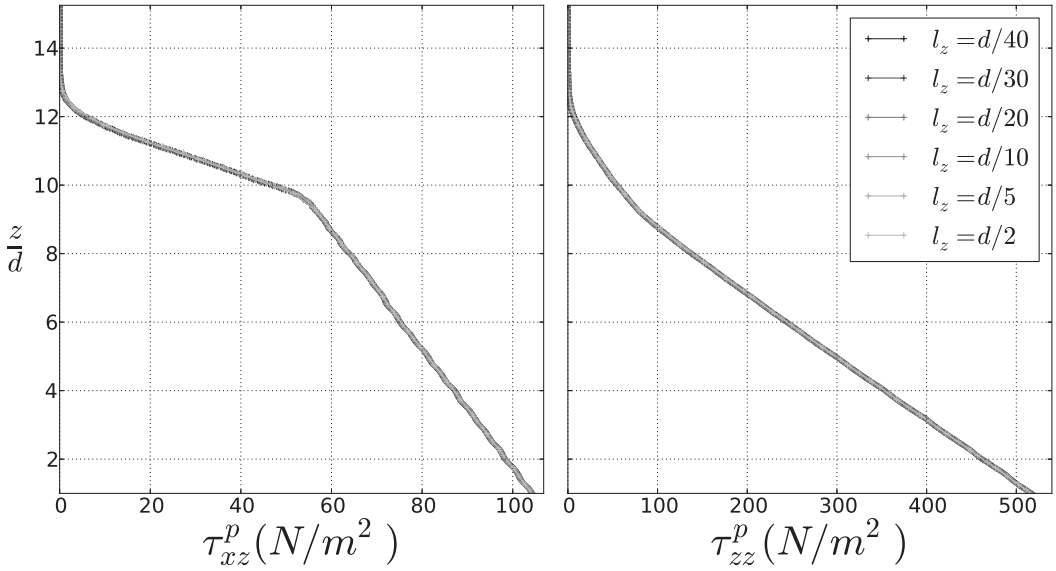

Figure 5.1: Normal (τ^p_{zz}) and shear (τ^p_{xz}) stress tensor depth profiles for different wall-normal averaging length scale l_z. All the profiles are superimposed, suggesting that they are independent from l_z in the range studied.

shown to be linked with the couple between the particles (*Goldhirsch*, 2010), while the latter is representative of the granular media anisotropy (*Weinhart et al.*, 2013). Figure 5.2 shows the stress asymmetry and normal stress difference observed in a typical simulation. While the normal streamwise and spanwise components presents differences with the particulate pressure defined as $P^p = -(\tau^p_{xx}(z)+\tau^p_{yy}(z)+\tau^p_{zz}(z))/3$, they compensate each other so that the wall-normal component $\tau^p_{zz}(z)$ follow the particulate pressure. Therefore, the latter two will be used equivalentely in the following. Concerning the asymmetry, it is shown (figure 5.2) to be negligible for the component of interests, so that $\tau^p_{xz}(z)$ will be used in the following.

5.1.2 Momentum balance

In order to validate the stress tensor profile computed, the momentum balance is analyzed in the framework of the continuous two-phase equations (*Jackson*, 2000). Using the steady and uniform character of the problem considered, the momentum balance along the streamwise direction reads (see chapter 4):

$$0 = \frac{\partial S^f_{xz}}{\partial z} + \frac{\partial R^f_{xz}}{\partial z} + \rho^f(1-\phi)g\sin\alpha - n\left\langle f^p_{f\,x}\right\rangle^p, \tag{5.2}$$

$$0 = \frac{\partial \tau^p_{xz}}{\partial z} + \rho^p\phi g\sin\alpha + n\left\langle f^p_{f\,x}\right\rangle^p. \tag{5.3}$$

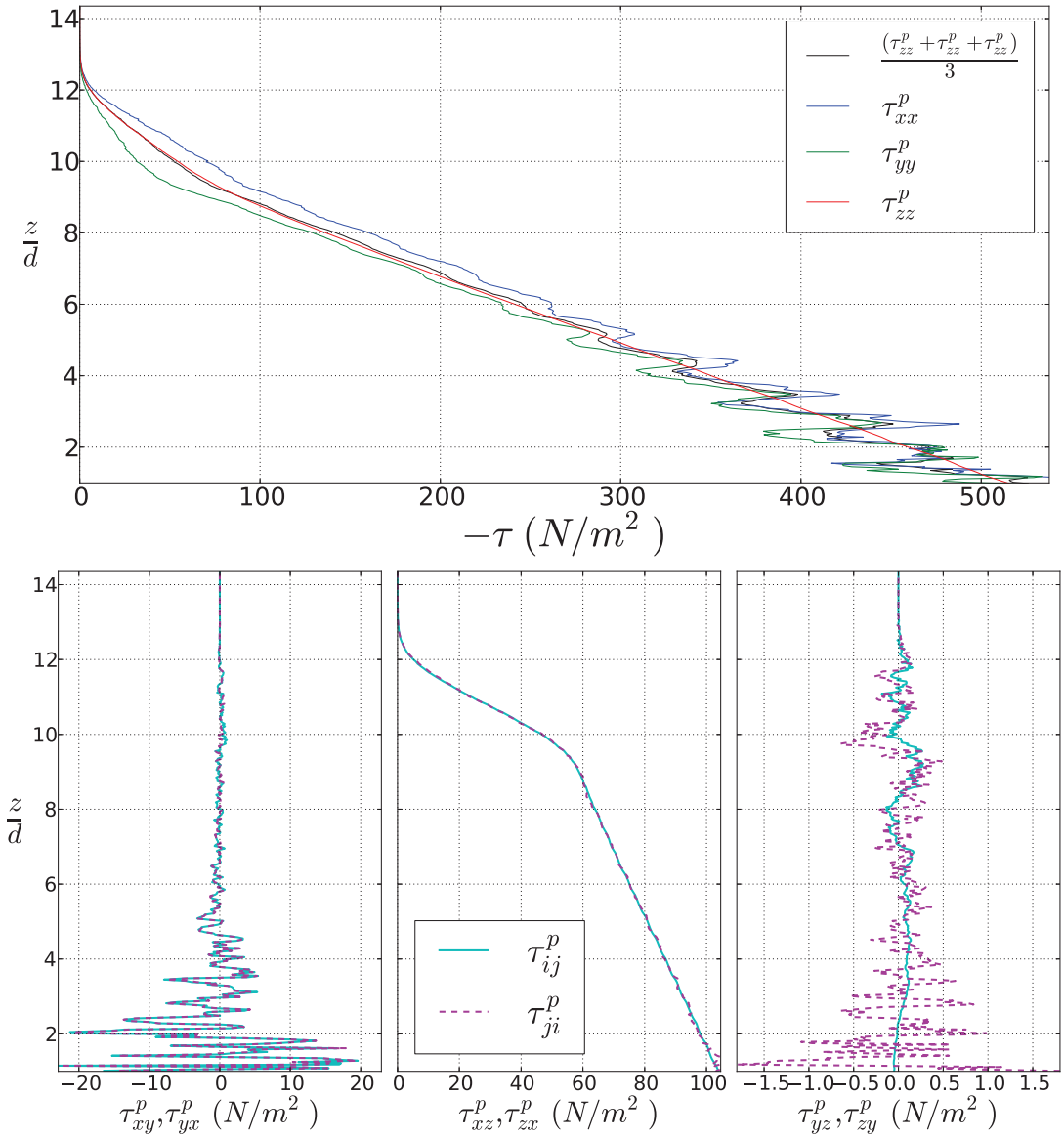

Figure 5.2: Profile of the different component of the stress tensors to evidence the stress asymmetry and normal stress differences. The stress asymmetry is negligible, and the wall-normal component $\tau^p_{zz}(z)$ is equivalent to the particulate pressure $P^p = -(\tau^p_{xx}(z) + \tau^p_{yy}(z) + \tau^p_{zz}(z))/3$.

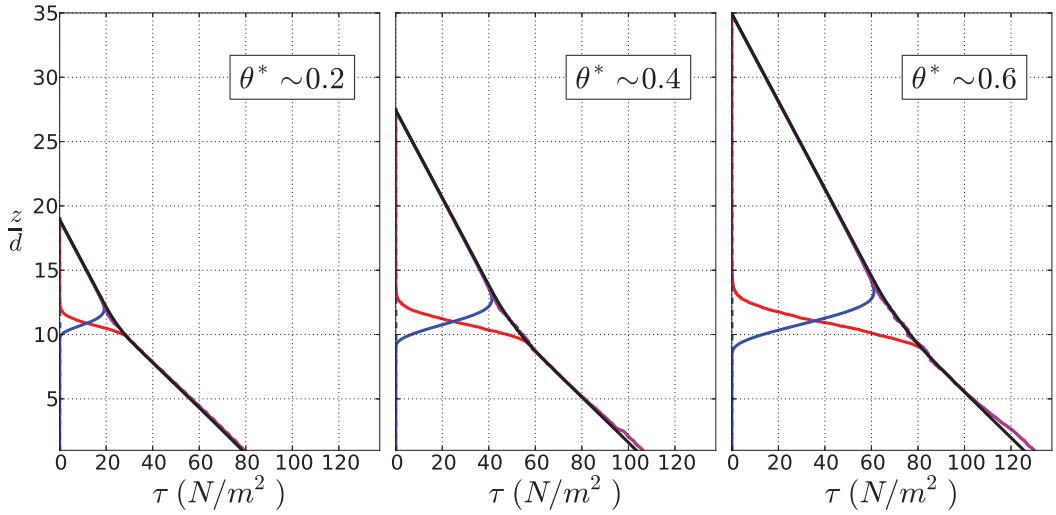

Figure 5.3: Fluid-particle mixture momentum balance terms along streamwise direction (eq. 5.5) as a function of the depth, for three different Shields number $\theta^* \sim 0.2,\ 0.4,\ 0.6$, with specific density $\rho^p/\rho^f - 1 = 1.5$ and particles diameter $d = 6mm$ (r2d6s1, r2d6s2 and r2d6s3 in table 5.1). The black curve represents the gravity term, the dashed and continuous blue lines are respectively the viscous and turbulent fluid shear stress, and the red line is the particle shear stress. The magenta line represents the sum of the latter three.

Combining these two equations together, the mixture momentum balance can be written as:

$$0 = \frac{\partial S^f_{xz}}{\partial z} + \frac{\partial R^f_{xz}}{\partial z} + \frac{\partial \tau^p_{xz}}{\partial z} + (\rho^p\phi + (1-\phi)\rho^f)g\sin\alpha. \tag{5.4}$$

In order to study the stress repartition, it is convenient to integrate this equation between a given position z in $h > z > 0$ and the water free-surface elevation h, where the viscous, turbulent, and particle shear stresses vanish: $S^f_{xz}(h) = R^f_{xz}(h) = \tau^p_{xz}(h) = 0$. It leads to the following formulation:

$$0 = -S^f_{xz}(z) - R^f_{xz}(z) - \tau^p_{xz}(z) + g\sin\alpha\left[\rho^f(h-z) + (\rho^p - \rho^f)\int_z^h \phi dz\right]. \tag{5.5}$$

From one simulation, it is possible to evaluate all the terms of the equation at each elevation. Providing the stress tensor formulation is appropriate and the system is at equilibrium, the equality should be satisfied. Figure 5.3 shows the different terms of the streamwise mixture momentum balance (eq. 5.5) for three different Shields number. The momentum balance are closed in each case, as the sum of the time-averaged stresses terms equals the gravity contribution. This gives credits to the computed stress tensor profiles, and shows that the situation considered are indeed at equilibrium. In addition, the viscous shear stress is observed to be a negligible contribution indepedently from the elevation. This has been observed for all the

cases analyzed in the framework of this PhD, and is consistent with former two-phase Eulerian sheet flow simulations (*Revil-Baudard and Chauchat*, 2013). Moreover, the depth structure can be divided into three parts depending on the strength of the different contributions. Indeed, the uppermost and lowermost region are respectively fully dominated by the turbulent and the intergranular shear stresses. In the central part a competition between these two contributions is observed. The latter region is representative of the mobilized granular layer, and is in consequence the main region of interest from the transport rate point of view. Therefore, the repartition of the stresses affects the structure of the granular flow. The evolution with increasing Shields number shows an increase of the vertical extent of the central region. This is classically associated with the mobile granular layer becoming thicker (*Wilson*, 1987).

The study of the vertical shear stress repartition has evidenced that the viscous shear stress component is negligible. In addition, it justifies the formulation of the granular stress tensor adopted, as the momentum balance has been observed to be closed. These results will serve as a basis for further analyzing of the granular flow rheology in bedload transport in the next section.

5.1.3 Computing the rheology

In the study of the granular rheology in bedload transport at steady state, the fluid is considered as an external forcing. It is embedded in the granular medium deformation, by imposing the shear rate profile. Thereore, bedload transport can be seen as a granular medium under a complex sollicitation that depends on the depth. From a granular point of view, the particularity of bedload transport stands in the variety of the encountered behaviors: from quasi-static in the bed, to dense and rapid granular flows at the interface with the fluid. Sampling the medium from top to bottom allows one to compute the whole spectrum of granular behavior with a single simulation.

The $\mu(I)$ rheology

In the dense regime, the $\mu(I)$ rheology is local, so that it is possible to compute the granular flow rheology at each elevation. To do so, the stress ratio, the solid volume fraction, and the inertial number have to be evaluated. Figure 5.4 presents the associated depth profiles for a single simulation. The inertial number varies over an impressive range ($I_{dry} \in [10^{-5}, 10^{1}]$) from the bottom to the top of the sample. The stress ratio and the solid volume fraction are, as expected, also variying along the depth. From the parameters value at each given elevation of the profiles, it is therefore possible to compute the $\mu(I)$ rheology. The curve obtained (figure 5.5) covers the full range of inertial number from quasi-static to dynamic. Each simulation produces a curve in the planes (μ,I) and (ϕ,I). The results will be detailed in

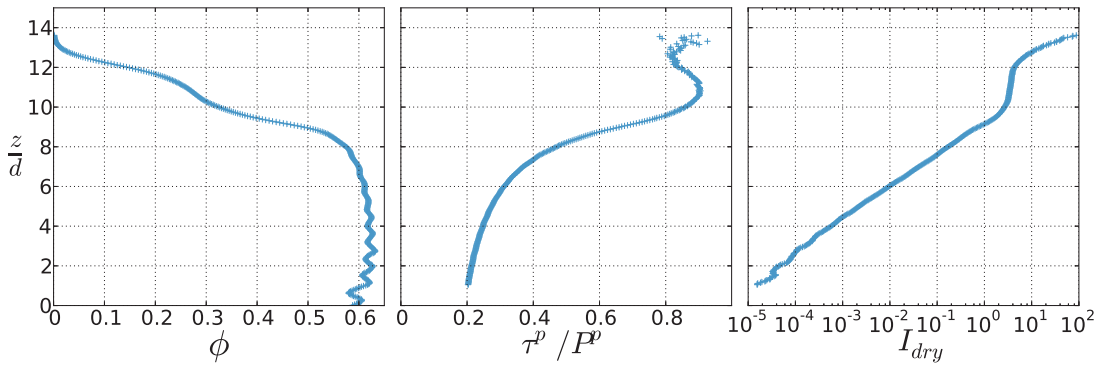

Figure 5.4: Depth profiles of solid volume fraction ϕ, shear to normal stress ratio $\mu = \tau^p_{xz}/\tau^p_{zz}$ and dry inertial number $I_{dry} = \dot{\gamma}d/\sqrt{\tau^p_{zz}/\rho^p}$ for a single simulation corresponding to case r2d6s2 in table 5.1. One simulation allows to sample an important range of inertial number averaging at different elevation.

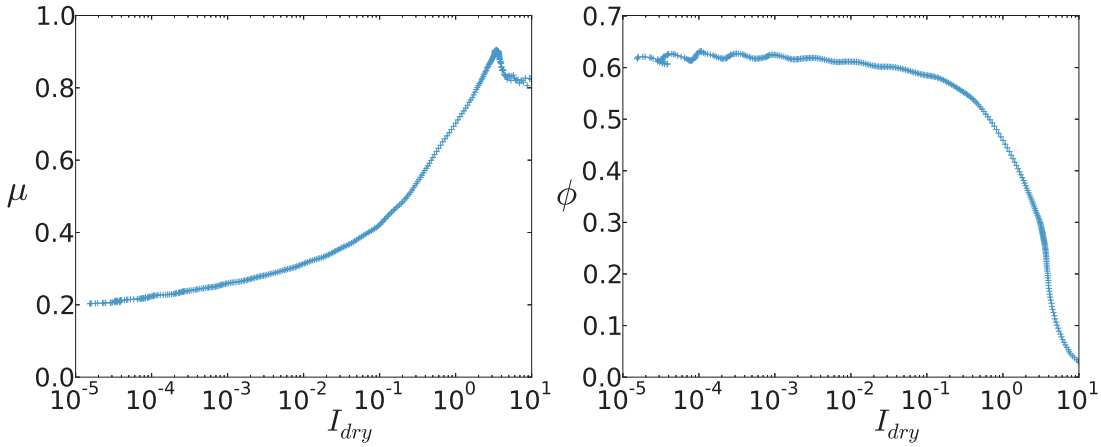

Figure 5.5: Shear to normal stress ratio $\mu = \tau^p_{xz}/\tau^p_{zz}$ and solid volume fraction ϕ as a function of the dry inertial number $I_{dry} = \dot{\gamma}d/\sqrt{\tau^p_{zz}/\rho^p}$ in semilogarithmic scale for a single simulation corresponding to case r2d6s2 in table 5.1.

next section.

The kinetic theory

The uppermost layer of bedload transport can be assimilated to a rapid granular flow. Therefore, the collisional layer formed above the bed should, in principle, be described by the kinetic theory of granular gases (*Jenkins and Hanes*, 1998; *Hsu et al.*, 2004). In order to compare our numerical simulation with the kinetic theory of granular gases, it is necessary to evaluate the granular temperature. Similarly to the stress tensor, for each slice of volume V, at wall-normal position z, the granular

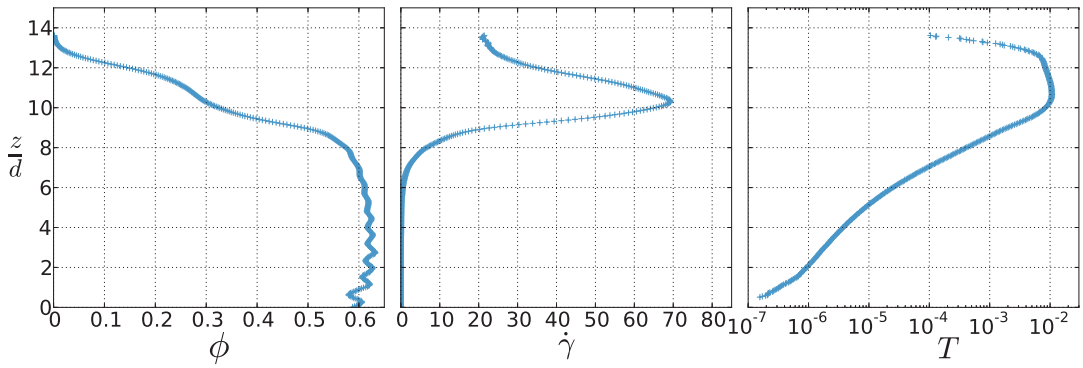

Figure 5.6: Solid volume fraction (ϕ), shear rate ($\dot{\gamma}$) and granular temperature (T) depth profiles for a single simulation corresponding to case r2d6s2 in table 5.1.

temperature can be computed as (*Lun et al.*, 1984; *Jenkins and Berzi*, 2010):

$$T(z) = \frac{\left\langle v_x' v_x' + v_y' v_y' + v_z' v_z' \right\rangle^s (z)}{3} = \frac{1}{N} \sum_{\alpha \in V} \frac{v_x'^{\alpha} v_x'^{\alpha} + v_y'^{\alpha} v_y'^{\alpha} + v_z'^{\alpha} v_z'^{\alpha}}{3}, \tag{5.6}$$

with N the number of particles contained in the slice V. The kinetic theory predicts the scaling of the normalized shear and normal stress components, as a function of the solid volume fraction and restitution coefficient:

$$\tau_{xz}^p = f_1(\phi, e_n) \rho^p \dot{\gamma} d \sqrt{T}, \tag{5.7}$$

$$\tau_{zz}^p = f_2(\phi, e_n) \rho^p T. \tag{5.8}$$

These scaling are dimensional, and the differences between the approaches of the kinetic theory lie in the formulation of f_1 and f_2. These functions depend on the pair distribution function adopted and the restitution coefficient value.
Therefore, to compute the scalings and the predictions of the kinetic theories as a function of the depth, it is necessary to evaluate the solid volume fraction, the shear rate and the granular temperature. Figure 5.6 presents these three parameters for a single simulation. Similarly to the $\mu(I)$ rheology case, a wide range of granular temperature and solid volume fraction is covered. Each simulation produces a curve in both shear and normal stress components plane as a function of the solid volume fraction.
The systematic study of bedload transport cases should therefore bring an important statistics on the analysis of the granular rheology.

Table 5.1: Parameters of the simulations studied and symbol correspondence. The specific density, particle diameter, and Shields number have been varied. Each specific density is associated with a color, which intensity reflects the Shields number. The symbol associated with the run is characteristic of the particles diameter.

Run	$\rho^p/\rho^f - 1$	$d(mm)$	θ^*	Q_s^*	symbol
r1d3s1	0.75	3	0.188	0.574	●
r1d3s2	0.75	3	0.378	2.073	●
r1d3s3	0.75	3	0.593	4.527	●
r1d6s1	0.75	6	0.193	0.587	+
r1d6s2	0.75	6	0.381	2.086	+
r1d6s3	0.75	6	0.598	4.593	+
r1d12s1	0.75	12	0.191	0.592	x
r1d12s2	0.75	12	0.379	2.111	x
r1d12s3	0.75	12	0.596	4.592	x
r2d3s1	1.5	3	0.205	0.438	●
r2d3s2	1.5	3	0.443	1.931	●
r2d3s3	1.5	3	0.694	4.095	●
r2d6s1	1.5	6	0.205	0.445	+
r2d6s2	1.5	6	0.455	1.928	+
r2d6s3	1.5	6	0.692	4.125	+
r2d12s1	1.5	12	0.21	0.446	x
r2d12s2	1.5	12	0.451	1.943	x
r2d12s3	1.5	12	0.696	4.122	x
r4d3s1	3	3	0.191	0.282	●
r4d3s2	3	3	0.402	1.245	●
r4d3s3	3	3	0.648	2.889	●
r4d6s1	3	6	0.191	0.285	+
r4d6s2	3	6	0.405	1.25	+
r4d6s3	3	6	0.653	2.896	+

5.2 Results

In order to investigate the scaling laws, the Shields number, particle to fluid density ratio, and particle diameter are varied. This allows to identify trends and key dimensionless numbers in bedload transport. To restrict our study to bedload transport while changing the density ratio, the channel inclination angle is fixed to $\alpha = 0.05$. For each parameter, three values are considered. All the simulation parameters are given in table 5.1.

Figure 5.7 presents the stress ratio and the solid volume fraction as a function of the inertial number for all the cases considered. The colors are associated with the specific density, while their intensities are linked to the Shields number value, and the symbols corresponds to the particle diameter. The figure shows a good collapse

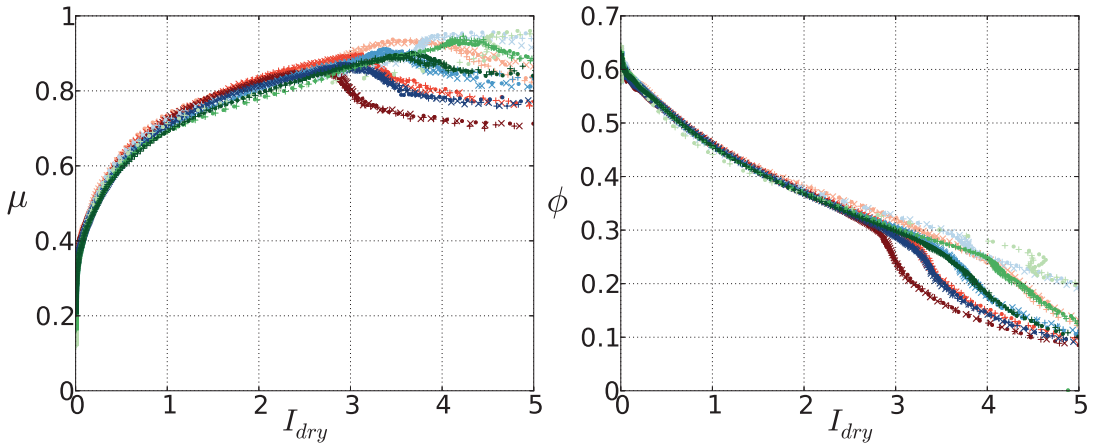

Figure 5.7: Shear to normal stress ratio $\mu = \tau^p_{xz}/\tau^p_{zz}$ and solid volume fraction ϕ as a function of the dry inertial number $I_{dry} = \dot{\gamma}d/\sqrt{\tau^p_{zz}/\rho^p}$ for all the cases presented in table 5.1 with variation of Shields number, specific density and particle diameter. The parameters of the simulation sampled and the corresponding symbols are shown in table 5.1.

of the data for both the stress ratio and the solid volume fraction up to inertial number of the order of three: $I_{dry} \sim 3$. All the curves show an increasing trend of the stress ratio, followed by decrease. The maximum value and its position in terms of inertial number depend on the runs. Associated with this maximum, a change is observed in the solid volume fraction, where the curves drop down suddenly with increasing inertial number. The results can be splitted into three parts corresponding to both a change of behavior in terms of rheology and a different zone in the depth structure of bedload transport: the quasi-static granular layer at the bottom of the sample associated with low inertial numbers ($I_{dry} < 10^{-3} - 10^{-2}$) and high solid volume fraction ($\phi \sim 0.6$); the dense granular flow layer corresponding to intermediate inertial number ($I_{dry} \in [10^{-2}, 3]$) and solid volume fraction ($\phi \in [0.3, 0.6]$); and lastly the dilute ($\phi < 0.3$) upper layer which can be assimilated as rapid granular flows ($I_{dry} > 1$). Therefore, the following subsections will focus on the different part of the flow independently (section 5.2.2 to 5.2.4). Before presenting these results, the choice to adopt the dry inertial number is discussed.

5.2.1 Interstitial fluid influence

Following the generalization of the $\mu(I)$ rheology to cases with interstitial fluid (*Courrech du Pont et al.*, 2003; *Cassar et al.*, 2005), the inertial number should depend on the regime sampled, defined by the position in the (St,r) diagram (figure 5.8). In the present case, the coarse particle size combined with the low viscosity of water lead to high Stokes numbers, and all the simulations belong to regimes where $St >> 1$. The dimensionless number $r = \sqrt{\rho^p/(\rho^f C_D)}$ is of order one in the

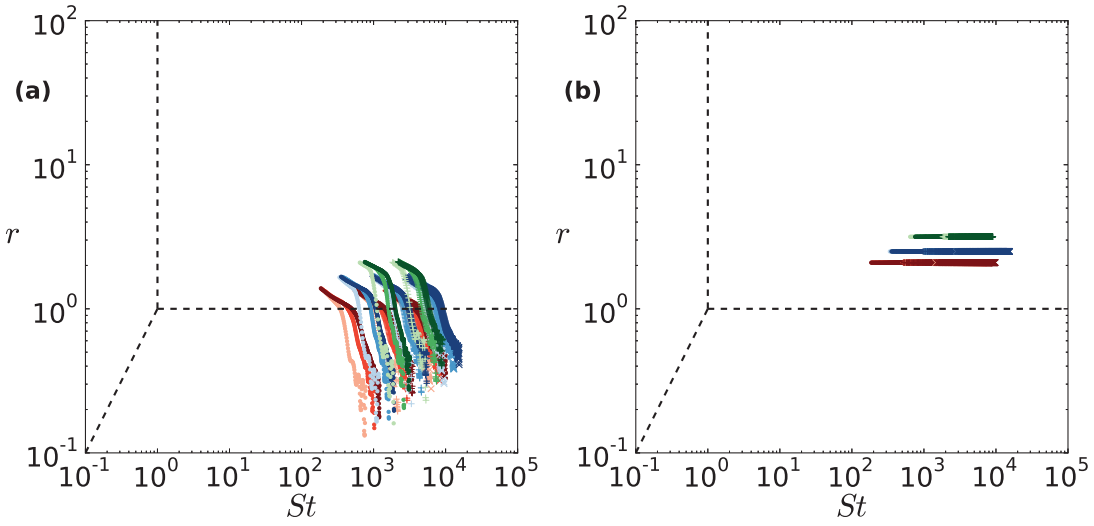

Figure 5.8: Stokes number $St = d\sqrt{\rho^p P^p}/\eta^f$ and $r = \sqrt{\rho^p/(\rho^f C_D)}$ phase diagram with all the data (see table 5.1) plotted considering local $C_D(z) = (24.4/Re_p(z) + 0.44)(1-\phi(z))^{-3.1}$ (a) and global $C_D = 0.4$ (b) determination of the drag coefficient.

simulations considered (figure 5.8), close to the transition from turbulent to free-fall regime. Therefore, the evaluation of the r number and the position of the transition r_c in the (St,r) diagram are of primary importance. In previous works, *Courrech du Pont et al.* (2003) and *Izard* (2014) used a global constant drag coefficient ($C_D = 1/\pi$) to compute r. *Cassar et al.* (2005) adopted the same approach taking into account, the global effect of the solid volume fraction on the drag coefficient. The position of the transition between free-fall and turbulent regimes r_c has been studied first by *Courrech du Pont et al.* (2003), who predicted $r'_c = \sqrt{5\rho^p/3\rho^f} \sim 4$. More recently, *Izard* (2014) analyzed underwater granular avalanches by means of DNS-DEM simulations, and found no evidence of the transition when sampling values of $r' = \sqrt{5\rho^p/(3\rho^f)}$ from 2 to 11 and St from 10^{-1} to 10^2.

In the present case, the drag coefficient evolves importantly from top to bottom, due to the change in solid volume fraction and particle Reynolds number. Accordingly, it seems more appropriate to use the local drag coefficient, as it is driving the local re-arrangements. As a matter of comparison, the values computed from a constant global drag coefficient $C_D = 0.4$ are shown in figure 5.8b. With the latter expression, r depends only on the density ratio. All the simulations gather around three lines at constant r and varying Stokes number, corresponding to the three density ratio studied. Using the critical transition value predicted by *Courrech du Pont et al.* (2003) ($r_c = 2$[1]), all the simulations belong to the free-fall regime. Conversely, the local definition (figure 5.8a) induces a set of curves varying as a function of both St and r number, mostly situated in the turbulent regime.

[1]equivalent to $r'_c = 4$ with $C_D = 1/\pi$

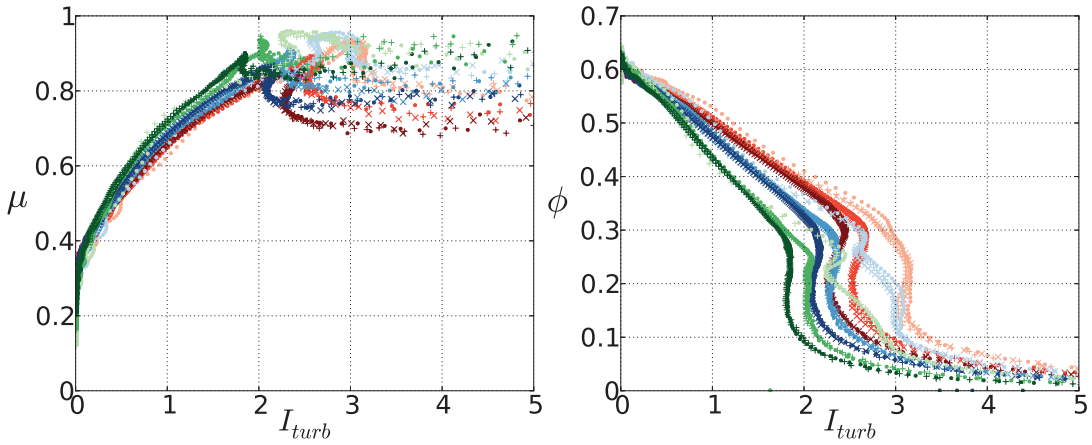

Figure 5.9: Shear to normal stress ratio $\mu = \tau^p_{xz}/\tau^p_{zz}$ and solid volume fraction ϕ as a function of the turbulent inertial number I_{turb}, for all the cases presented in table 5.1 with variation of Shields number, specific density and particle diameter.

These two results show the importance of the choice of the drag coefficient, and suggests that a transition to the turbulent regime might occur in the simulations. Regarding the prediction of *Courrech du Pont et al.* (2003), a non-negligible part of the curves should collapse as a function of the turbulent inertial number. Figure 5.9 shows the results of the shear to normal stress ratio and solid volume fraction as a function of the turbulent inertial number. No collapse of the data is observed. It suggests that the range of parameters considered belongs to the free-fall regime. Accordingly, the dry inertial number is the dimensionless number of interest in the present case, and it will be adopted in the following analysis. The absence of turbulent inertial number scaling for local r number lower than the transition one, questions the existence of the turbulent regime for granular media. Indeed, realistic granular media in turbulent flows present a density greater than the surrounding fluid, so that it is very unlikely to have $\rho^p/\rho^f < 1$. In addition, high drag coefficient at relatively high particle Reynolds number ($St >> 1$) are only possible if the hindrance effects are important, i.e. near packing fraction for which granular media behaves mainly as quasi-static. Consequently, the turbulent regime is at least very restricted, and possibly not existing for granular media.

5.2.2 Quasi-static behavior

The low inertial number behavior is revealed by adopting a semi-logarithmic scale (figure 5.10). In term of solid volume fraction, the data from the different simulations collapse until the lowest inertial number. For the stress ratio, the collapse is observed only down to inertial number $I_{dry} \sim 10^{-2}$. Below, the curves follow different paths depending on the specific density and Shields number of the run considered. In this

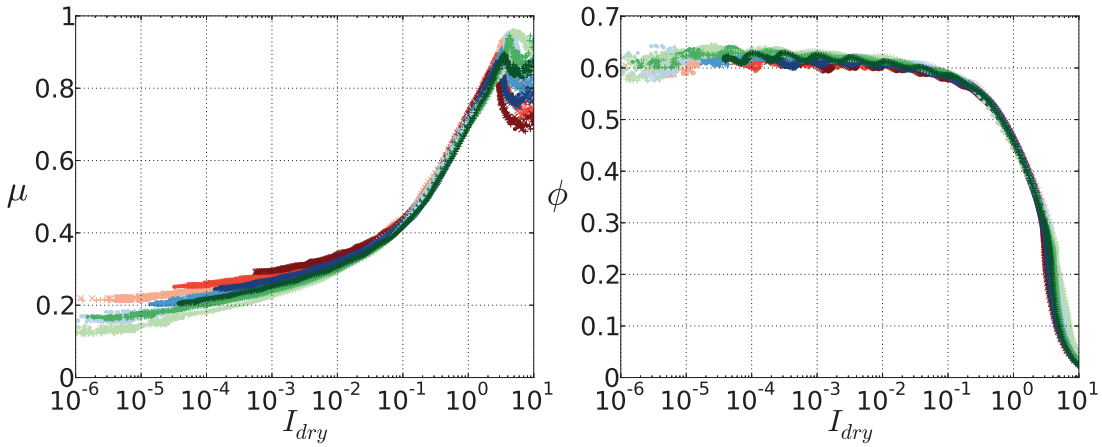

Figure 5.10: Shear to normal stress ratio and solid volume fraction as a function of the dry inertial number in semilogarithmic scale, for all the cases presented in table 5.1.

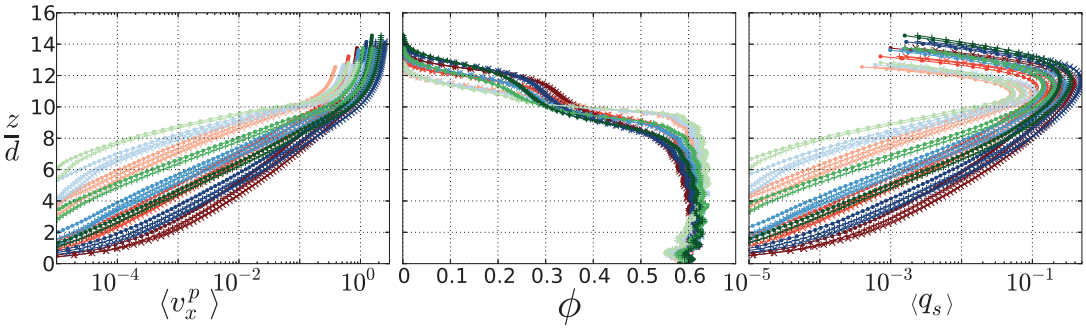

Figure 5.11: Solid velocity, volume fraction and transport rate density profiles for all the simulations considered in the present chapter (see table 5.1).

region, the values of the stress ratio are below the expected static effective friction of the granular media ($\mu_s \sim 0.38$ for monodisperse glass beads (*Andreotti et al.*, 2013)). Meanwhile, the associated solid volume fraction is seen to saturate to the maximum packing fraction, slightly greater than $\phi = 0.6$.

Figure 5.11 shows the solid depth profiles for all the simulations presented. An exponential decrease is observed in the velocity profile with decreasing wall-normal position z. This is characteristic of the creeping regime observed in dry granular media (*Komatsu et al.*, 2001; *Richard et al.*, 2008). This regime, together with the values of stress ratio lower than the static friction, are the signature of non-local effects (e.g. *Kamrin and Koval* (2012); *Bouzid et al.* (2013)). In such cases, the flow is influenced by the far-field and the stress ratio should depend on the surface flow condition. Following *Bouzid et al.* (2013), the signature of the surface flow is contained in the length scale associated with the solid velocity exponential decrease. The latter is indeed varying with simulation parameters (figure 5.11), supporting

the idea that it is linked to the surface flow condition and the stress ratio observed. The creeping regime is associated with alternance of long period without significant motion, with sudden fast jump of the particle (*Richard et al.*, 2008). It suggests a behavior based on collective re-arrangements between period of rests, which corresponds well to what is observed in the present simulations and experimentally (*Frey*, 2014).

The presence of creeping in the granular phase has been observed in recent experiments on laminar bedload in annular cell (*Houssais et al.*, 2015). It may have consequences on bedload transport through the influence on the granular phase compaction. The latter affects the incipient motion, but has no impact on steady uniform bedload (*Ouriemi et al.*, 2009). Contrary to *Houssais et al.* (2015) no drastic change in the exponential decrease of the particle velocity profile has been observed. This difference is probably linked to the channel inclination which induces a constant velocity flow in the lowermost part of the present configuration, whereas fluid velocity is only due to the surface liquid flow in the experimental annular setup of *Houssais et al.* (2015)[2].

The quasi-static lowermost part of bedload transport shows interesting granular features but does not influence importantly the sediment transport rate. While it can influence out-of-equilibrium problem such as incipient motion, it is not of fundamental importance for the analysis of steady uniform conditions in bedload transport above the threshold of motion.

5.2.3 Dense granular flows

As mentioned previously, in the dense granular flow part ($I_{dry} \in [10^{-2}, 3]$), a collapse of the curves from the different simulations is observed for both the stress ratio and the solid volume fraction as a function of the inertial number (figure 5.7 and 5.10). The collapse is observed up to particularly high values in terms of inertial number, with respect to what is classically observed in dry granular flows (e.g. *Da Cruz et al.* (2005); *Jop et al.* (2006); *Forterre and Pouliquen* (2008); *Jop* (2015)). In the classical dry granular flow setups such as the inclined plane, the steady state configurations are limited to inertial number lower than 0.5. Therefore, the saturation of the effective friction coefficient at high inertial number contained in the $\mu(I)$ rheology ($\mu \to \mu_2$ in eq. 5.9), is an extrapolation of the behavior observed at moderate inertial numbers. *Holyoake and McElwaine* (2012) studied the inclined plane configuration for accelerated dry granular flows, in steep channel with lateral walls and a bumpy base. The important size of the setup and the recirculation of granular materials allowed them to measure steady non-uniform flows, and sample inertial number up to $I_{dry} \sim 2$. No saturation was observed in the value of the stress

[2]As seen in the previous chapter, this fluid flow can become of importance at steep slopes or low specific density.

ratio, going as high as $\mu \sim 0.75$. *Börzsönyi et al.* (2009) studied numerically the granular instability of rolling waves on an inclined plane and computed the local rheology. They found a collapse of the data up to $I_{dry} \sim 1$. Relatively high inertial number ($I_{dry} \sim 1$) have also been measured with a recent technique, considering low granular flow depth on inclined plane in steady uniform conditions (*Faug et al.*, 2015). Configurations such as the super stable granular heap (*Taberlet et al.*, 2003) also shows stable dense granular flows at very high inclination angle suggesting high inertial numbers.

In the present study, the collapse of the data goes higher in terms of inertial number than anything previously observed ($I_{dry} \sim 3$). The above cited examples suggest that the possibility to obtain steady dense granular flows at high inertial number depends on the nature of the setup considered. The local analysis coupled with the particular configuration, might be at the origin of this unusally high collapse.
For dense granular flows, the effective friction coefficients observed seems however to be general. Comparing the value of the effective friction coefficient for inertial number $I_{dry} = 2$ obtained in this study with the one obtained by *Holyoake and McElwaine* (2012), a relatively good agreement is obtained ($\mu \sim 0.80$ against $\mu \sim 0.75$). Therefore, it is interesting to characterize the observed trend as a function of the inertial number, for the effective friction coefficient and the solid volume fraction. The high inertial numbers observed are not compatible with the usual expression for the effective friction coefficient and solid volume fraction as a function of the inertial number (eq. 1.8 and 1.9):

$$\mu(I) = \mu_1 + \frac{\mu_2 - \mu_1}{I_0/I + 1} = \mu_1 + (\mu_2 - \mu_1)\frac{I}{I_0 + I}, \tag{5.9}$$

$$\phi(I) = \phi^{max} - bI. \tag{5.10}$$

Indeed, figure 5.12 shows the results of these expressions with classical values of the phenomenological constants (*Jop et al.*, 2006): $\mu_1 = 0.38$, $\mu_2 = 0.64$, $I_0 = 0.279$ (dashed line). It shows a poor agreement with the data observed in the present study. In particular, the saturation when increasing inertial number is not observed. Performing a best fit of the constants, a better agreement is obtained (black continuous line in figure 5.12, with $\mu_1 = 0.35$, $\mu_2 = 0.97$, $I_0 = 0.69$, $\phi^{max} = 0.61$, $a = 0.31$). However, the constant increasing slope exhibited in the semi-logarithmic plot is not reproduced, suggesting that the shape of the function is not appropriate. For the solid volume fraction, the linear shape classically employed deviates importantly from the data when increasing the inertial number (figure 5.12). The following function fits well the results:

$$\phi(I) = \frac{\phi^{max}}{1 + aI}, \tag{5.11}$$

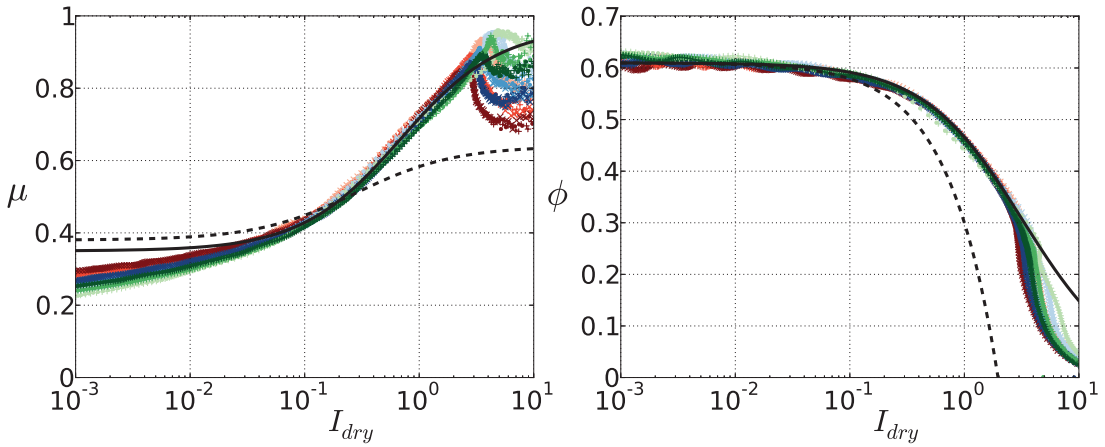

Figure 5.12: Shear to normal stress ratio and solid volume fraction as a function of the dry inertial number, for all the cases presented in table 5.1. The dashed black line represents the equations 5.9 and 5.10 with the parameters of *Jop et al.* (2006) ($\mu_1 = 0.38$, $\mu_2 = 0.64$, $I_0 = 0.279$), $\phi^{max} = 0.61$, and $b = 0.31$). The continuous black line represents the best fit from equations 5.9 and 5.11 of the data in the dense regime with $I_{dry} > 10^{-2}$ ($\mu_1 = 0.35$, $\mu_2 = 0.97$, $I_0 = 0.69$, $\phi^{max} = 0.61$, $a = 0.31$).

with $a = 0.31$ (see figure 5.12). This expression is similar to the expression used by *Boyer et al.* (2011), *Aussillous et al.* (2013) and *Revil-Baudard and Chauchat* (2013). At first order, the classical shape of equation (5.10) is recovered.

5.2.4 Rapid granular flows

Considering higher inertial number, no collapse of the data is observed (figure 5.7 and 5.12). At a given inertial number I_c depending on the run considered, the stress ratio decreases and the solid volume fraction trend changes suddenly. A transition to rapid granular flows dominated by particle velocity fluctuations and granular temperature gradient is expected. The prediction of the kinetic theory for the stress ratio can be expressed as a function of the inertial number (*Forterre and Pouliquen*, 2008). It shows two unstable branches exhibiting a decreasing trend with increasing inertial number (see figure 5.13). Eventually it crosses the increasing $\mu(I)$ rheology (eq. 5.9) at a critical inertial number depending on the restitution coefficient (*Lois et al.*, 2006). Performing local averaging on numerical simulation of inclined plane rolls instabilities, *Börzsönyi et al.* (2009) evidenced a decreasing trend of the collapse observed, at inertial number $I_{dry} > 0.8$. In the present case, the decreasing trend is observed for $I_c > 3$, and the value of I_c is different for each run. The lower restitution coefficient adopted here ($e_n = 0.5$ against $e_n \in [0.80, 0.95]$ in *Börzsönyi et al.* (2009)) might justify the presence of the transition at higher inertial number, but the variation of the transition with the runs remains unexplained.

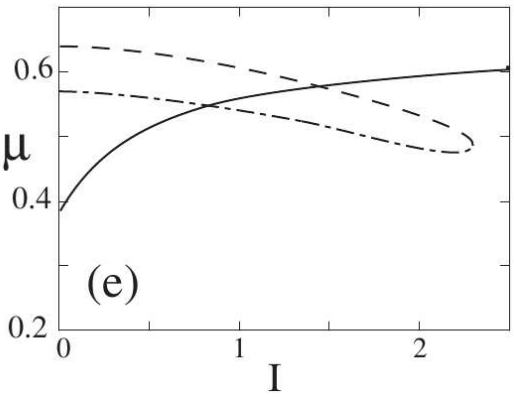

Figure 5.13: Prediction of the $\mu(I)$ phenomenological rheology ((–) eq. 5.9 with $\mu_1 = 0.38$, $\mu_2 = 0.65$, $I_0 = 0.3$) and kinetic theory of *Lun et al.* (1984) with $e_n = 0.6$ (- -), for the effective friction coefficient as a function of the inertial number. After *Forterre and Pouliquen* (2008).

To better understand the nature of the regime observed, it is interesting to consider the kinetic theory predictions (*Campbell*, 1990; *Goldhirsch*, 2003). Figure 5.14

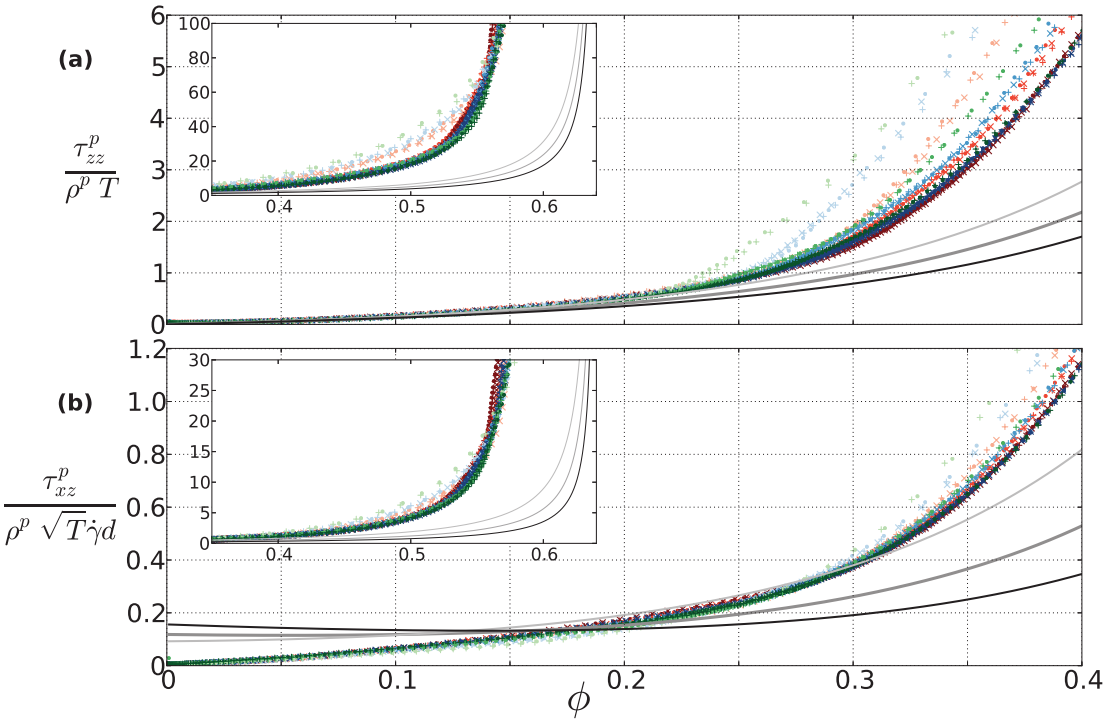

Figure 5.14: Normalized shear and normal component of the stress tensor as a function of the solid volume fraction for all the cases presented in table 5.1 with variation of Shields number, specific density and particle diameter. The lines represents the prediction of the kinetic theory of *Garzó and Dufty* (1999) with $e_n = 0.1$ (–), $e_n = 0.5$ (–), $e_n = 1$ (–).

shows the shear and normal stresses rescaled in the kinetic theory framework, as a function of the solid volume fraction. Considering dilute conditions ($\phi \in [0.08, 0.3]$), the data collapse well. The prediction of the kinetic theory have been computed considering the formulation of *Garzó and Dufty* (1999), in the simplified version of *Jenkins and Berzi* (2010) (eq. 2-8 in their paper), and setting the restitution coefficient to the adopted value in the simulation ($e_n = 0.5$). The comparison with the results (middle grey line in figure 5.14), shows that the trend of the shear stress is not well described. For the normal stress component, the prediction is good below $\phi \sim 0.2$. However, it should be noted that $\phi = 0.08$ is usually taken as a lower validity limit to define a granular rheology[3]. Therefore, the range of solid volume fraction where the prediction of the kinetic theory is accurate for the normal stress component is narrow. As a matter of comparison, the prediction of the kinetic theory for restitution coefficient $e_n = 0.1$ and $e_n = 1$ are also plotted on figure 5.14. It further illustrates the poor agreement with the simulations.

The analysis of the granular rheology in bedload transport exhibits the features of the three regimes of granular media, and shows behaviors challenging the established rheologies. The dense regime is observed to persist until unexpectedly high inertial number, depending on the structure of the granular flows (variation of θ^* and $\rho^p/\rho^f - 1$). Above, the behaviors observed show signatures of rapid granular flows, but does not seems to be well described by the kinetic theory predictions. The repartition between the different regime and the nature of the granular behavior are of importance for a better characterization of bedload transport granular flow structure. Accordingly, the results will be discussed and analyzed further in the next section.

5.3 Discussion

The persistence of the dense granular flow at high inertial number has been seen to depend on the parameters of the simulations. In order to obtain a better understanding, the position of the transition is studied as a function of the parameters of the problem (section 5.3.1). This is complemented by further analysis of the granular behavior above (section 5.3.2) and below (section 5.3.3) the transition.

5.3.1 Transition from dense to rapid granular flows

The inertial number at the transition denoted as I_{cr}, is determined for each run from the maximum of the shear to normal stress ratio. It corresponds exactly to the change in behavior observed in the solid volume fraction. Figure 5.15 shows the critical inertial number as a function of the modified Shields number defined in the

[3]It corresponds to an average one diameter interparticles distance, for which particles are not much interacting with each other.

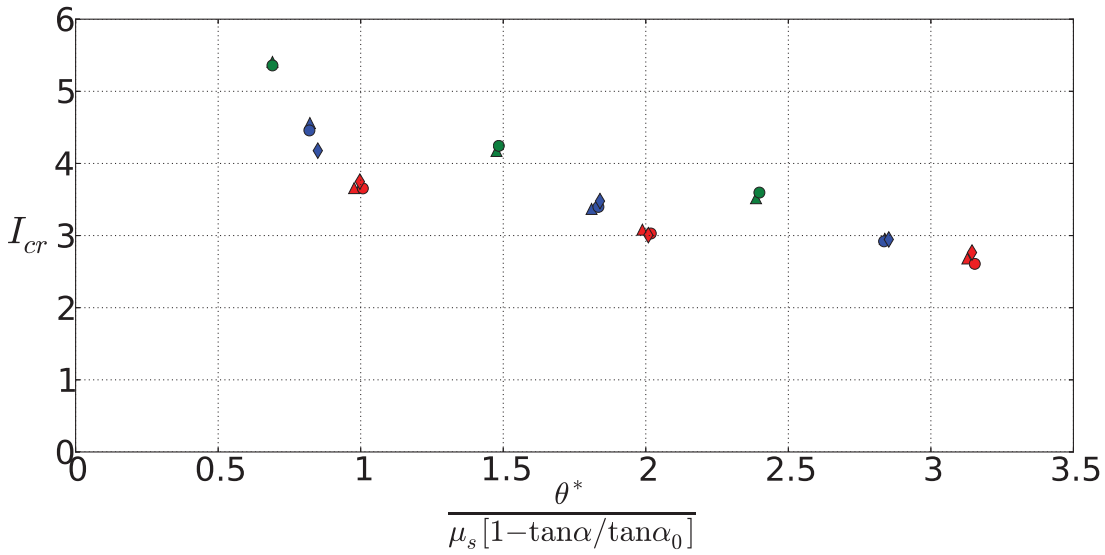

Figure 5.15: Critical inertial number I_{cr} for each run as a function of the modified Shields number to account for the effect of the slope and density. I_{cr} has been determined for each run from the maximum of the shear to normal stress ratio. The color of the points depends on the particles density: $\rho^p = 1750kg/m^3$ (red),$\rho^p = 2500kg/m^3$ (blue),$\rho^p = 4000kg/m^3$ (green). The symbol are representative of the particle diameter: $d = 3mm$ (▲), $d = 6mm$ (●), $d = 12mm$ (⧫).

previous chapter. The latter is characteristic of bedload transport independently of the slope and the specific density. The data follow a decreasing trend with increasing modified Shields number. As a consequence, the critical Shields number is expected to be lower at the transition with debris flow. This behavior is consistent with the lower value observed by *Börzsönyi et al.* (2009) at the transition from dense to dilute flows. Indeed, the closest configuration from the dry inclined plane is obtained at the transition to debris flow where the whole granular layer is entrained, and for which the modified Shields number tends to infinity. Therefore, the observed variation of the transition from dense to dilute granular flows suggests an influence of the configuration adopted on the transition. The fluid bed shear stress surface contribution allows to create a granular flow at inclination lower than the inclined plane, possibly stabilizing the dense flow.

5.3.2 High inertial number

Looking at very high inertial numbers ($I_{dry} > 10$), the solid volume fraction shows a common behavior for the different runs with increasing inertial number (see figure 5.16a). While not collapsing, they all exhibit a decrease of the solid volume fraction as a power-law I_{dry}^{-n} with an exponent $n \sim 1.75$. The very low solid volume fraction observed indicates that it is the signature of isolated particles behavior.
We have studied the classical dry inclined plane configuration locally, and it presents

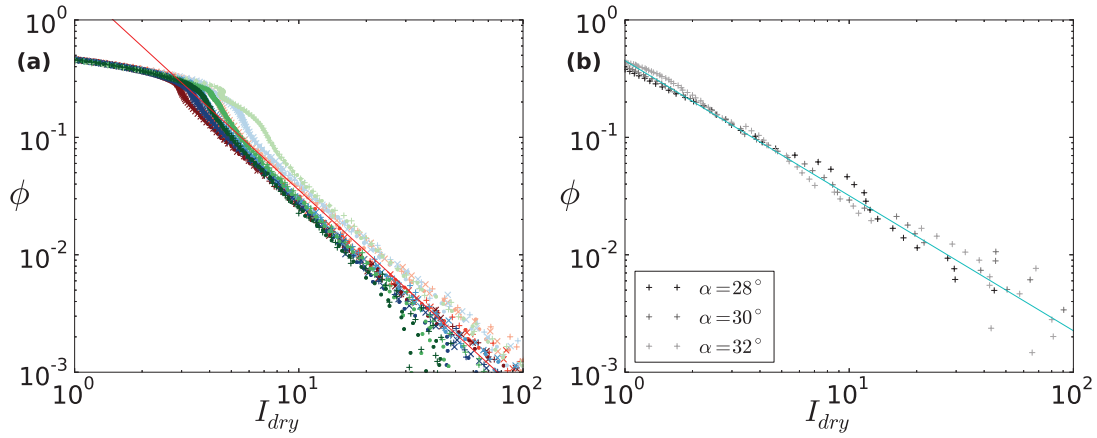

Figure 5.16: Solid volume fraction as a function of the dry inertial number in logarithmic scale, for bedload transport cases presented in table 5.1 (a), and dry inclined plane configuration with inclination angle α (b). The red and cyan curves represent respectively a trend I_{dry}^{-n} with $n = 1.75$ and $n = 1.15$.

a similar signature at the top of the sample. The setup adopted is the same as for the bedload configuration, without fluid forces. The inclination angle is increased, and the depth profiles are computed with the usual mesh ($l_z = d/30$). The configurations sampled (α = 28, 30, 32 degrees) are steady and uniform. Figure 5.16b shows that the solid volume fraction decreases as a power-law at very high inertial number. The exponent is slightly lower ($n = 1.15$) than in the bedload transport case ($n = 1.75$). This difference can be explained by the effect of the fluid flow in the latter case. Therefore, the power-law decrease can be seen as the signature of saltating particles having ballistic trajectories at the top of the granular layer. In this region, it is not relevant anymore to analyze the granular rheology since the solid volume fraction is very low. However, for numerical purpose, a solid volume fraction power-law decrease can be used as a boundary condition in the $\mu(I)$ rheology framework.

5.3.3 Nature of the dense granular flow layer

The dense granular regime observed up to high inertial numbers in bedload transport suggests a non-negligible collisional contribution. Indeed, the solid volume fraction collapses down to $\phi = 0.3$ (figure 5.7), where the particles do not, *a priori*, experience long-lasting contacts. To quantify the contribution of the collisions to the granular media effective friction, the effect of the restitution coefficient is considered. Figure 5.17 presents the effective friction and the solid volume fraction as a function of the dry inertial number, for three runs with different restitution coefficients. It shows weak differences when lowering the restitution coefficient from $e_n = 0.5$ to $e_n = 0.1$. However, the increase to $e_n = 0.9$ impacts importantly the rheology,

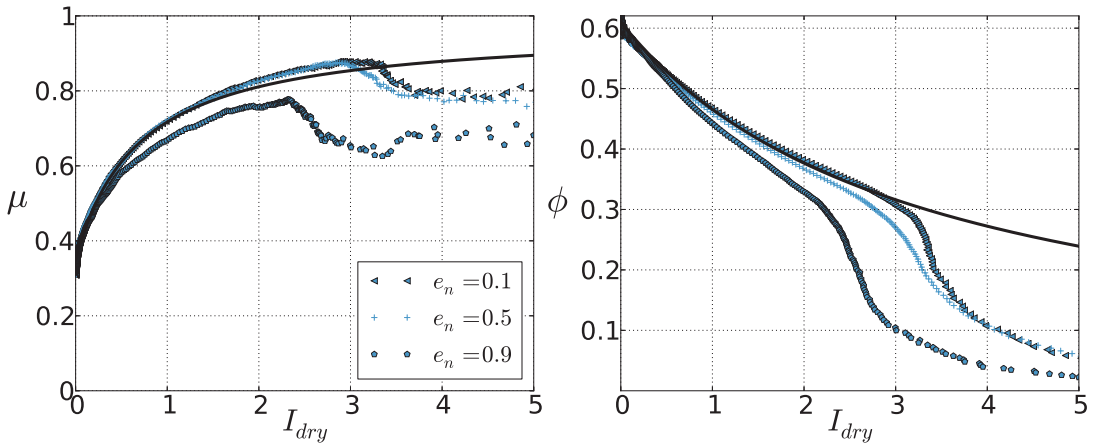

Figure 5.17: Effect of the restitution coefficient on shear to normal stress ratio and solid volume fraction, as a function of the inertial number, for case r2d6s2 (see table 5.1).

lowering the effective friction coefficient and the solid volume fraction for a given inertial number. It is consistent with the results of *Da Cruz et al.* (2005), at lower inertial number ($I_{dry} < 0.3$). This is the signature of collisional mechanisms: the reduction of the dissipation at contact induces an increase in granular temperature. The latter leads to a decompaction and a reduction of the stress ratio. The regime observed seems therefore to result from the co-existence of frictional and collisional behaviors. This tends to support models such as the one developed by *Armanini et al.* (2014), combining together the kinetic theory and the $\mu(I)$ rheology to describe intense bedload transport from the lowermost granular bed to the uppermost dilute granular flows.

5.4 Conclusion

The granular rheology in turbulent bedload transport has been characterized numerically over a wide range of Shields number, specific density and particle diameter. The local computation of the rheology has allowed to sample all the different granular regimes, from quasi-static to rapid granular flows. The results obtained allow one to draw a picture of the depth structure of turbulent bedload transport (figure 5.18).

In the lowermost layer, a creeping regime is observed, characterized by long period of rests and sudden re-arrangements. In this region, the average effective friction coefficient of the granular medium is below the static friction coefficient, denoting the presence of non-local effects. Above, a dense granular flow layer is observed, following the scaling of the $\mu(I)$ rheology in the free-fall regime. The layer subsists until unexpectedly high inertial number, and present the co-existence of frictional and collisional behaviors. A transition is observed at higher inertial number to a

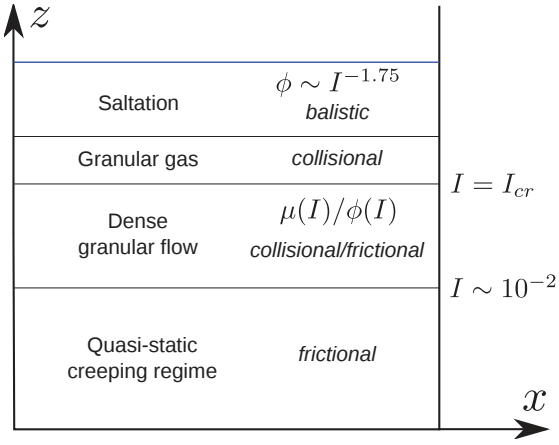

Figure 5.18: Schematic picture of the depth structure of granular behavior in bed-load transport.

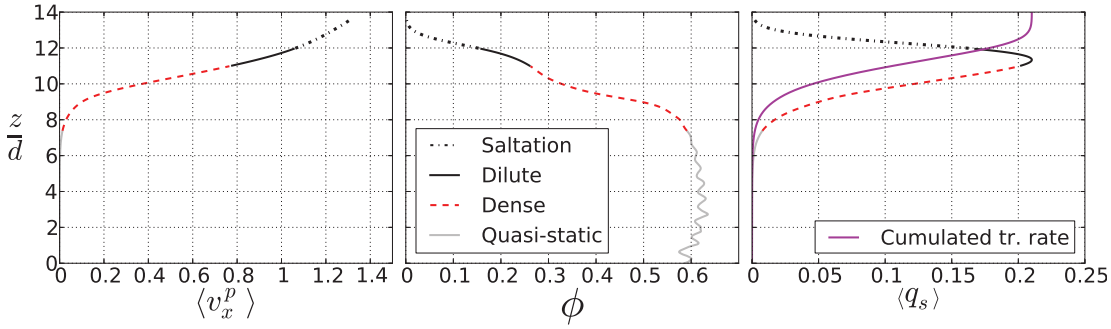

Figure 5.19: Estimation of the repartition of the different granular regimes in the solid depth profiles, for case r2d6s2 in table 5.1. For a better lisibility, the cumulated transport rate is normalized by $\int_0^h \langle q_s \rangle (z)dz / \langle q_s \rangle^{max}$.

dilute regime related to a granular gas, even though not well predicted by the kinetic theory. The transition is observed to depend on the configuration parameters and decrease with increasing modified Shields number. The uppermost layer can be assimilated as saltation trajectory on the top of the granular free-surface.

While the repartition of the transport rate contribution of the different layers has been seen to evolve as a function of the parameters, it is interesting to estimate it for a given case. Figure 5.19 shows that the transport rate is dominated by the dense granular flow, the dilute regime, and to a lesser extent the saltation part. This picture reaffirms the importance of the transition between the dense and dilute regime for the transport rate.

In addition, the present findings challenge the existing granular media rheologies. Indeed, the results have been observed to scale with the dry inertial number, in a range of parameters where a transition to the turbulent regime is expected in the framework of the extended $\mu(I)$ rheology. These results are supported by the

observations of *Izard* (2014), and question the existence of the turbulent regime for granular media. Moreover, dense granular flows have been observed up to high inertial numbers similarly to the experimental results of *Holyoake and McElwaine* (2012). The variation of the extent of the dense region with the parameters, and the importance of the collisional nature inside the dense layer, suggest that the studied configuration influences the transition from dense to dilute granular flows. These characteristics are not well described by the $\mu(I)$ rheology and the kinetic theory.

Chapter 6

Conclusions and perspectives

6.1 Conclusions

The present thesis has focused on the analysis of the granular phase behavior in idealized bedload transport configurations. The aim was to improve our understanding of turbulent bedload transport by studying a simplified configuration. Using numerical simulations of monodisperse spherical beads has enabled us to characterize the depth structure of the granular phase and identify underlying mechanisms in turbulent bedload transport.

A minimal numerical model has been proposed, coupling a discrete element method with a one-dimensional volume-averaged fluid momentum balance equation. Particular care has been taken to detail the coupling between the fluid and the granular phase. The lack of granular scale separation in bedload transport has been pointed out and its consequences identified in the fluid-particle interaction term. Omitting the scale separation between the weigthing function and the particle diameter, a formulation of the averaging has been proposed to ensure the independence of the results with the weighting function length scale. The numerical model has been compared with the classical sediment transport rate curve as a function of the Shields number, as well as with quasi-2D particle-scale measurements of solid volume fraction, solid velocity and transport rate density depth profiles. The good agreement obtained with experiments validates the approach and the developed model. A simple discrete random walk model has been proposed to account for the fluid velocity fluctuations. It has been shown to influence mainly the incipient motion Shields number.

The model has been further used to analyze the depth structure of the granular flow in bedload transport. Considering the effect of the friction coefficient, it has been shown to affect the transport rate through the solid velocity, while no variation of the solid volume fraction profile has been observed. Conversely, the restitution coefficient has been shown to have negliglible influence on the integrated transport

rate, but to affect the solid volume fraction and the transport rate density depth repartition. The decrease of the restitution coefficient induces a reduction of the mobile layer thickness, coupled with an increase of the solid velocity in the uppermost region. The results evidence the complex coupling between the granular and the fluid phase, and the impact of the contact parameters on the depth structure of the granular phase. The influences of both the friction and the restitution coefficient show the importance of both collisional and frictional granular characteristics in bedload transport.

To extend the analysis of the sediment transport rate, the slope angle and the specific density have been varied. It has been shown that the classical adimensionalization of the fluid bed shear stress and the sediment transport rate, does not allow to catch the evolution observed with variation of slope and specific density. Analyzing the depth profile of the shear to normal granular stress ratio in the framework of the two-phase volume-averaged equations, the effects of slope and specific density have been shown to be coupled. The importance of the fluid flow inside the granular bed has been identified as the missing link to understand the combined effect of both parameters. Rescaling the Shields number by the apparent friction coefficient of the granular phase, all the data have been shown to collapse on a master curve. The modified Shields number is characteristic of both the classical surface contribution of the fluid bed shear stress and the fluid contribution inside the granular bed. It allows to reproduce the divergence of the sediment transport rate at the transition to debris flows, and defines a characteristic vertical length scale of the problem. Regarding the link with the field observations, these results confirm the intuitive picture of the slope as a destabilizing effect of the granular phase in bedload transport. Therefore, it shows that the field observations are not due to a change in the process, but to a modification of the transport conditions in higher slope configurations (e.g. hydraulic conditions, grains-size distribution, grain shape).

The rheology of the granular phase as a function of the depth has been characterized for a wide range of Shields number, particle diameter and density ratio, in bedload transport conditions. Computing the local rheology has allowed to sample all the granular regimes from quasi-static to rapid granular flows. A picture of the granular regime can be drawn as a function of the depth. The lower quasi-static part exhibits signatures of a creeping regime and non-local effects. On the top of it, a dense granular flow layer is present with co-existence of frictional and collisional mechanisms. The dense granular flow persists up to unexpectedly high inertial numbers. The transition to dilute granular flow is controlled by the parameters of the simulations such as the Shields number and the density. The dilute regime shows the signature of a granular gas over a limited region, topped by a behavior assimilated to bedload transport saltation.

6.2 Perspectives

6.2.1 Granular media rheology

The results obtained challenge the existing granular media rheology. The non-zero velocity observed at shear to normal granular stress ratio under the static effective friction coefficient of the granular media is a typical signature of non-local effects. Recent development (e.g. *Kamrin and Koval* (2012); *Bouzid et al.* (2013)) extended the $\mu(I)$ rheology to account for such effects. Bedload transport represents a complex case of granular flows, and can be used to compare the results with the existing theories.

In the dilute part of the flow, the shear and normal stress components have been seen to collapse on a single curve when rescaled by the kinetic theory formulation. However, the trend followed by the two components as a function of the solid volume fraction are not in agreement with the predictions. It would be interesting to study the origin of the difference between the predictions and the results observed.

The dense granular flow has been shown to persist up to unusually high inertial numbers, in a regime characterized by a non-negligible contribution of the collisional granular behavior. The transition from dense to dilute granular flows has been observed to depend on the configuration, being linked with the Shields number and the apparent static friction coefficient of the granular material. While the relevance of such results might be questionned in a framework without granular scale separation, the experimental observations of *Holyoake and McElwaine* (2012) tend to support the results obtained. Further bedload transport simulations could be performed at higher Shields number, in order to reproduce the present results in a framework where the mobile layer thickness allows a larger averaging mesh and a better granular scale separation. If the observations are confirmed, the approach of both the dense granular flow and the transition to dilute flow should be reconsidered in the framework of the $\mu(I)$ rheology.

6.2.2 Transport rate scaling

To extend the scaling of the transport rate with modified Shields number, supplementary simulations with higher slopes and higher Shields number should be performed. In addition, it would be interesting to compile and/or perform experimental measurements, to test the scaling and bridge the gap with more realistic configurations. A combined experimental and numerical analysis would possibly enable us to identify the missing link between the field observations and the present results.

6.2.3 Numerical modelling

In the numerical model, the hydrodynamic forces applied to the particles have been restricted to drag and buoyancy. *Ji et al.* (2013) showed by means of DNS-DEM simulations, that the lift force can be of the same order of magnitude than the drag force close to the incipient motion. Up to now, no satifying formulations have been proposed to model the lift force in bedload transport (*Schmeeckle et al.*, 2007). Considering its importance close to the critical Shields number, experimental measurements or analysis from DNS-DEM simulation would be of interest to provide an empirical relationship valid for turbulent bedload transport. Regarding the closure law for the turbulent shear stress, the mixing length formulation adopted could benefit from recent experimental measurements. *Revil-Baudard et al.* (2015) showed that the effect of sediment transport on turbulence can be modelled as a modification of the Von Karman constant[1]. Based on their experimental results, a formulation can be proposed and compared with the experiments to provide a solid experimental basis for the closure law.

In the present work, it has been observed that the fluid resolution and the turbulent fluctuations model do not enable one to reproduce the right trend of the dimensionless transport rate close to the critical Shields number. In addition, regarding the transition to sheet flows, the influence of the turbulent structures has been shown to play major role (*Revil-Baudard et al.*, 2015). To extend the range of application of the model to these two regimes, the improvement of both the turbulent velocity fluctuations model and the fluid resolution should be considered. A first test for the fluctuations model would be to reproduce the Rouse suspension profile in intense sheet flow. The fluctuation model could be improved by considering a Langevin equation with space-time correlations of the fluctuations (*Dehbi*, 2008). For the fluid phase description, the present model can be seen as a basis to generalize the resolution to three dimensions, taking advantage from the convergence analysis performed and the averaging approach adopted in this PhD. A 3D fluid description would enable to tackle issues linked to bedforms for example.

The characterization of the granular rheology provides a description of the constitutive law for granular media, which can in two-phase volume-averaged continuous models. This allows to lower substantially the computational cost and describe larger scale problems. Preliminary comparisons have been performed with the Euler/Euler model of Julien Chauchat (*Revil-Baudard and Chauchat*, 2013; *Chauchat et al.*, 2015), which shares the same fluid resolution with a steady uniform continuous description of the granular phase using the $\mu(I)$ rheology as a closure law. Setting the parameters from the fit of the $\mu(I)$ rheology performed in chapter 5, a comparison with a case simulated during the PhD is shown in figure 6.1. In the dense granular layer the profiles match perfectly, while the dilute region is logically

[1] therefore called Von Karman parameter.

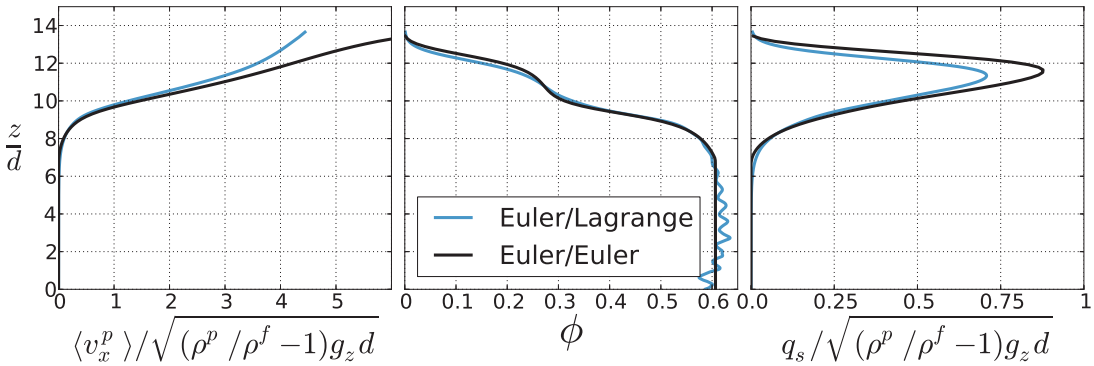

Figure 6.1: Solid depth profile comparison between Euler/Lagrange simulation performed during the PhD and Euler/Euler simulation from the code of Julien Chauchat (*Revil-Baudard and Chauchat*, 2013; *Chauchat et al.*, 2015). The latter uses the $\mu(I)$ rheology as closure law for the granular stress formulation, with the parameters obtained from the fit of the granular rheology in chapter 5: $\mu_1 = 0.35$, $\mu_2 = 0.97$, $I_0 = 0.69$, $\phi^{max} = 0.61$, $a = 0.31$ in eq. 5.9 and 5.11. Comparison for case r2d6s2 in table 5.1.

exhibiting some differences. Although the comparison remains to be extended to a wide range of parameters, the good overall agreement obtained suggests that using the $\mu(I)$ rheology with the fitted parameters is sufficient to describe the granular depth profiles at first order. It questions the importance of the dilute regime in bedload transport modelling, and opens perspectives for continuous two-phases models.

6.2.4 Vertical size-segregation in bedload transport

Grain size depth repartition is of primary importance for the prediction of the bedload transport rate (*Frey and Church*, 2011; *Bacchi et al.*, 2014). The coupling between size-segregation (*Andreotti et al.*, 2013), increasing mobility of fine particles (*Gilbert*, 1914; *Venditti et al.*, 2010), and hiding/exposure effects (*Houssais and Lajeunesse*, 2012), lead to complex behaviors that are not well-understood yet and represent a major scientific issue. In the framework of the PhD, the model developed has been adapted to simulate bi-disperse granular samples. The first year master project of *Morchid-Alaoui* (2015)[2] aimed at performing preliminary analysis of bi-disperse bedload transport simulations. The experimental observation of *Van der Vaart et al.* (2015) on the asymmetry of particle size-segregation in oscillatory simple shear, has been qualitatively reproduced in the framework of bedload transport. A fine particle is observed to fall down by steps in a coarse sample, at a segregation velocity much larger than a coarse particle at the bottom of a fine granular sample (see figure 6.2a and b). In addition, the infiltration of a given number of fine particles layers deposited at the top of a coarse sample has been studied (see an example

[2]supervised by Philippe Frey and the author

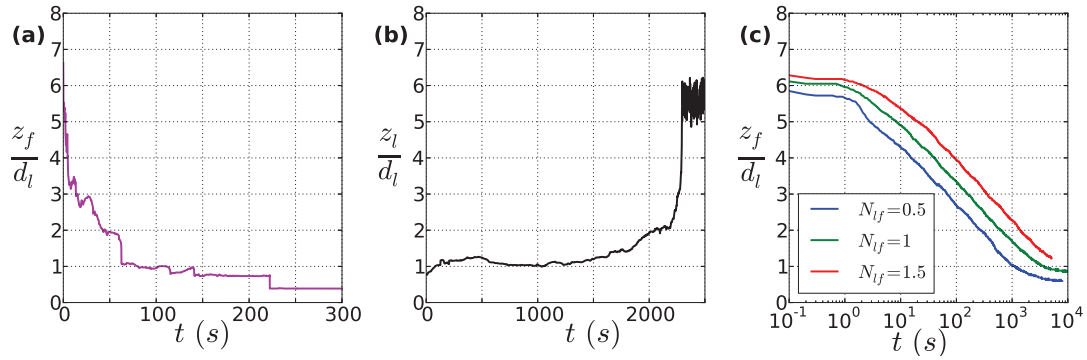

Figure 6.2: Vertical position of a test-particle center of mass as a function of time for three bi-disperse bedload transport configuration of Shields number $\theta^* \sim 0.1$. Figure (a) and (b) corresponds to respectively a single fine particle deposited at the top of a coarse granular sample, and a single coarse particle deposited at the bottom of a fine granular sample. Figure (c) corresponds to the evolution of the center of mass of N_{lf} fine particle layers deposited at the top of a coarse sample. The vertical position is normalized by the coarse particle diameter d_l.

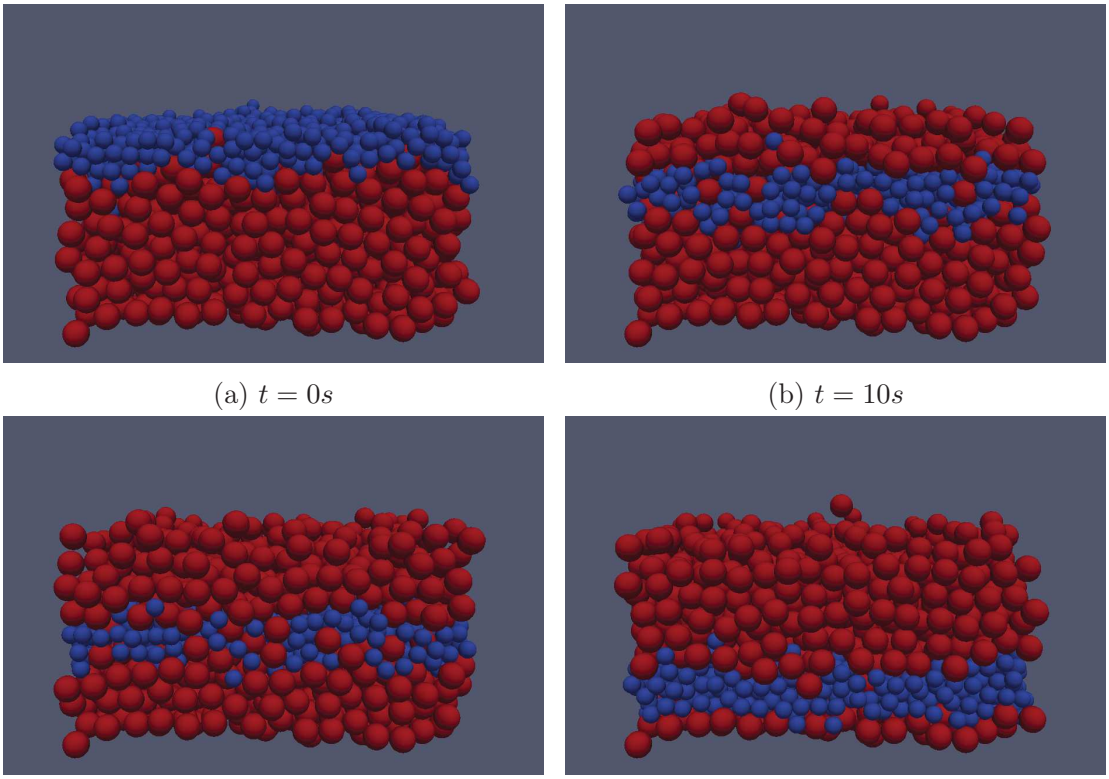

(a) $t = 0s$ (b) $t = 10s$

(c) $t = 50s$ (d) $t = 10000s$

Figure 6.3: Infiltration of a fine particle layer into a coarse sample as a function of time in bedload transport.

in figure 6.3). The center of mass of the fine particles has been shown to follow the same logarithmic decrease with time, for variation of initially deposited fine particle layers (see figure 6.2c). This common collective behavior has been shown to be driven by the shear rate depth profile. As can be deduced from dimensional analysis, the logarithmic exponent is directly linked with the exponential decrease of the shear rate (*Morchid-Alaoui*, 2015).

These promising results show the ability of the model to deal with granular size-segregation, and its potential to improve our understanding of the phenomenon in bedload transport. A comparison with the experimental data obtained in Irstea Grenoble during the last years (*Ripert*, 2011; *Hergault*, 2011; *Frey and Martin*, 2012; *Bel et al.*, 2013a,b) would be of particular interests, as well as the extension of the granular rheology analysis to the context of bi-disperse mixtures (*Yohannes and Hill*, 2010; *Tripathi and Khakhar*, 2011; *Hill and Yohannes*, 2011).

Chapter 7

Appendix

A Fluid phase equation derivation

The use of average two-phase flow equations in the framework of bedload transport violate the separation of scale between the characteristic size of the weighting function l and the particle diameter d. In order to clarify precisely the underlying assumptions made when using these equations without separation of scale, the averaged fluid equation are derived in the present appendix from the local formulation of Navier-Stokes equation. The derivation is performed considering only the hypotheses verified in the present case. It enables us to compare the equation obtained with the classical one, and identify the source of the assumptions made when using the latter outside of its validity domain. The equation derivation follows the paper of *Anderson and Jackson* (1967), without assuming separation of scales between l and d.

A.1 Averaging formulation and properties

To define volume averaging, the weighting function g should be positive, indefinitly derivable, and normalized over the whole space V, so that:

$$\int_V \mathcal{G}(\vec{y}) dV_y = 1. \tag{7.1}$$

Following this definition, the fluid volume fraction ϵ at a point $\vec{x}$ and time t is defined as:

$$\epsilon(\vec{x}, t) = \int_{V_f(t)} \mathcal{G}(\vec{x} - \vec{y}) dV_y, \tag{7.2}$$

where V_f is defined by the volume occupied by the fluid. For a point property of the fluid phase $\gamma(\vec{x},t)$, the local average value $\langle\gamma\rangle^f(\vec{x},t)$ is defined as:

$$\epsilon(\vec{x},t)\langle\gamma\rangle^f(\vec{x},t) = \int_{V_f(t)} \gamma(\vec{y},t)\mathcal{G}(\vec{x}-\vec{y})dV_y. \tag{7.3}$$

These three definitions together determine an averaging if the results are independent from the shape and the characteristic size of the weighting function, i.e. in the present case if the results converge with varying length scale associated with the weighting function. In bedload, this is observed only when decreasing the size of the wall-normal length scale. Consequently, this scale is imposed, and the analysis shows that this characteristic length should be lower than the particle diameter. Interestingly, the lack of scale separation in the granular phase still allows the derivation of the fluid phase equation.
As a direct consequence of the convergence of the results, the spatial variation of the local average variables are slow compared with the characteristic size of the weighting function. This can be written mathematically as:

$$\int_{V_f(t)} \langle\gamma\rangle^f(\vec{y},t)\mathcal{G}(\vec{x}-\vec{y})dV_y \approx \langle\gamma\rangle^f(\vec{x},t)\int_{V_f(t)} \mathcal{G}(\vec{x}-\vec{y})dV_y = \epsilon(\vec{x},t)\langle\gamma\rangle^f(\vec{x},t), \tag{7.4}$$

and is equivalent to the well-known property of the averaging:

$$\left\langle\langle\gamma\rangle^f\right\rangle^f = \langle\gamma\rangle^f. \tag{7.5}$$

Therefore, a point property can be decomposed as:

$$\gamma(\vec{x},t) = \langle\gamma\rangle^f(\vec{x},t) + \gamma'(\vec{x},t), \tag{7.6}$$

where the average of the point property fluctuation $\langle\gamma'(\vec{x},t)\rangle^f \approx 0$. From the definition of fluid averaging, the spatial and temporal derivative of the average can be evaluated. Deriving equation (7.3) with respect to x_j:

$$\begin{aligned}\frac{\partial}{\partial x_j}\left[\epsilon(\vec{x},t)\langle\gamma\rangle^f(\vec{x},t)\right] &= \frac{\partial}{\partial x_j}\left[\int_{V_f(t)}\gamma(\vec{y},t)\mathcal{G}(\vec{x}-\vec{y})dV_y\right] \\ &= \int_{V_f(t)}\mathcal{G}(\vec{x}-\vec{y})\frac{\partial\gamma(\vec{y},t)}{\partial y_j}dV_y + \int_{V_f(t)}\frac{\partial\mathcal{G}(\vec{x}-\vec{y})}{\partial y_j}\gamma(\vec{y},t)dV_y. \end{aligned}\tag{7.7}$$

Using on the last term Gauss theorem, and the fact that:

$$\frac{\partial}{\partial x_j}\mathcal{G}(\vec{x}-\vec{y}) = -\frac{\partial}{\partial y_j}\mathcal{G}(\vec{x}-\vec{y}), \tag{7.8}$$

we obtain:

$$\frac{\partial}{\partial x_j}\left[\epsilon(\vec{x},t)\left\langle\gamma\right\rangle^f(\vec{x},t)\right] = \int_{V_f(t)}\mathcal{G}(\vec{x}-\vec{y})\frac{\partial\gamma(\vec{y},t)}{\partial y_j}dV_y - \int_{S_f(t)}\mathcal{G}(\vec{x}-\vec{y})\gamma(\vec{y},t)n'_j dV_y, \tag{7.9}$$

where n'_j is the normal to the fluid limiting surface. The surface bounding the fluid phase $S_f(t)$ is made of the contour of the whole system $S_{f\infty}(t)$ plus the interface with the particles. Considering that for most positions in space, the distance to the contour is much bigger than the characteristic size of the weighting function, this term can be neglected. The last term of equation (7.10) can then be rewritten:

$$\begin{aligned}\int_{S_f(t)}\mathcal{G}(\vec{x}-\vec{y})\gamma(\vec{y},t)n'_j dV_y &= \sum_{p\infty}\int_{s_p(t)}\mathcal{G}(\vec{x}-\vec{y})\gamma(\vec{y},t)n'_j dS_y \\ &= -\sum_{p\infty}\int_{s_p(t)}\mathcal{G}(\vec{x}-\vec{y})\gamma(\vec{y},t)n_j dS_y,\end{aligned} \tag{7.10}$$

where the sum $\sum_{p\infty}$ is over all the particles in the system, the integral over the particle surface $s_p(t)$, and n_j is the normal to the fluid at the interface, while $n_j = -n'_j$ is the normal to the particle at the interface. These, together, modify equation (7.10) and gives the important equation:

$$\int_{V_f(t)}\mathcal{G}(\vec{x}-\vec{y})\frac{\partial\gamma(\vec{y},t)}{\partial y_j}dV_y = \frac{\partial}{\partial x_j}\left[\epsilon(\vec{x},t)\left\langle\gamma\right\rangle^f(\vec{x},t)\right] - \sum_{p\infty}\int_{s_p(t)}\mathcal{G}(\vec{x}-\vec{y})\gamma(\vec{y},t)n_j dS_y. \tag{7.11}$$

A similar approach can be applied for the time-derivative taking into account in addition the variation of the V_f with time. It leads to a second important equation:

$$\int_{V_f(t)}\mathcal{G}(\vec{x}-\vec{y})\frac{\partial\gamma(\vec{y},t)}{\partial t}dV_y = \frac{\partial}{\partial t}\left[\epsilon(\vec{x},t)\left\langle\gamma\right\rangle^f(\vec{x},t)\right] + \sum_{p\infty}\int_{s_p(t)}\mathcal{G}(\vec{x}-\vec{y})\gamma(\vec{y},t)v_j n_j dS_y, \tag{7.12}$$

where v_j is the particle velocity j component. The last two equations will be used intensively in the derivation. Until here, all the assumptions made are consistent with bedload situations with strong wall-normal gradient. Using the properties defined by equation (7.2), (7.3), (7.4), (7.5), (7.6), (7.11) and (7.12), the average momentum balance equation of the fluid phase in a two-phase flow is derived.

A.2 Continuity equation

First, the local continuity equation for an incompressible fluid is given by:

$$\frac{\partial u_i(\vec{x},t)}{\partial x_i} = 0, \tag{7.13}$$

where u_i is the i-th component of the local point fluid velocity. Multiplying by $\mathcal{G}(\vec{x}-\vec{y})$ and integrating over the fluid volume, it reads:

$$\int_{V_f(t)} \mathcal{G}(\vec{x}-\vec{y}) \frac{\partial u_i(\vec{y},t)}{\partial x_i} dV_y = 0. \tag{7.14}$$

Using equation (7.11), it gives:

$$\frac{\partial}{\partial x_i}\left[\epsilon(\vec{y},t)\left\langle u_i\right\rangle^f(\vec{y},t)\right] - \sum_{p\infty}\int_{s_p(t)} \mathcal{G}(\vec{x}-\vec{y}) u_i(\vec{y},t) n_i' dS_y. = 0. \tag{7.15}$$

With $\gamma = 1$ in equation (7.12), and using the property of fluid and particle velocity equality at their interface, the following is obtained:

$$0 = \frac{\partial}{\partial t}\epsilon(\vec{x},t) + \sum_{p\infty}\int_{s_p(t)} \mathcal{G}(\vec{x}-\vec{y}) u_i(\vec{y},t) n_i' dS_y, \tag{7.16}$$

and the continuity equation can be expressed classically from eq. 7.15:

$$\frac{\partial}{\partial t}\epsilon(\vec{x},t) + \frac{\partial}{\partial x_i}\left[\epsilon(\vec{x},t)\left\langle u_i\right\rangle^f(\vec{x},t)\right] = 0. \tag{7.17}$$

A.3 Fluid phase equation

For the momentum balance, the starting point is the local incompressible Navier-Stokes equations:

$$\rho^f\left[\frac{\partial u_i}{\partial t} + \frac{\partial}{\partial x_i}(u_i u_j)\right] = \frac{\partial \sigma_{ij}}{\partial x_i} + \rho^f g_i, \tag{7.18}$$

where ρ^f is the fluid density, σ_{ij} is the fluid stress tensor local value, g_i is the i-th component of the gravity vector. Like for the continuity equation, by multiplying by $\mathcal{G}(\vec{x}-\vec{y})$ and integrating over the fluid phase:

$$\rho^f\int_{V_f(t)} \mathcal{G}(\vec{x}-\vec{y})\left[\frac{\partial u_i}{\partial t} + \frac{\partial}{\partial y_i}(u_i u_j)\right] dV_y = \int_{V_f(t)} \mathcal{G}(\vec{x}-\vec{y})\frac{\partial \sigma_{ij}}{\partial y_i} dV_y + \int_{V_f(t)} \mathcal{G}(\vec{x}-\vec{y})\rho^f g_i dV_y. \tag{7.19}$$

In the last term on the right hand side, apart from the weighting function there are no dependency in space under the integral, and it simplifies to $\rho^f g_i \epsilon(\vec{x},t)$ using the definition of the fluid volume fraction (eq. 7.2). Considering the full left hand side term, writing equation (7.12) with $\gamma = u_i$ gives:

$$\int_{V_f(t)} \mathcal{G}(\vec{x}-\vec{y})\frac{\partial u_i(\vec{y},t)}{\partial t} dV_y = \frac{\partial}{\partial t}\left[\epsilon(\vec{x},t)\left\langle u_i\right\rangle^f(\vec{x},t)\right] + \sum_{p\infty}\int_{s_p(t)} \mathcal{G}(\vec{x}-\vec{y}) u_i(\vec{y},t) u_j(\vec{y},t) n_j dS_y, \tag{7.20}$$

where we used the fact that the fluid and particle velocities are equal at the surface of the particles in the last term. Similarly, putting $\gamma = u_i u_j$ in equation (7.11), we

obtain:

$$\int_{V_f(t)} \mathcal{G}(\vec{x}-\vec{y})\frac{\partial}{\partial y_j}\left(u_i(\vec{y},t)u_j(\vec{y},t)\right)dV_y = \frac{\partial}{\partial x_j}\left[\epsilon(\vec{x},t)\left\langle u_i u_j\right\rangle^f(\vec{x},t)\right] - \sum_{p\infty}\int_{s_p(t)} \mathcal{G}(\vec{x}-\vec{y})u_i(\vec{y},t)u_j(\vec{y},t)n_j dS_y. \quad (7.21)$$

The term $\langle u_i u_j\rangle^f$ is rewritten, taking into account the known property 7.5 and 7.6:

$$\langle u_i u_j\rangle^f = \left\langle (\langle u_i\rangle^f + u_i')(\langle u_j\rangle^f + u_j')\right\rangle^f = \left\langle \langle u_i\rangle^f \langle u_j\rangle^f + \langle u_i\rangle^f u_j' + u_i'\langle u_j\rangle^f + u_i'u_j'\right\rangle^f = \langle u_i\rangle^f\langle u_j\rangle^f + \left\langle u_i'u_j'\right\rangle^f. \quad (7.22)$$

Defining the Reynolds stress tensor as:

$$R_{ij}^f = \rho^f \epsilon \left\langle u_i'u_j'\right\rangle^f, \quad (7.23)$$

and using the equations 7.20, 7.21, and the continuity equation (eq. 7.17), the left hand side of equation (7.19) is simplified into:

$$\rho^f \int_{V_f(t)} \mathcal{G}(\vec{x}-\vec{y})\left[\frac{\partial u_i}{\partial t} + \frac{\partial}{\partial y_i}(u_i u_j)\right]dV_y = \rho^f\epsilon\left[\frac{\partial\langle u_i\rangle^f}{\partial t} + \langle u_j\rangle^f\frac{\partial\langle u_i\rangle^f}{\partial x_j}\right] + \frac{\partial R_{ij}^f}{\partial x_j}. \quad (7.24)$$

Lastly, the first term on the right hand side of equation (7.19) representing the integration of the fluid stress tensor is expressed with equation (7.11), and lead to the final formulation of the fluid equation:

$$\rho^f\epsilon\left[\frac{\partial\langle u_i\rangle^f}{\partial t} + \langle u_j\rangle^f\frac{\partial\langle u_i\rangle^f}{\partial x_j}\right] = \frac{\partial(\epsilon\langle\sigma_{ij}\rangle^f)}{\partial x_j} - \frac{\partial R_{ij}^f}{\partial x_j} + \rho^f\epsilon g_i - \sum_{p\infty}\int_{s_p(t)}\mathcal{G}(\vec{x}-\vec{y})\sigma_{ij}(\vec{y},t)n_j dS_y. \quad (7.25)$$

A.4 Link with classical formulation

As expressed in the body of the manuscript (section 2.2.1), this formulation is different from the classical one (eq. 2.8) in the formulation of the fluid-interaction term, represented by the last term on the right hand side of equation (7.25). When assuming separation of scales between the weighting function and the particle diameter, the weigthing function in the latter term can be expanded as a Taylor series about

the center of the particle (*Jackson*, 1997):

$$\mathcal{G}(\vec{x}-\vec{y}) = \mathcal{G}(\vec{x}-\vec{x^p}) - \frac{\partial \mathcal{G}(\vec{x}-\vec{x^p})}{\partial x_j}(y_j - x_j^p) + \frac{1}{2}\frac{\partial \mathcal{G}(\vec{x}-\vec{x^p})}{\partial x_j \partial x_k}(y_j - x_j^p)(y_k - x_k^p) - ... \quad (7.26)$$

Considering that on the surface of the particle $\vec{y} - \vec{x^p} = d\ \vec{n}(\vec{y})$ with d the particle diameter, it becomes:

$$\mathcal{G}(\vec{x}-\vec{y}) = \mathcal{G}(\vec{x}-\vec{x^p}) - d\frac{\partial \mathcal{G}(\vec{x}-\vec{x^p})}{\partial x_j} n_j(\vec{y}) + \frac{d^2}{2}\frac{\partial \mathcal{G}(\vec{x}-\vec{x^p})}{\partial x_j \partial x_k} n_j(\vec{y}) n_k(\vec{y}) - ... \quad (7.27)$$

Using this, the last term in the general fluid-particle interaction term, we can write following the notation of Jackson:

$$\sum_{p\infty} \int_{s_p(t)} \mathcal{G}(\vec{x}-\vec{y})\sigma_{ij}(\vec{y},t) n_j dS_y = n \left\langle f_{f\,i}^p \right\rangle^p (\vec{x}) - \frac{\partial}{\partial x_j}\left[n \left\langle s_{ij}^f \right\rangle^p (\vec{x}) \right] + \frac{1}{2}\frac{\partial^2}{\partial x_j \partial x_k}\left[n \left\langle s_{ijk}^f \right\rangle^p (\vec{x}) \right] - ... \quad (7.28)$$

where

$$n \left\langle f_{f\,i}^p \right\rangle^p (\vec{x}) = \sum_{p\infty} \mathcal{G}(\vec{x}-\vec{x^p}) \int_{s_p} \sigma_{im} n_m ds \quad (7.29)$$

$$n \left\langle s_{ij}^f \right\rangle^p (\vec{x}) = d \sum_{p\infty} \mathcal{G}(\vec{x}-\vec{x^p}) \int_{s_p} \sigma_{im} n_m n_j ds \quad (7.30)$$

$$n \left\langle s_{ijk}^f \right\rangle^p (\vec{x}) = d \sum_{p\infty} \mathcal{G}(\vec{x}-\vec{x^p}) \int_{s_p} \sigma_{im} n_m n_j n_k ds \quad (7.31)$$

with $\sigma_{im} n_m$ the traction force exerted by the fluid on the surface of the particle. Using separation of scale by considering that the derivative with respect of x is of the order the macroscopic length scale L, this series can be truncated at second order. The last two terms of equation (7.28) can be assimilated to second order particle-fluid phase interaction, and have been showed to lead to Einstein's effective viscosity in the fluid stress tensor for the case of dilute Stokesian particles (*Jackson*, 1997). Inserting this two terms in the effective fluid stress tensor, we recover the classical equation (2.8) as expected.

Bibliography

Amoudry, L. O. (2014), Extension of turbulence closure to two-phase sediment transport modelling: Application to oscillatory sheet flows, *Advances in Water Resources*, *72*, 110 – 121. 5

Ancey, C., P. Coussot, and P. Evesque (1999), A theoretical framework for granular suspensions in a steady simple shear flow, *Journal of Rheology*, *43*(6), 1673–1699. 9

Anderson, T. B., and R. Jackson (1967), Fluid mechanical description of fluidized beds. equations of motion, *Industrial & Engineering Chemistry Fundamentals*, *6*(4), 527–539. 5, 19, 25, 109

Andreotti, B., Y. Forterre, and O. Pouliquen (2013), *Granular media: between fluid and solid*, Cambridge University Press. ix, 3, 8, 69, 78, 89, 105

Armanini, A., H. Capart, L. Fraccarollo, and M. Larcher (2005), Rheological stratification in experimental free-surface flows of granular-liquid mixtures, *Journal of Fluid Mechanics*, *532*, 269–319. 13, 56

Armanini, A., M. Larcher, E. Nucci, and M. Dumbser (2014), Submerged granular channel flows driven by gravity, *Advances in Water Resources*, *63*, 1 – 10. 13, 97

Aussillous, P., J. Chauchat, M. Pailha, M. Médale, and E. Guazzelli (2013), Investigation of the mobile granular layer in bedload transport by laminar shearing flows, *Journal of Fluid Mechanics*, *736*, 594–615. 6, 10, 12, 31, 92

Bacchi, V., A. Recking, N. Eckert, P. Frey, G. Piton, and M. Naaim (2014), The effects of kinetic sorting on sediment mobility on steep slopes, *Earth Surface Processes and Landforms*, *39*(8), 1075–1086. 105

Bathe, K.-J., and E. Wilson (1976), *Numerical methods in finite element analysis*, Prentice-Hall (Englewood Cliffs, N.J.). 18

Bathurst, J. (2007), Effect of coarse surface layer on bed-load transport, *Journal of Hydraulic Engineering*, *133*(11), 1192–1205. 1, 3

Bel, C., K. Rorsman, and P. Frey (2013a), Size-segregation in bedload transport: Experiments and binary continuous modelling, in *Two-pHase modElling for Sed-Iment dynamIcS*. 107

Bel, C., K. Rorsman, and P. Frey (2013b), Size-segregation in bedload transport: Experiments at the particle scale and continuous modelling, in *EGU GA*, vol. 15, Vienna, Austria. 107

Berzi, D., and J. T. Jenkins (2008), A theoretical analysis of free-surface flows of saturated granular-liquid mixtures, *Journal of Fluid Mechanics*, *608*, 393–410. 13

Bigillon, F. (2001), Etude du mouvement bidimensionnel d'une particule dans un courant d'eau sur forte pente, Ph.D. thesis, Université Joseph Fourier. 13, 32, 35

Böhm, T. (2005), Motion and interaction of a set of particles in a supercritical flow, Ph.D. thesis, University Joseph Fourier Grenoble. 13, 32

Böhm, T., P. Frey, C. Ducottet, C. Ancey, M. Jodeau, and J. Reboud (2006), Two-dimensional motion of a set of particles in a free surface flow with image processing, *Experiments in Fluids*, *41*(1), 1–11. x, 32, 34

Börzsönyi, T., R. E. Ecke, and J. N. McElwaine (2009), Patterns in flowing sand: Understanding the physics of granular flow, *Phys. Rev. Lett.*, *103*, 178,302. 91, 92, 95

Bouzid, M., M. Trulsson, P. Claudin, E. Clément, and B. Andreotti (2013), Nonlocal rheology of granular flows across yield conditions, *Phys. Rev. Lett.*, *111*, 238,301. 10, 89, 103

Boyer, F., E. Guazzelli, and O. Pouliquen (2011), Unifying suspension and granular rheology, *Phys. Rev. Lett.*, *107*, 188,301. 12, 92

Brodu, N., J. A. Dijksman, and R. P. Behringer (2015), Multiple-contact discrete-element model for simulating dense granular media, *Phys. Rev. E*, *91*, 032,201. 16

Brogliato, B. (1999), *Non-smooth mechanics*, Springer. 15

Buffington, J., and D. Montgomery (1997), A systematic analysis of eight decades of incipient motion studies, with special reference to gravel-bedded rivers, *Water Resources Research*, *33*(8), 1993–2029. 54, 55

Calantoni, J., and C. S. Thaxton (2008), Simple power law for transport ratio with bimodal distributions of coarse sediments under waves, *Journal of Geophysical Research: Oceans*, *113*(C3), c03003. 5, 16

Campbell, C. (2002), Granular shear flows at the elastic limit, *Journal of Fluid Mechanics*, *465*, 261–291. 36

Campbell, C. S. (1990), Rapid granular flows, *Annual Review of Fluid Mechanics*, *22*(1), 57–90. 8, 93

Capart, H., and L. Fraccarollo (2011), Transport layer structure in intense bed-load, *Geophysical Research Letters*, *38*(20), l20402. 12, 57

Cassar, C., M. Nicolas, and O. Pouliquen (2005), Submarine granular flows down inclined planes, *Physics of Fluids (1994-present)*, *17*(10), 103301. 10, 11, 86, 87

Catalano, E. (2012), A pore-scale coupled hydromechanical model for biphasic granular media. application to granular sediment hydrodynamics, Ph.D. thesis, Université de Grenoble. 18, 19

Catalano, E., B. Chareyre, and E. Barthélémy (2014), Pore-scale modeling of fluid-particles interaction and emerging poromechanical effects, *Int. Journal for Numerical and Analytical Methods in Geomechanics*, *38*(1), 51–71. 18

Chareyre, B., and P. Villard (2005), Dynamic spar elements and discrete element methods in two dimensions for the modeling of soil-inclusion problems, *Journal of engineering mechanics*, *131*, 689. 18

Chauchat, J., S. Guillou, D. Pham Van Bang, and K. Dan Nguyen (2013), Modelling sedimentation-consolidation in the framework of a one-dimensional two-phase flow model, *Journal of Hydraulic Research*, *51*(3), 293–305. 29

Chauchat, J., T. Revil-Baudard, and D. Hurther (2015), An improved two-phase flow model for steady uniform sheet-flow based on dense granular flow rheology, in *36th IAHR world Congress*, The Hague, The Netherlands. xv, 29, 104, 105

Chiodi, F., P. Claudin, and B. Andreotti (2014), A two-phase flow model of sediment transport: transition from bedload to suspended load, *Journal of Fluid Mechanics*, *755*, 561–581. 12

Cortet, P.-P., D. Bonamy, F. Daviaud, O. Dauchot, B. Dubrulle, and M. Renouf (2009), Relevance of visco-plastic theory in a multi-directional inhomogeneous granular flow, *EPL (Europhysics Letters)*, *88*(1), 14,001. 10

Courrech du Pont, S., P. Gondret, B. Perrin, and M. Rabaud (2003), Granular avalanches in fluids, *Phys. Rev. Lett.*, *90*, 044,301. 10, 11, 86, 87, 88

Cowen, E. A., R. D. Dudley, Q. Liao, E. A. Variano, and P. L.-F. Liu (2010), An insitu borescopic quantitative imaging profiler for the measurement of high concentration sediment velocity, *Experiments in Fluids*, *49*(1), 77–88. 12

Cundall, P. A., and O. D. L. Strack (1979), A discrete numerical model for granular assemblies, *Géotechnique*, pp. 305–329(24). 4, 15

Da Cruz, F., S. Emam, M. Prochnow, J.-N. Roux, and F. Chevoir (2005), Rheophysics of dense granular materials: Discrete simulation of plane shear flows, *Phys. Rev. E*, *72*, 021,309. ix, 8, 9, 17, 18, 52, 56, 90, 97

DallaValle, J. M. (1948), *Micrometrics : The technology of fine particles*, vol. 2nd edition, Pitman Pub. Corp. 5, 25, 26

Dehbi, A. (2008), Turbulent particle dispersion in arbitrary wall-bounded geometries: A coupled cfd-langevin-equation based approach, *International Journal of Multiphase Flow*, *34*(9), 819 – 828. 27, 104

Doppler, D., P. Gondret, T. Loiseleux, S. Meyer, and M. Rabaud (2007), Relaxation dynamics of water-immersed granular avalanches, *Journal of Fluid Mechanics*, *577*, 161–181. 11

Drake, T. G., and J. Calantoni (2001), Discrete particle model for sheet flow sediment transport in the nearshore, *J. Geophys. Res.*, *106*(C9), 19,859–19,868. 6, 17, 55

Drew, D. A., and S. L. Passman (1999), *Theory of Multicomponent Fluids*, Springer. 5

Duran, O., B. Andreotti, and P. Claudin (2012), Numerical simulation of turbulent sediment transport, from bed load to saltation, *Physics of Fluids*, *24*(10), 103306. 5, 6, 17, 52, 61

Dwivedi, A., B. Melville, A. Raudkivi, A. Shamseldin, and Y. Chiew (2012), Role of turbulence and particle exposure on entrainment of large spherical particles in flows with low relative submergence, *Journal of Hydraulic Engineering*, *138*(12), 1022–1030. 55

Einstein, A. (1906), Eine neue Bestimmung der Molekül Dimensionen, *Ann. Physik*, *19*, 289–306. 22

Einstein, H. (1942), Formulas for the transport of bed sediment, *Transactions of the American Society of Civil Engineers*, *107*, 561–574. 2

Ergun, S. (1952), Fluid flow through packed columns, *Chemical Engineering Progress*, *48*(2), 89–94. 5, 25, 44

Faug, T., P. Childs, E. Wyburn, and I. Einav (2015), Standing jumps in shallow granular flows down smooth inclines, *Physics of Fluids*, *27*(7), 073304. 91

Fernandez Luque, R., and R. Van Beek (1976), Erosion and transport of bed-load sediment, *Journal of Hydraulic Research*, *14*(2), 127–144. 75

Finn, J., S. Apte, and M. Li (2014a), Numerical simulation of sand ripple evolution in oscillatory boundary layers, in *Proceedings of ASME Fluids Engineering Summer Meeting*. 5

Finn, J., M. Li, and S. Apte (2014b), Euler-lagrange simulations of sediment transport in oscillatory boundary layers with bedforms, *Coastal Engineering Proceedings*, *1*(34), 80. 5

Forterre, Y., and O. Pouliquen (2008), Flows of dense granular media, *Annual Review of Fluid Mechanics*, *40*(1), 1–24. ix, xiv, 7, 8, 9, 10, 90, 92, 93

Fredsøe, J., and R. Deigaard (1992), *Mechanics of Coastal Sediment Transport*, World. Scientific. 62, 75

Frey, P. (2014), Particle velocity and concentration profiles in bedload experiments on a steep slope, *Earth Surface Processes and Landforms*, *39*(5), 646–655. x, 13, 31, 32, 33, 34, 40, 42, 90

Frey, P., and M. Church (2009), How river beds move, *Science*, *325*, 1509–1510. 3

Frey, P., and M. Church (2011), Bedload : a granular phenomenon, *Earth Surface Processes and Landform*, *36*, 58–69. 3, 105

Frey, P., and T. Martin (2012), Experimental bedload sorting at the particle scale on steep slopes, in *River Flow*, edited by Murillo, pp. 393–397, Costa Rica. 107

Frey, P., and J. Reboud (2001), Experimental study of narrow free-surface turbulent flows on steep slopes, in *Advances in flow modeling and turbulence measurements*, edited by T. N. Ninokata H, Wada A, pp. 396–403, World Scientific Publishing Co., Tokyo. 36

Fukuoka, S., T. Fukuda, and T. Uchida (2014), Effects of sizes and shapes of gravel particles on sediment transports and bed variations in a numerical movable-bed channel, *Advances in Water Resources*, *72*, 84 – 96. 16

Garzó, V., and J. W. Dufty (1999), Dense fluid transport for inelastic hard spheres, *Phys. Rev. E*, *59*, 5895–5911. xiv, 8, 93, 94

Gilbert, K. G. (1914), *The transportation of débris by running water*, Washinton government printing office. 1, 105

Goldhirsch, I. (2003), Rapid granular flows, *Annual Review of Fluid Mechanics*, *35*(1), 267–293. 8, 93

Goldhirsch, I. (2010), Stress, stress asymmetry and couple stress: from discrete particles to continuous fields, *Granular Matter*, *12*(3), 239–252. 78, 79

Gondret, P., M. Lance, and L. Petit (2002), Bouncing motion of spherical particles in fluids, *Physics of Fluids*, *14*(2), 643–652. 18, 62

Graf, W., and S. Altinakar (1998), *Fluvial hydraulics: flow and transport processes in channels of simple geometry*. 36

Hanes, D. M., and A. J. Bowen (1985), A granular-fluid model for steady intense bed-load transport, *Journal of Geophysical Research: Oceans*, *90*(C5), 9149–9158. 6

Hergault, V. (2011), étude microstructurelle du transport par charriage de mélanges bidisperses à forte pente, Ph.D. thesis, University of Grenoble. 13, 32, 107

Hergault, V., P. Frey, F. Métivier, C. Barat, C. Ducottet, T. Böhm, and C. Ancey (2010), Image processing for the study of bedload transport of two-size spherical particles in a supercritical flow, *Experiments in Fluids*, *49*(5), 1095–1107. x, 34

Hill, K., and D. Tan (2014), Segregation in dense sheared flows: gravity, temperature gradients, and stress partitioning, *Journal of Fluid Mechanics*, *756*, 54–88. 16

Hill, K. M., and B. Yohannes (2011), Rheology of dense granular mixtures: Boundary pressures, *Phys. Rev. Lett.*, *106*, 058,302. 107

Hill, K. M., G. Gioia, and V. V. Tota (2003), Structure and kinematics in dense free-surface granular flow, *Phys. Rev. Lett.*, *91*, 064,302. 24, 38

Holyoake, A., and J. N. McElwaine (2012), High-speed granular chute flows, *Journal of Fluid Mechanics*, *710*, 35–71. 90, 91, 99, 103

Houssais, M., and E. Lajeunesse (2012), Bedload transport of a bimodal sediment bed, *Journal of Geophysical Research: Earth Surface*, *117*(F4), f04015. 105

Houssais, M., C. P. Ortiz, D. J. Durian, and D. J. Jerolmack (2015), Onset of sediment transport is a continuous transition driven by fluid shear and granular creep, *Nature communications*, *6*. 90

Hsu, T. J., J. T. Jenkins, and P. L. F. Liu (2004), On two-phase sediment transport: sheet flow of massive particles, *Proceedings of the Royal Society of London Series A-mathematical Physical and Engineering Sciences*, *460*(2048), 2223–2250. 5, 6, 12, 27, 57, 83

Izard, E. (2014), Modélisation numérique des écoulements granulaires denses immergés dans un fluide, Ph.D. thesis, Université de Toulouse. 87, 99

Izard, E., T. Bonometti, and L. Lacaze (2014), Simulation of an avalanche in a fluid with a soft-sphere/immersed boundary method including a lubrication force, *The Journal of Computational Multiphase Flows*, *6*(4), 391–406. 11, 17, 52

Jackson, R. (1997), Locally averaged equations of motion for a mixture of identical spherical particles and a newtonian fluid, *Chemical Engineering Science*, *52*(15), 2457 – 2469. 19, 21, 22, 24, 25, 114

Jackson, R. (2000), *The dynamics of fluidized particles*, Cambridge University Press. 5, 19, 20, 26, 79

Jean, M., and J. Moreau (1992), Unilaterality and dry friction in the dynamics of rigid body collections, in *Proceedings of Contact Mechanics International Symposium. Lausanne, Switzerland.*, pp. 31–48, Presses Polytechniques et Universitaires Romandes. 15

Jenkins, J., and D. Hanes (1998), Collisional sheet flows of sediment driven by a turbulent fluid., *Journal of Fluid Mechanics*, *370*, 29–52. 6, 12, 26, 27, 56, 83

Jenkins, J. T. (2006), Dense shearing flows of inelastic disks, *Physics of Fluids*, *18*(10). 8

Jenkins, J. T. (2007), Dense inclined flows of inelastic spheres, *Granular Matter*, *10*(1), 47–52. 8

Jenkins, J. T., and D. Berzi (2010), Dense inclined flows of inelastic spheres: tests of an extension of kinetic theory, *Granular Matter*, *12*(2), 151–158. 8, 84, 94

Jha, S. K., and F. A. Bombardelli (2010), Toward two-phase flow modeling of nondilute sediment transport in open channels, *Journal of Geophysical Research: Earth Surface*, *115*(F3), f03015. 4

Ji, C., A. Munjiza, E. Avital, J. Ma, and J. J. R. Williams (2013), Direct numerical simulation of sediment entrainment in turbulent channel flow, *Physics of Fluids*, *25*(5), 056601. 4, 5, 26, 104

Ji, C., A. Munjiza, E. Avital, D. Xu, and J. Williams (2014), Saltation of particles in turbulent channel flow, *Phys. Rev. E*, *89*, 052,202. 5

Jiang, Z., and P. K. Haff (1993), Multiparticle simulation methods applied to the micromechanics of bed load transport, *Water Resources Research*, *29*(2), 399–412. 6

Jones, J. E. (1924), On the determination of molecular fields. ii. from the equation of state of a gas, *Proceedings of the Royal Society of London A: Mathematical, Physical and Engineering Sciences*, *106*(738), 463–477. 15

Jop, P. (2015), Rheological properties of dense granular flows, *Comptes rendus physique*, *16*(1), 62–72. 8, 9, 10, 90

Jop, P., F. Y., and O. Pouliquen (2005), Crucial role of sidewalls in granular surface flows: consequences for the rheology, *Journal of Fluid Mechanics*, *541*, 167–192. 9

Jop, P., Y. Forterre, and O. Pouliquen (2006), A constitutive law for dense granular flows, *Nature*, *441*(7094), 727–730. xiv, 9, 10, 90, 91, 92

Kamrin, K., and G. Koval (2012), Nonlocal constitutive relation for steady granular flow, *Phys. Rev. Lett.*, *108*, 178,301. 10, 89, 103

Kidanemariam, A. G., and M. Uhlmann (2014), Interface-resolved direct numerical simulation of the erosion of a sediment bed sheared by laminar channel flow, *International Journal of Multiphase Flow*, *67*(0), 174 – 188. 5

Kidanemariam, A. G., C. Chan-Braun, T. Doychev, and M. Uhlmann (2013), Direct numerical simulation of horizontal open channel flow with finite-size, heavy particles at low solid volume fraction, *New Journal of Physics*, *15*(2), 025,031. 5

Komatsu, T. S., S. Inagaki, N. Nakagawa, and S. Nasuno (2001), Creep motion in a granular pile exhibiting steady surface flow, *Phys. Rev. Lett.*, *86*, 1757–1760. 57, 89

Lacaze, L., and R. R. Kerswell (2009), Axisymmetric granular collapse: A transient 3d flow test of viscoplasticity, *Phys. Rev. Lett.*, *102*, 108,305. 10

Lajeunesse, E., L. Malverti, and F. Charru (2010), Bed load transport in turbulent flow at the grain scale: Experiments and modeling, *Journal of Geophysical Research: Earth Surface*, *115*(F4), F4. 40

Lamb, M. P., W. E. Dietrich, and J. G. Venditti (2008), Is the critical shields stress for incipient sediment motion dependent on channel-bed slope?, *Journal of Geophysical Research: Earth Surface*, *113*(F2), f02008. 3, 75

Larcher, M., L. Fraccarollo, A. Armanini, and H. Capart (2007), Set of measurement data from flume experiments on steady uniform debris flows, *Journal of Hydraulic Research*, *45*, 59–71. 13

Li, L., and M. Sawamoto (1995), Multi-phase model on sediment transport in sheet-flow regime under oscillatory flow, *Coastal engineering Japan*, *38*, 157–178. 23

Lois, G., A. Lemaître, and J. M. Carlson (2006), Emergence of multi-contact interactions in contact dynamics simulations of granular shear flows, *Europhys. Lett.*, *76*(2), 318–324. 92

Love, A. E. H. (1927), *A Treatise on the Mathematical Theory of Elasticity*, 4th ed., Cambridge University Press. 78

Lun, C. K. K., S. B. Savage, D. J. Jeffrey, and N. Chepurniy (1984), Kinetic theories for granular flow: inelastic particles in couette flow and slightly inelastic particles in a general flowfield, *Journal of Fluid Mechanics*, *140*, 223–256. xiv, 13, 84, 93

Maurin, R. (2012), Using a dem approach for experimental inter-granular force assessment, Master's thesis, ENS Lyon. 15

Maurin, R., J. Chauchat, B. Chareyre, and P. Frey (2015), A minimal coupled fluid-discrete element model for bedload transport, *Physics of Fluids*, *27*(11), 113302, doi:http://dx.doi.org/10.1063/1.4935703. 13

Maxey, M. R., and J. J. Riley (1983), Equation of motion for a small rigid sphere in a nonuniform flow, *Physics of Fluids (1958-1988)*, *26*(4), 883–889. 5, 25

Meyer-Peter, E., and R. Müller (1948), Formulas for bed-load transport, in *Proc. 2nd Meeting*, pp. 39–64, IAHR. ix, xi, 2, 3, 53, 54

Midi, G. (2004), On dense granular flows, *The European Physical Journal E*, *14*(4), 341–365. 8, 57

Morchid-Alaoui, L. (2015), Size-segregation in bedload transport, a numerical approach, Master's thesis, ENSE3, INP Grenoble. 105, 107

Moreau, J. (1983), Liasons unilatérales sans frottement et chocs inélastiques, *Comptes rendus de l'Académie des Sciences*, *296*, 1473–1476. 15

Mouilleron, H., F. Charru, and O. Eiff (2009), Inside the moving layer of a sheared granular bed, *Journal of Fluid Mechanics*, *628*, 229–239. 12, 31

Muir Wood, D. (1990), *Soil behaviour and critical state soil mechanics*, Cambridge University Press. 10

Nezu, I. (1977), Turbulent structure in open-channel flows, Ph.D. thesis, Kyoto University. 27

Nezu, I., and H. Nakagawa (1993), *Turbulence in Open Channel Flows*, IAHR Monographs. 27

Ni, W.-J., and H. Capart (2015), Cross-sectional imaging of refractive-index-matched liquid-granular flows, *Experiments in Fluids*, *56*(8), 163. 32

Niño, Y., and M. García (1998), Using lagrangian particle saltation observations for bedload sediment transport modelling, *Hydrological Processes*, *12*(8), 1197–1218. 26

Ouriemi, M., P. Aussillous, M. Medale, Y. Peysson, and E. Guazzelli (2007), Determination of the critical shields number for particle erosion in laminar flow, *Physics of Fluids*, *19*(6), 061706. 55

Ouriemi, M., P. Aussillous, and E. Guazzelli (2009), Sediment dynamics. part 1. bed-load transport by laminar shearing flows, *Journal of Fluid Mechanics*, *636*, 295–319. 12, 90

Papanicolaou, A., P. Diplas, N. Evaggelopoulos, and S. Fotopoulos (2002), Stochastic incipient motion criterion for spheres under various bed packing conditions, *Journal of Hydraulic Engineering*, *128*(4), 369–380. 55

Penn, A. (2014), Personal communication. 32

Prandtl, L. (1926), Bericht über neuere Turbulenzforschung, *Hydraulische Probleme. Vorträge Hydrauliktagung Göttingen*, *5*, 1–13. 23

Radjai, F., and F. Dubois (Eds.) (2011), *Discrete-element modeling of granular materials*, ISTE, Wiley. 15, 16

Recking, A. (2009), Theoretical development on the effects of changing flow hydraulics on incipient bed load motion, *Water Resources Research*, *45*(4), w04401. 3, 75

Recking, A. (2010), A comparison between flume and field bed load transport data and consequences for surface-based bed load transport prediction, *Water Resources Research*, *46*(3), W03,518. ix, 3

Recking, A., A. Frey, P.and Paquier, P. Belleudy, and J. Champagne (2008), Feedback between bed load transport and flow resistance in gravel and cobble bed rivers, *Water Resources Research*, *44(5)*(W05412). 3

Recking, A., D. Richard, and D. G. (Eds.) (2013), *Torrents et rivières de montagne, dynamique et aménagement*, Quae. ix, 3

Revil-Baudard, T., and J. Chauchat (2013), A two-phase model for sheet flow regime based on dense granular flow rheology, *Journal of Geophysical Research: Oceans*, *118*(2), 619–634. xv, 4, 5, 6, 12, 19, 20, 23, 26, 35, 57, 67, 70, 82, 92, 104, 105

Revil-Baudard, T., J. Chauchat, D. Hurther, and P.-A. Barraud (2015), Investigation of sheet-flow processes based on novel acoustic high-resolution velocity and concentration measurements, *Journal of Fluid Mechanics*, *767*, 1–30. 12, 57, 104

Richard, P., A. Valance, J.-F. Métayer, P. Sanchez, J. Crassous, M. Louge, and R. Delannay (2008), Rheology of confined granular flows: Scale invariance, glass transition, and friction weakening, *Phys. Rev. Lett.*, *101*, 248,002. 57, 89, 90

Richardson, J. F., and W. N. Zaki (1954), Sedimentation and fluidization: Part i, *Trans. Instn. Chem. Engrs*, *32*. 25, 26, 44

Richefeu, V., G. Mollon, D. Daudon, and P. Villard (2012), Dissipative contacts and realistic block shapes for modeling rock avalanches, *Engineering Geology*, *149-150*, 78–92. 16

Rickenmann, D. (1991), Hyperconcentrated flow and sediment transport at steep slopes, *Journal of Hydraulic Engineering*, *117*(11), 1419–1439. 3

Rickenmann, D. (2012), *Alluvial Steep Channels: Flow Resistance, Bedload Transport Prediction, and Transition to Debris Flows*, chap. 28, pp. 386–397, John Wiley & Sons, Ltd. 3, 75

Ripert, E. (2011), Le charriage des sédiments en montagne: Un défi scientifique pour une meilleure gestion du risque torrentiel, Master's thesis, Université Paul Valéry Montpellier 3. 107

Rognon, P., J.-N. Roux, M. Naaïm, and F. Chevoir (2007), Dense flows of bidisperse assemblies of disks down an inclined plane, *Physics of Fluids*, *19*(5), 058101. 16, 17

Roux, J.-N., and G. Combe (2002), Quasistatic rheology and the origins of strain, *Comptes Rendus Physique*, *3*(2), 131 – 140. 18, 35

Savage, S. B., and M. Sayed (1984), Stresses developed by dry cohesionless granular materials sheared in an annular shear cell, *Journal of Fluid Mechanics*, *142*, 391–430. 9

Schiller, L., and A. Naumann (1933), Über die Grundlegenden Berechungen bei der Schwerkraftaufbereitung, *Ver. Deut. Ing.*, *77*. 5, 25

Schmeeckle, M. W. (2014), Numerical simulation of turbulence and sediment transport of medium sand, *Journal of Geophysical Research: Earth Surface*, *119*(6), 1240–1262. 5

Schmeeckle, M. W., J. M. Nelson, and R. L. Shreve (2007), Forces on stationary particles in near-bed turbulent flows, *Journal of Geophysical Research: Earth Surface*, *112*(F2), F02,003. 25, 26, 104

Schwager, T., and T. Pöschel (2007), Coefficient of restitution and linear spring-dashpot model revisited, *Granular Matter*, *9*, 465–469. 18

Shields, A. (1936), Anwendung der Aehnlichkeitsmechanik und der Turbulenzforschung auf die Geschiebebewegung, Doktor-Ingenieurs dissertation, Technischen Hochschule, Berlin. 1

Silbert, L. E., D. Ertaş, G. S. Grest, T. C. Halsey, D. Levine, and S. J. Plimpton (2001), Granular flow down an inclined plane: Bagnold scaling and rheology, *Phys. Rev. E*, *64*, 051,302. 36

Simeonov, J., and J. Calantoni (2012), Modeling mechanical contact and lubrication in direct numerical simulations of colliding particles, *International Journal of Multiphase Flow*, *46*(0), 38 – 53. 5

Sumer, B. M., A. Kozakiewicz, J. Fredsø e, and R. Deigaard (1996), Velocity and concentration profiles in sheet-flow layer of movable bed, *Journal of Hydraulic Engineering*, *122*(10), 549–558. 12, 61

Taberlet, N., P. Richard, A. Valance, W. Losert, J. M. Pasini, J. T. Jenkins, and R. Delannay (2003), Superstable granular heap in a thin channel, *Phys. Rev. Lett.*, *91*, 264,301. 91

Takahashi, T. (1978), Mechanical characteristics of debris flow, *Journal of the Hydraulics Division*, *104*(8), 1153–1169. 70

Takahashi, T. (2007), *Debris Flow: Mechanics, Prediction and Countermeasures*, Balkema-proceedings and monographs in engineering, water and earth sciences, Taylor & Francis. 70

Thornton, A., T. Weinhart, S. Luding, and O. Bokhove (2012), Modeling of particle size segregation: calibration using the discrete particle method, *International Journal of Modern Physics C*, *23*(08), 1240,014. 17

Tripathi, A., and D. V. Khakhar (2011), Rheology of binary granular mixtures in the dense flow regime, *Physics of Fluids*, *23*(11), 113302. 16, 107

Trulsson, M., B. Andreotti, and P. Claudin (2012), Transition from the viscous to inertial regime in dense suspensions, *Phys. Rev. Lett.*, *109*, 118,305. 12

Van der Vaart, K., P. Gajjar, G. Epely-Chauvin, N. Andreini, J. M. N. T. Gray, and C. Ancey (2015), Underlying asymmetry within particle size segregation, *Phys. Rev. Lett.*, *114*, 238,001. 105

Venditti, J. G., W. E. Dietrich, P. A. Nelson, M. A. Wydzga, J. Fadde, and L. Sklar (2010), Mobilization of coarse surface layers in gravel-bedded rivers by finer gravel bed load, *Water Resources Research*, *46*(7), w07506. 105

Vowinckel, B., T. Kempe, and J. Fröhlich (2014), Fluid-particle interaction in turbulent open channel flow with fully-resolved mobile beds, *Advances in Water Resources*, *72*(0), 32 – 44. 5

Šmilauer, V., and B. Chareyre (2010), *Šmilauer and B. Chareyre, "Yade Dem Formulation", in Yade Documentation (V. Šmilauer, ed.), The Yade Project, 1st ed., 2010. http://yade-dem.org/doc/formulation.html*. 16

Šmilauer, V., E. Catalano, B. Chareyre, S. Dorofeenko, J. Duriez, A. Gladky, J. Kozicki, C. . Modenese, L. Scholtès, L. Sibille, J. Stránský, and K. Thoeni (2010),

Yade Documentation (V. Šmilauer, ed.), The Yade Project, 1st ed., http://yade-dem.org/doc/. 18

Wachs, A. (2011), Peligriff, a parallel dem-dlm/fd direct numerical simulation tool for 3d particulate flows, *Journal of Engineering Mathematics*, *71*(1), 131–155. 4, 5, 16, 17

Weinhart, T., R. Hartkamp, A. Thornton, and S. Luding (2013), Coarse-grained local and objective continuum description of three-dimensional granular flows down an inclined surface, *Physics of Fluids*, *25*(7), 070605. 79

Wiberg, P. L., and J. D. Smith (1985), A theoretical model for saltating grains in water, *Journal of Geophysical Research: Oceans*, *90*(C4), 7341–7354. 26

Wilson, K. (1987), Analysis of bed-load motion at high shear stress, *Journal of Hydraulic Engineering*, *113*(1), 97–103. xi, 3, 54, 82

Wilson, K. C. (1966), Bed-load transport at high shear stress, in *A.S.C.E*, vol. HY6, edited by ASCE. xi, 53, 54

Wong, M., and G. Parker (2006), Reanalysis and correction of bed-load relation of Meyer-Peter and Müller using their own database, *Journal of Hydraulic Engineering*, *132*(11), 1159–1168. 3

Yalin, M. S. (1977), *Mechanics of sediment transport*, 2nd edition ed., Pergamon Press, Ontario. xi, 54

Yeganeh, A., H. Gotoh, and T. Sakai (2000), Applicability of euler-lagrange coupling multiphase-flow model to bed-load transport under high bottom shear, *Journal of Hydraulic Research*, *38*(5), 389–398. 6

Yeganeh-Bakhtiary, A., B. Shabani, H. Gotoh, and S. S. Wang (2009), A three-dimensional distinct element model for bed-load transport, *Journal of Hydraulic Research*, *47*(2), 203–212. 17

Yohannes, B., and K. M. Hill (2010), Rheology of dense granular mixtures: Particle-size distributions, boundary conditions, and collisional time scales, *Phys. Rev. E*, *82*, 061,301. 107

Zannetti, P. (1986), Monte-carlo simulation of auto- and cross-correlated turbulent velocity fluctuations (mc-lagpar {II} model), *Environmental Software*, *1*(1), 26 – 30. 27

Zhu, H., Z. Zhou, R. Yang, and A. Yu (2007), Discrete particle simulation of particulate systems: Theoretical developments, *Chemical Engineering Science*, *62*(13), 3378 – 3396. 5

Zhu, H., Z. Zhou, R. Yang, and A. Yu (2008), Discrete particle simulation of particulate systems: A review of major applications and findings, *Chemical Engineering Science*, *63*(23), 5728 – 5770. 5

Abstract: A numerical study of turbulent bedload transport is presented, focusing on the granular phase behavior. A minimal coupled numerical model is proposed, associating a three-dimensional discrete element method with a one-dimensional volume-averaged fluid momentum balance. The model is compared with classical experimental results of dimensionless sediment transport rate as a function of the Shields number. The comparison is extended to granular depth profiles of existing quasi-2D bedload transport experiments. The validated model is further used to analyze the granular depth structure in bedload transport. Varying the channel inclination angle and the specific density, it is shown that the classical Shields number and dimensionless sediment transport rate formulations do not take appropriately into account the effects of these two parameters. Analyzing the solid depth profiles and the continuous two-phase flow equations, a rescaling of the Shields number is proposed and is shown to make all the data collapse onto a master curve. In addition, the bedload transport granular rheology is characterized by computing locally the stress tensor as a function of the depth, for a serie of simulations varying of Shields number, particle diameter and specific density. The obtained results are analyzed in the framework of the $\mu(I)$ rheology and show a collapse of the data up to unexpectedly high inertial numbers. These results show the relevancy in modelling the granular phase behavior using the $\mu(I)$ framework, and also challenge the existing granular rheologies.

Keywords: Sediment transport, bedload, granular media, Discrete Element Method, two-phase flow, fluid-grain coupling, granular depth structure, granular rheology

Résumé : Le manuscrit présente une étude numérique du transport solide par charriage d'un point de vue granulaire. Un modèle numérique minimal couplé est développé, associant une modélisation par éléments discrets tri-dimensionnelle à une résolution fluide unidirectionnelle moyennée en volume. Le modèle est comparé aux résultats experimentaux classiques, en terme de débit solide adimensionné en fonction du nombre de Shields. La comparaison est étendue à des résultats expérimentaux existants, de profils moyens granulaires verticaux dans une configuration quasi-bidimensionnelle. Le modèle validé est ensuite utilisé pour analyser la structure granulaire verticale en transport par charriage. En étudiant l'effet de la pente et de la densité spécifique, il est montré que les formulations classiques du nombre de Shields et du débit solide adimensionné ne prennent pas en compte de manière appropriée les effets de ces deux paramètres. À partir d'une analyse des équations continues moyennées diphasiques, une modification du nombre de Shields est proposée et apparaît réunir les données sur une courbe maîtresse en considérant le débit solide adimensionné en fonction du nombre de Shields modifié. Dans un deuxième temps, la rhéologie de la phase granulaire en transport par charriage est caractérisée en évaluant localement le tenseur des contraintes particulaires en fonction de la profondeur, dans une série de simulations avec variation du nombre de Shields, du diamètre des grains et de la densité spécifique. Les résultats obtenus sont analysés dans le cadre de la rhéologie $\mu(I)$, et montrent un alignement des données jusqu'à des nombres inertiels inhabituellement élevés. Ces résultats suggèrent la possibilité de décrire la rhéologie granulaire du transport par charriage dans le formalisme $\mu(I)$, et représentent également un défi pour les théories granulaires existantes.

Mot clés : Transport de sédiments, charriage, milieux granulaires, méthode par éléments discrets, écoulement diphasique, couplage fluide-grain, structure granulaire verticale, rhéologie granulaire